AN ABSTRACT OF THE THESIS OF

Ashley Nicholle Shultz for the degree of Doctor of Philosophy in Physics presented on April 26, 1996. Title: Creation of Defects and Interactions between Defects and Small Molecules on TiO_2(110) Surfaces: Comparative SHG and XPS Studies

Abstract approved: Redacted for Privacy

William M. Hetherington III

Rutile TiO_2 surfaces, which have broad applications in photocatalysis, have been extensively studied for over two decades. Despite this research effort, large gaps exist in the basic understanding of surface structure, methods by which surface defects can be created, and interactions between small molecules and these surfaces. In this thesis, Second Harmonic Generation (SHG) is used to probe the structure of TiO_2(110) surfaces. These experiments show that above band-gap UV photons create oxygen-vacancy defects on single-crystal surfaces, a process previously considered unlikely. This defect-creation saturates after only 360 J/cm^2 total UV fluence. Further understanding of UV defect creation is gained through parallel X-ray Photoelectron Spectroscopy (XPS) experiments. Some Ultraviolet Photoelectron Spectroscopy (UPS) studies are also presented here, but this technique is rapidly abandoned due to difficulties in interpreting the UPS spectra without ambiguity. These studies rule out contaminant-driven interactions and allow quantification of the defects produced by UV illumination. The number of defects produced by UV at saturation is consistent with oxygen vacancies at 1/6 of the total oxygen sites present on the surface.

In addition, both SHG and XPS are used to examine interactions between these defects and small molecules (interactions between defects and O_2, H_2O, HCOOH, and N_2O are presented here). The results of these experiments are then compared to previous studies present in the literature on other molecules. In compiling experiments done with many different molecules, it becomes clear that the observed defect-molecule interactions correlate

with the electron affinity of the molecule used. If the molecule has an electron affinity it will interact with surface defects, resulting in removal of the defect signature. It is unclear however, that removal of the defect signature in this way necessarily implies that the surface has been physically healed to become stoichiometric. XPS indicates that this is the case, but detailed study of the SHG experiments suggests that it is possible that healing may sometimes occur through the formation of Ti^{4+}:X^{-} complexes from a Ti^{3+} defect and an electronegative molecule X. Indeed it appears that Ti^{4+}:O_2^{-} complexes are present on all $TiO_2(110)$ surfaces.

Creation of Defects and Interactions between Defects and Small Molecules on $TiO_2(110)$ Surfaces: Comparative SHG and XPS Studies

by

Ashley Nicholle Shultz

A THESIS

submitted to

Oregon State University

in partial fulfillment of
the requirements for the
degree of

Doctor of Philosophy

Presented April 26, 1996
Commencement June 1996

Doctor of Philosophy thesis of Ashley Nicholle Shultz presented on April 26, 1996

APPROVED:

Redacted for Privacy

Major Professor, representing Physics

Redacted for Privacy

Chair of Department of Physics

Redacted for Privacy

Dean of Graduate School

I understand that my thesis will become part of the permanent collection of Oregon State University libraries. My signature below authorizes release of my thesis to any reader upon request.

Redacted for Privacy

Ashley Nicholle Shultz, Author

ACKNOWLEDGMENTS

I am sincerely grateful to my advisor, Bill Hetherington, for his guidance and support over the last five years. His knowledge of the field is immense, providing much needed perspective on the experiments presented here. I am deeply indebted to Winyann Jang and Chang-Yuan Ju, who came before me, for developing the LASER and vacuum systems used in SHG experiments. My work was made much easier through the inheritance of their functioning experimental system. I also wish to thank Robin Zagone and Bradley Matson for their friendship and counsel these past years. Many thanks to Don Baer and Li-Qiong Wang for their patience, expertise and the use of their surface science systems at Pacific Northwest laboratory. XPS experiments done there added much needed confirmation of SHG results, and opened up many more avenues of future research. I look forward to fruitful collaboration in the coming years. I also extend thanks to Mark Engelhard, who spent many hours working hard to ensure that my experiments at PNL ran smoothly. Thanks also to my family, to Wes Colgan III, and to Teresa Lebel for providing the personal support network necessary to make this thesis happen.

TABLE OF CONTENTS

TABLE OF CONTENTS: (Continued)

TABLE OF CONTENTS: (Continued)

LIST OF FIGURES

LIST OF FIGURES: (Continued)

LIST OF FIGURES: (Continued)

LIST OF TABLES

DEDICATION

For Pamela K. Barclay and Florence B. (Sandi) Ashton. I stand on your shoulders.

CREATION OF DEFECTS AND INTERACTIONS BETWEEN DEFECTS AND SMALL MOLECULES ON TiO_2(110) SURFACES: COMPARATIVE SHG AND XPS STUDIES

CHAPTER 1
INTRODUCTION

This thesis arises out of studies of rutile TiO_2 surfaces that were done with two major goals in mind. The first is based on the realization that a fundamental understanding of TiO_2 surfaces remains elusive, despite two decades of extensive research on this material. Thus one focus of this thesis is to re-evaluate our understanding of these surfaces based on a complete study of the literature. Doing this points to obvious gaps in our understanding of very simple processes that occur on these surfaces. In particular, the response of TiO_2 surfaces to ultraviolet light has not been adequately explored, and only cursory studies of interactions between these surfaces and small molecules have been attempted. Filling in this gap motivates much of the research here. The second goal of this research is to further develop second harmonic generation (SHG) as a technique for studying surfaces of centrosymmetric materials. SHG has shown promise in recent years as a probe that will form a bridge between real-world environments such as air or solution and surface science studies necessarily done in high vacuum environments. In addition, evidence presented in this thesis suggests that SHG can provide information about physical surface structure that can not be observed using conventional surface science techniques. This chapter further explores these motivations and presents an overview of the discussion to come.

Titanium dioxide (TiO_2) has been so heavily studied over the last two decades that many believe it to be well-understood. TiO_2 is of interest to scientists because of its broad applications in many fields. It is a ubiquitous material, as a primary component of many soils and the main ingredient in white paint. In addition TiO_2 has a high damage threshold, making it desirable as an optical coating. TiO_2 surfaces are extremely corrosion-resistant as well, adding to their utility. But the main reason for their popularity is their tremendous photocatalytic activity, which has led to diverse applications in environmental science and other fields. Early in the study of TiO_2 it was observed that water appears to

catalytically decompose on TiO_2 in the presence of UV light with energy above the bulk band-gap of TiO_2 [1]. This generated such enthusiasm that research efforts were quickly directed toward exploring this and more complex photochemical processes. It was hoped that these processes would provide a method for efficient generation of power using solar energy, so this rush to explore TiO_2 photoelectrolysis is certainly understandable. This research led to the additional discovery that some complex organic molecules interact with TiO_2 surfaces in the presence of UV. Most of these molecules decompose, providing an avenue for degradation of some organic environmental toxins. But some molecules use the surface as an intermediary to react with each other, such that synthesis of more complex organic molecules is also possible. The tendency in such research is to characterize the reaction between each individual molecule and a TiO_2 surface in the presence of UV. But little emphasis is placed on understanding the overall mechanisms that drive these reactions so that a predictive scheme for all molecules can be developed.

Since most research on TiO_2 has focused on complicated photocatalytic processes, simple studies of these surfaces have often been neglected. An unfortunate side-effect of this is a general impression that the structure and simple behavior of TiO_2 surfaces is well understood. This misconception arises from early studies that are considered definitive, despite being based on somewhat arbitrary interpretations of emerging techniques. As the techniques available to surface scientists have been refined over the years, evidence that contradicted these early definitive experiments began to surface. Chapter 2 discusses in detail past research on TiO_2, exposes the gaps in our understanding of TiO_2 surfaces, and demonstrates the need for more study.

Conventional surface science techniques are limited to high and ultra-high vacuum environments because they rely on the detection of particles that are either ejected or scattered from a surface. Examples of techniques of this type include x-ray photoelectron spectroscopy (XPS), ultraviolet photoelectron spectroscopy (UPS), Auger electron spectroscopy (AES), electron energy-loss spectroscopy (EELS), and low-energy electron diffraction (LEED). All of these probes detect electrons ejected or scattered from the surface. Information about surface structure (electronic or physical) and stoichiometry is then determined by examining either the spatial and/or energy distributions of these electrons. Clearly this

distribution will be altered if the ejected electrons encounter and collide with ambient gas molecules between the surface and the electron detection system. The mean free path of these electrons is such that these techniques can not be used for ambient pressures above $1x10^{-4}$ Torr, and are best used at considerably lower pressures. Unfortunately, very few "real world" applications exist for these surfaces in UHV. In realistic environments, such as atmospheric pressure and solution, collisions with gas molecules are unavoidable, making conventional surface science techniques unusable. It is traditional in such cases to do *ex situ* studies, where interactions under unfavorable conditions are examined by looking at the surface in high-vacuum "before" and "after" the interaction has occurred. But it is desirable to develop surface science techniques that can probe surfaces *in situ* so that realistic environments and interactions can be studied. The ideal technique would provide surface information in all pressure ranges, and even in hostile environments.

Second harmonic generation has shown great promise as a tool to probe surfaces under conditions when conventional surface science techniques fail. SHG is a second-order nonlinear process in which two photons with the same frequency from an incident field are annihilated while a third photon with twice this frequency is simultaneously created. This process is coherent, such that the second harmonic photon propagates along the same direction as the incident photons. The SHG response of a material is governed by a second-order nonlinear electric susceptibility tensor that reflects the physical characteristics of the material. For nonlinear crystals where this susceptibility is large, substantial intensity at the second harmonic can be generated. Such crystals are extensively used to double the frequency of laser sources, extending the available spectrum of coherent, intense, laser light. Under the electric-dipole approximation, SHG is forbidden in materials that have inversion symmetry. This is because symmetry arguments dictate that the second-order susceptibility tensor of centrosymmetric materials vanish. But at a surface, or at any interface between centrosymmetric media, inversion symmetry is necessarily broken along the surface normal. Second harmonic generation is therefore always allowed in the surface or interface region, and can be used as a probe of the structure of such a region. Since it is an optical technique, study of surfaces in a wide variety of environments is possible, as long as the environment does not absorb either the fundamental or the harmonic light.

SHG is sensitive both to the symmetry of a material and to its electronic structure through resonances. Most other surface science techniques can probe only one of these aspects of surface structure. XPS and UPS, for example, are sensitive only to the core and valence electronic structures respectively, while LEED only probes the symmetry of a surface. This additional sensitivity of SHG can often make changes in harmonic signal difficult to interpret, but compensates for this by providing information unavailable by other means. Chapter 3 discusses the history and utility of SHG as a surface-specific probe, and develops a phenomenological treatment of surface SHG in a reflection-based geometry. XPS and UPS, the other surface science techniques used in the research presented here, are also developed in this chapter. For the SHG discussion, emphasis is placed on the theory behind the technique. For XPS and UPS, the more established surface probes, the emphasis is shifted to interpretation of spectra.

That SHG is sensitive to both physical and electronic surface structure leads to another facet of the motivation for this research. As previously mentioned, most scientists believe that simple structure and interactions on TiO_2 surfaces are well understood based on early experiments that are considered definitive. Other early studies contributed to this impression in another way. Namely, the first studies were carried out on powdered samples which have complex topography. Molecular adsorption was seen on such surfaces for many different molecules, and in most cases this adsorption was thought to occur at defects or steps on the surface. Electron spin resonance (ESR) experiments, for example, suggested that charged molecular oxygen would bind to defect sites, and was the major adsorbed species. These oxygen molecules easily desorbed when exposed to photons with energy above the band-gap. But technology developed in the following years that allowed growth single-crystal samples for study. Surfaces of these samples were prepared by cutting along the desired axis, ion-sputtering to remove any contamination, and annealing to high temperature in low partial pressures of O_2. The result was a single-crystal surface that appeared "defect-free" using techniques sensitive to electronic defects. No adsorption of molecular oxygen was expected on these surfaces. ESR experiments to check this expectation were not done because it was considered unlikely that this technique would be sensitive enough to detect small amounts of adsorbed O_2. It was thought instead that any

oxygen vacancy defects created on such a surface would be healed by O_2 exposure through dissociation such that only atomic oxygen ions would be present. In general, it was assumed that any defect-related adsorption seen on the powder samples would be absent from the single-crystal surfaces. Until recently, this assumption was not challenged. This was largely because the techniques used to determine whether defects were present are sensitive only to the electronic structure of the surface. Here a defect "signature" appears in the spectra for the technique when uncoordinated titanium atoms (oxygen vacancies) are present. A stoichiometric surface is characterized by fully-coordinated Ti^{4+} ions, while a surface with oxygen vacancies will have Ti^{3+} defects. These defects appear as a shoulder on the Ti-2p peaks in XPS spectra, and as a small Ti-3d defect state in the gap in UPS spectra. In the case of adsorbed molecular oxygen, a charge transfer could take place between a Ti^{3+} defect and O_2 to form a Ti^{4+}:O_2^- complex. If this occurs, the titanium atom in the complex is fully coordinated. This site would then appear electronically (using XPS and UPS) to be "healed" when a species other than the oxygen ion necessary to produce physical healing is present. But this possibility was not seriously entertained until recent observation in this group that above band-gap UV light appeared to induce defects even on "defect-free" single-crystal surfaces. This observation, which is confirmed and further developed in this thesis, led to the conclusion that either Ti^{4+}:O_2^- complexes exist even on "defect-free" surfaces or some mechanism exists by which photons that are barely above the band gap can remove surface lattice oxygen atoms. The latter was thought unlikely by energetics arguments, while the former implies that lack of an electronic defect signature for a surface is not conclusive proof of a physically perfect structure. The possible existence of physical defects that are not detectable using conventional surface science techniques is a recurring theme in this thesis.

Chapter 4 describes the techniques and apparatus used for the SHG, XPS, and UPS experiments presented here. For SHG, the Nd:YAG laser system is discussed in detail, with sections describing Q-switching and mode-locking to produce high peak-power pulses. A section on frequency-doubling in nonlinear crystals is also included since this process is used to produce both the 532 nm beam used for SHG and the 266 nm beam used for UV exposure on surfaces. The UHV system and gas introduction lines are also discussed.

Sample preparation techniques are presented as well. Experiments using XPS and UPS were done in a different UHV chamber from the SHG experiments, and a separate section describing experimental details of this system is included in Chapter 4. Despite the necessity of doing experiments in different UHV chambers, experimental conditions were kept as uniform as possible. Any necessary differences in experimental technique are outlined in these section. Since XPS and UPS are limited to UHV, *ex situ* studies of molecule-surface interactions were necessary in most cases. SHG, not limited to UHV, allowed for *in situ* studies and experiments at high gas pressures.

Chapter 5 presents the results of SHG, XPS, and UPS studies done on $TiO_2(110)$ surfaces. Discussion begins with previous results on $TiO_2(001)$ surface in which UV defect creation and O_2 high-pressure adsorption were first observed. These experiments are then repeated on $TiO_2(110)$ surfaces, with similar results. Then XPS experiments that confirm the observation of UV defect creation are presented. The number of defects created is quantified by comparison to studies of systematic surface damage done using a low-energy electron beam. UPS is also explored as a technique for studying and quantifying surface defects and interactions. Then interactions between Ti^{3+} surface defects and several small molecules are characterized. Here the behaviors of H_2O and HCOOH are explored, and the results are added to a growing list of molecules for which defect-molecule interactions have been studied. A trend in the behavior of these molecules is then noted, and tested as a predictive scheme for interactions between defects and N_2O. Finally, identical SHG and XPS experiments are done to explore N_2O-defect interactions. This shows that SHG can observe changes and differences in surface structure that XPS and UPS can not detect. In Chapter 6, this research is summarized and its implications are explored.

The work presented here is in various stages of publication. SHG and XPS observations of UV-creation and O_2-healing of defects are found in a published article [2], as are XPS studies of interactions between defects and H_2O [3]. A paper describing reactions between HCOOH and defects has been submitted to *Surface Science*, as has a letter summarizing N_2O results. A comprehensive paper describing defect interactions with a number of molecules has been accepted by the *Journal of Vacuum Science and Technology* and is in press.

CHAPTER 2
PROPERTIES OF RUTILE TiO_2

2.1 Motivation

In 1972, Fujishima and Honda [1] first observed the photocatalytic decomposition of water on TiO_2 electrodes. This discovery suggested that TiO_2 could be used for solar photoelectrochemical generation and storage of energy [4, 5, 6, 7]. Since then much research has focused on developing a better understanding of TiO_2 surfaces, with the ultimate aim of enhancing their water-splitting photocatalytic efficiency. As this research progressed, it was also demonstrated that photocatalysis on TiO_2 surfaces could also be used to decompose other molecules. In particular, TiO_2-based photocatalysis is now commonly used to destroy unwanted complex organic molecules that contaminate air and wastewater [8, 9]. "Mainstream" applications for catalyzed decomposition of organics by TiO_2 have also emerged. For example, TiO_2 coatings are now deposited on surfaces for use in kitchens, bathrooms, and even fishtanks to prevent the growth of organic substances such as fungi (mold or mildew) and algae [10]. TiO_2 also forms when Ti metal is exposed to most oxidizing environments. The resulting oxide layer is highly stable, protecting the substrate metal from cracking and pitting in a wide variety of environments. The corrosion-resistance of this oxide is responsible for the extensive use of Ti metal in biological devices such as pacemakers and hip-replacement implants. Crystals of TiO_2 also have very high optical damage thresholds, making them useful as coatings for optics. In addition, TiO_2 is used commonly as the primary ingredient (pigment) in white paint. These broad applications of TiO_2 as a material provide the impetus for the research in this thesis.

Central to most of the above uses for TiO_2 surfaces are interactions between these surfaces and molecules in the surrounding environment. A full understanding of these interactions is certainly warranted so that positive interactions can be optimized, negative interactions can be suppressed, and new applications can be developed. Since many of these interactions seem to involve photocatalysis, it is important to understand the effects of light absorbed in the near-surface region both with and without the presence of adsorbates. It may seem that such basic understanding of the nature of surfaces, especially a surface

that has been as heavily studied as TiO_2, would have already been achieved. Surprisingly enough, the primary observations presented here are novel. This is largely because most probes of photocatalytic behavior on these surfaces focus on the initial and final state of the reaction molecules, with little attention paid to changes that may occur in the structure of the catalyst surface. Using probes such as SHG and XPS that are strictly sensitive to the electronic and/or physical structure of the surface helps to round out the understanding of these processes. An ideal study would combine these surface specific probes with the techniques that monitor the behavior of the reaction molecules.

2.2 The Structure and Properties of Bulk Rutile TiO_2

Titanium Dioxide is a transition metal oxide that can crystallize in one of three forms (brookite, anatase, and rutile). Anatase and rutile are the most easily formed of the crystalline structures, and are used for most photocatalytic work. Both anatase and rutile are composed of chains of TiO_6 octahedra. Each Ti atom in an octahedron is in a 4+ valence state, and is surrounded by six O^{2-} ions. The difference between the two structures lies in the amount of distortion of each of these octahedra and the assembly pattern of the chains. Figure 2.1 shows the unit cell structure of both rutile and anatase [11]. The octahedra for rutile are distorted to be slightly orthorhombic. Anatase octahedra are much more distorted, such that their symmetry is less than orthorhombic. For the rutile lattice, the Ti-Ti distances are 3.57 Å and 2.96 Å and the Ti-O distances are 1.949 Å and 1.980 Å. In anatase, the Ti-Ti distances are larger (3.79 Å and 3.04 Å), but the Ti-O distances are shorter (1.934 Å and 1.980 Å). In the rutile structure, each octahedron is in contact with 10 neighboring octahedra (eight sharing corner oxygen atoms and two sharing edge oxygen pairs). This means that half the octahedral sites that are surrounded by O^{2-} ions are empty, giving rise to open "channels" in the structure that run parallel to the *c* axis [12]. These channels allow for small atoms such as H and Li to diffuse into the material [13] along the *c* axis. In anatase each octahedron has only eight neighbors (four sharing corner and four sharing edge oxygen atoms), resulting in a still more open structure. These differences between the two forms explain the differences in their mass densities and

electronic structures (band gap), which are listed Figure 2.1. Both rutile and anatase are transparent and slightly yellow in color. Of the two structures, rutile is the most stable under standard conditions. This stability gives rise to much of its usefulness in catalysis and as a corrosion- or damage-resistant material. The studies presented here explore surfaces of rutile TiO_2, so only its characteristics will be discussed further. Rutile is a uniaxial crystal, such that at room temperature and for a 532 nm source, light polarized with an electric field parallel to the c-axis has $n_{||} = 2.9$, while light polarized perpendicular to this axis has $n_{\perp} = 2.7$ [14]. The space group for the rutile structure is D_{4h}^{14} [15]. The Ti atoms in rutile TiO_2 have a $Ti^{4+}(3d^0)$ electron configuration. The highest filled Ti orbital is the Ti-2p, which lies about 35 eV below the Fermi level [12]. The filled valence band of TiO_2 is predominantly the O-2p level, and the empty conduction band consists primarily of the Ti-3d orbital, with small contributions from the Ti-4s and Ti-4p orbitals. TiO_2 is thus an insulator, or wide band-gap semiconductor, with a measured bulk band-gap of 3.1 eV [16, 17]. Both the conduction and the valence bands have widths of about 5.5 eV [12], and the electron energy gap between these bands is featureless.

Rutile is often bulk-reduced to become a semiconductor. This is achieved by heating the sample to at least 600°C in vacuum or in a H_2 environment. The result is a small number ($\sim$ part per million concentration) of oxygen vacancy defects. It is thought that this occurs as bulk oxygen atoms diffuse to the surface and are released, leaving behind oxygen vacancies [18]. These oxygen vacancies can trap two electrons to form a Ti^{3+}-O-vacancy-Ti^{3+} center and then act as donors, resulting in an n-type semiconductor. Very recent studies, however, suggest that reduction may instead occur as titanium atoms diffuse from the surface into the bulk such that the resulting defects are actually titanium interstitials [19]. The implications of this observation on current understanding of the bulk and surface properties of rutile TiO_2 have not yet been thoroughly explored.

Early ultra-violet photoelectron spectroscopy (UPS) and electron energy loss spectroscopy (EELS) studies on reduced TiO_2 samples showed that the reduction process was accompanied by a small number of states in the band-gap at 0.5-0.7 eV below the conduction band edge [13, 20]. Theoretical calculations that followed [21] predicted that introduction of bulk defects during the reduction process should not produce any observable change in

Figure 2.1: Structure of rutile and anatase TiO_2.

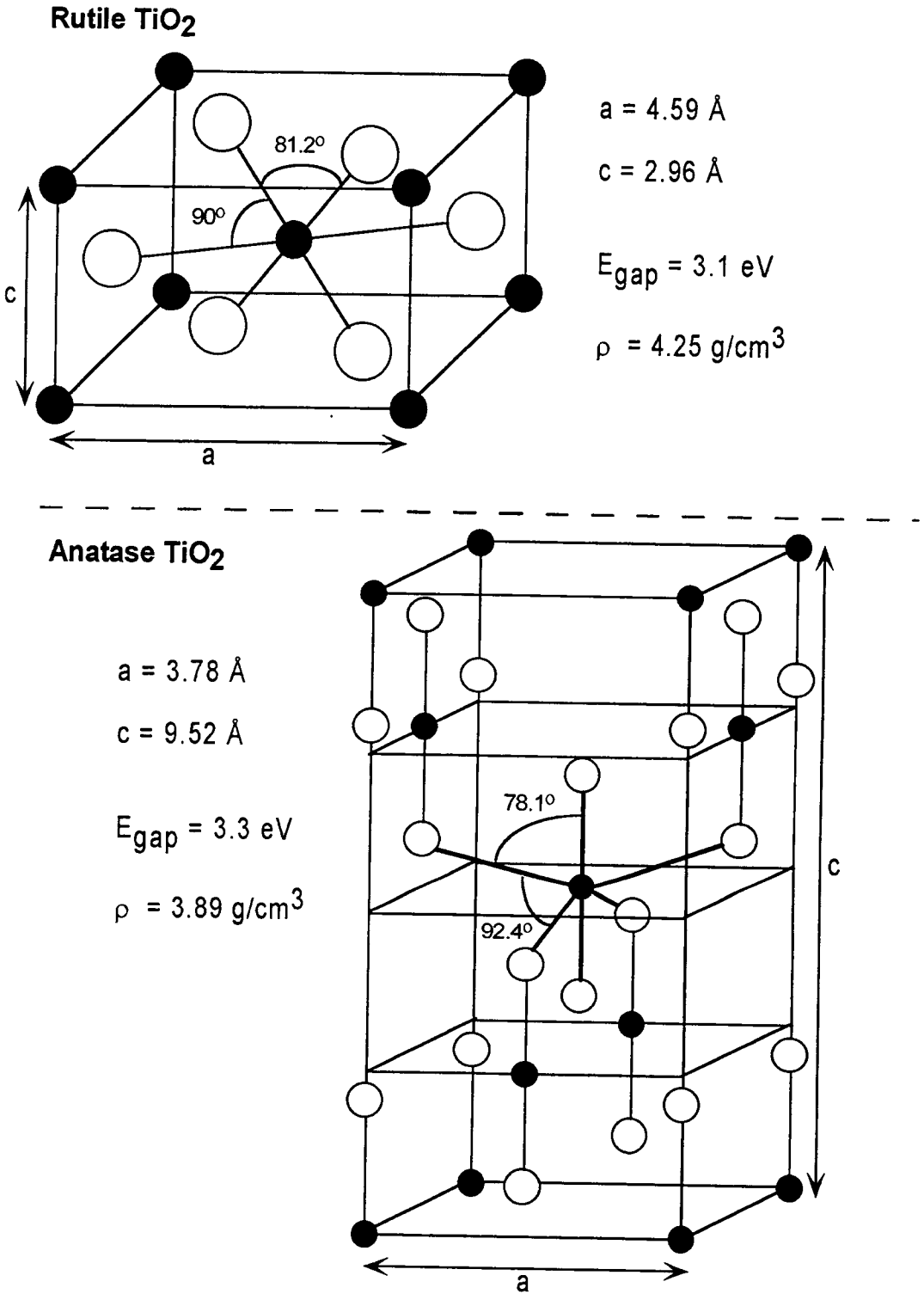

the structure of the gap, and attributed the observed states to surface defects. Later studies showed that the gap states could be produced by argon sputtering the surface and removed by annealing in a low-pressure oxygen environment, confirming that they were surface defect states rather than bulk states produced by reduction [18, 22]. Upon reduction, the Fermi level, which lies close to mid-gap in insulating TiO_2, becomes pinned close to the bottom of the conduction band, giving rise to the observed semiconducting properties.

2.3 The Structure and Properties of Rutile TiO_2 Surfaces

Rutile TiO_2 surfaces have been studied extensively by many researchers using a variety of surface science techniques. LEED studies have been done to determine their structure and thermal stability [12]. Their electronic structure has been explored using EELS, UPS, X-ray photoelectron spectroscopy (XPS), and later scanning tunneling microscopy and tunneling spectroscopy (STM/TS). Surface defects were first observed following bulk reduction using EELS and UPS, as mentioned briefly in Section 2.2 . This discovery largely motivated future surface studies as it became apparent that the defect "signatures" in UPS and XPS spectra could be used as probes of the number of defects present, their nature, and their interactions with molecules in the surrounding environment.

2.3.1 Physical Structure of the Surfaces

Rutile TiO_2 does not cleave well, but the most stable surface is formed when the (110) face of the crystal is exposed. The resulting surface does not represent the atomically flat surface that a cleave would produce, but instead includes a "bridging" oxygen species that corresponds to forming the surface by breaking the minimum number of cation-anion bonds possible. Two cation states exist on such a surface. The first is for Ti atoms bound only to oxygen atoms that would be present on the surface if a pure cleavage were possible. Each of these Ti^{4+} cations is then coordinated to five O^{2-} ligands in a structure with two Ti atoms and two O atoms per unit cell. The second cation state is for Ti atoms that are directly below the "bridging" oxygen atoms. The addition of the rows of bridging oxygen atoms terminates

the semi-infinite cleaved surface and gives rise to Ti atoms with a full complement of six O^{2-} ions. Figure 2.2 shows a schematic drawing of the resulting surface, including three common types of oxygen vacancy defects (surface, bridging, and double bridging). Such surfaces are stable, and do not reconstruct or facet if heated [12]. Other surface orientations, such as (001) and (100), are commonly studied as well. These surfaces are also shown in Figure 2.2. Previous SHG work [23] in this group has focused on the (001) surface in particular. This surface has no bridging species, and all surface titanium atoms are only four-fold coordinated to oxygen ions. The result is a unit cell with two oxygen atoms for each Ti atom. Faceting to (110) and (100) was observed by low-energy electron diffraction (LEED) when sputtered (001) surfaces were heated to between 400 and 800°C [18]. Another study which went to higher temperatures reported temperature dependent reconstruction, with (011) facets in a (2x1) reconstruction observed at 725°C, and (114) facets at over 1000°C [24]. On the (100) surface, all Ti atoms are five-fold coordinated. This surface reconstructs successively upon heating to form (1x3), (1x5), and (1x7) surfaces when heated to 600°C, 800°C, and 1200°C respectively. No faceting was seen at these temperatures. The thermal instability of the (100) and (001) surfaces limits their usefulness. It is desirable to have a technique that allows defect-free, single-crystal surfaces to be re-formed if damaged. For the (110) surface, this can be achieved by argon-ion sputtering the surface and then annealing it at 600°C in a low-pressure oxygen environment. But since (001) and (100) either facet or reconstruct upon heating, no such "recycling" technique exists. For this reason, only TiO_2(110) will be studied here.

2.3.2 Electronic Structure of the Surfaces

The above studies of the physical structure of TiO_2 surfaces have been accompanied by studies of their electronic structure as well. Most studies have indicated that the surface electronic structure and band-gap are indistinguishable from that of the bulk material [12] for all surfaces. In particular the UPS spectra for the (110), (001), and (100) surfaces are nearly identical and very similar to the spectrum for the bulk, even though these surfaces have very different structures [13]. These spectra indicate a surface band-gap of 3.1 eV,

Aigure 2.2: Structure of rutile TiO_2 (110), (001), and (100) surfaces.

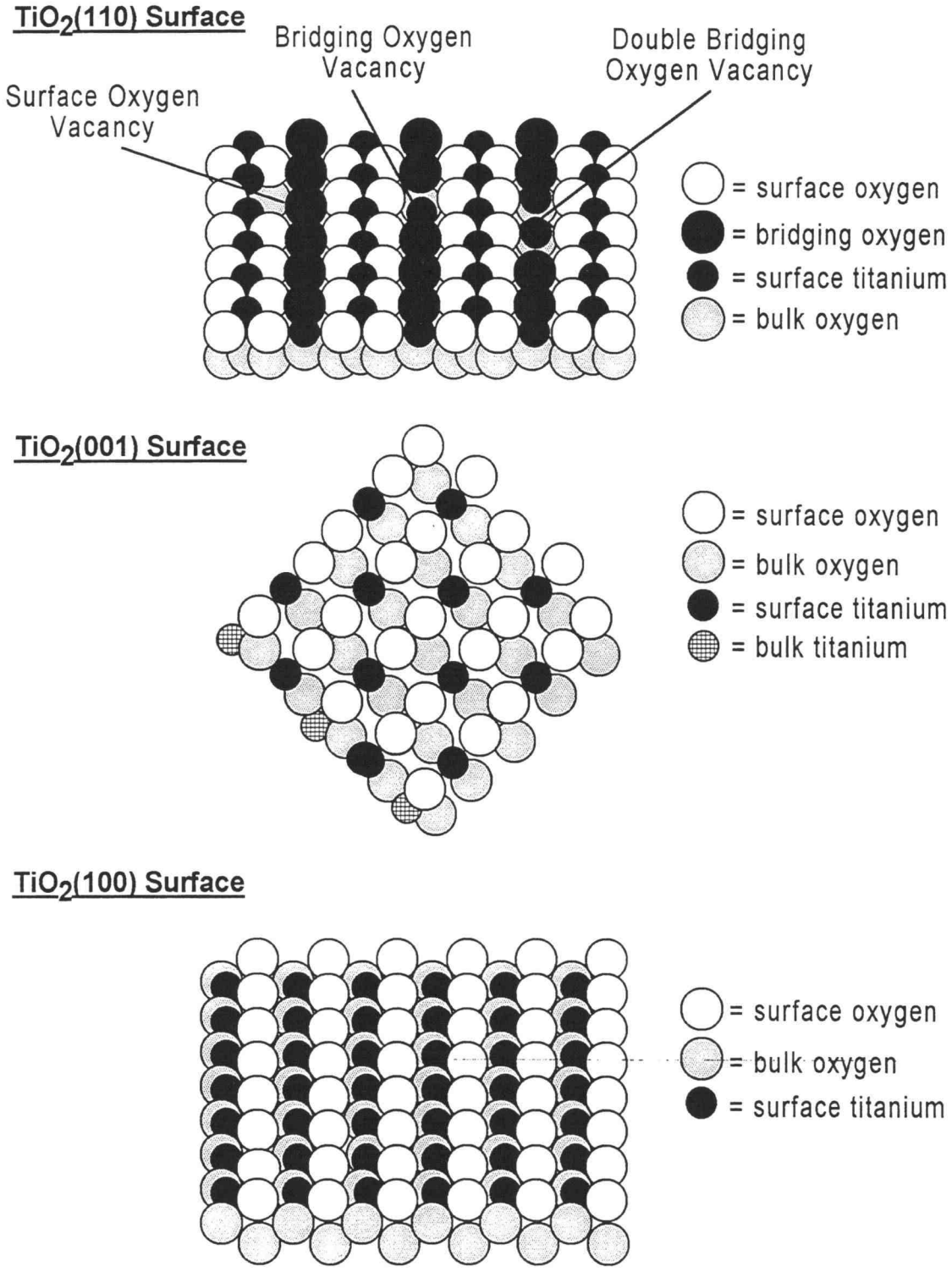

in agreement with the bulk band-gap. But a study of the (110) surface using scanning tunneling microscopy and tunneling spectroscopy (STM/TS) indicates that the surface band gap is 1.6 eV, much narrower than the bulk band-gap [25]. A similar study shows that the surface band-gap varies depending on the number of defects present, with a stoichiometric surface having a band-gap of 3.1 eV and defective surfaces having band-gaps ranging between 1 eV and 2.5 eV [26]. Theoretical calculations that might shed light on this conflict yield conflicting predictions. One study [27] predicts that no surface states should exist in the band-gap on the (110) or (001) surfaces. This would mean that the lower surface band-gap observed in some experiments is only due to defect states, providing explanations for all measured band-gap values. But another study predicts that a large band of intrinsic surface states should exist in the band-gap [28]. This is consistent with measured surface band-gaps below 3.1 eV but provides no explanation for studies that report band-gaps equal to the bulk band-gap or for studies that show variation in the band-gap with defect density.

2.3.3 Surface Defects

As shown in Aigure 2.2, defects on $TiO_2(110)$ surfaces appear when surface or bridging oxygen atoms are absent. Such oxygen vacancies give rise to the surface defect state in the band-gap, observed 0.5-0.7 eV below the Aermi level using UPS [13, 20], as previously mentioned. This state is associated with the Ti-3d level which is unoccupied in a stoichiometric surface, but becomes populated by the electron that is left behind when a Ti^{4+}:O^{2-} bond breaks to leave a Ti^{3+}:O-vacancy site. As more defects are created on a surface using argon-ion sputtering or other means, this defect signature increases in size, making it possible to quantify the number of defects present. Unfortunately, this signature is not sensitive to the type of defect produced. That is, a distinction can not be made between a Ti^{3+} defect formed by a single oxygen vacancy and the Ti^{2+}, Ti^{1+} or metallic Ti^{0} states that appear when more extensive damage is done to a surface. But UPS is most useful in determining the de-localized properties of a material, such as conduction and valence band structures, giving more limited information about localized structures such as defects. XPS, in contrast, probes the core levels of individual atoms in the material. This

makes it a better probe for examining localized defect states. It has been observed [29] that very small (<1/10 monolayer) numbers of oxygen vacancy defects on (110) surfaces can be detected using XPS. This is possible because the removal of an oxygen atom from the TiO_2 lattice to create a defect shifts the energy of the Ti-$2p_{3/2}$ core level of the Ti atom left behind to lower binding energy. This is then detected as a shoulder on the main Ti-$2p_{3/2}$ peak for the remaining unshifted Ti atoms.

When an argon sputtered surface was examined for such shoulders, three distinct defect peaks were seen [29, 30]. One peak was shifted by 1.7 eV to appear at an energy consistent with the Ti^{3+} ions in Ti_2O_3, causing it to be identified as the Ti^{3+} defect peak. Likewise the second peak, which was shifted by 3.1 eV to an energy consistent with Ti^{2+} atoms in TiO, was identified as a Ti^{2+} defect peak. This is thought to occur as Ti^{3+} defects pair to form local Ti_2O_3-like structures. The third peak was shifted by 4.1 eV to a metallic energy, and corresponds to Ti^{0+} defects in the lattice. No peak consistent with Ti^{1+} defects was seen on the (110) surface. Curve-fitting the spectrum containing the main peak and these three defect peaks allows for the relative number of defects of each type to be determined.

Prior to the work in this thesis, three means for creating defects on TiO_2(110) surfaces were observed using XPS. The defect states previously seen by UPS were present on the surface after thermal annealing to 600°C in vacuum, but absent if the surface was annealed in a low-pressure oxygen environment. XPS shows that these thermally produced defects are Ti^{3+} in type and not very extensive [30]. Low-energy electron bombardment also produces defects on these surfaces [29] which are of Ti^{3+} type only. This technique produces much more damage than thermal annealing, but still only a very small amount. In contrast, argon sputtering produces defects of all three possible types, though predominantly of Ti^{3+} type. Argon sputtered surfaces are also much more severely damaged than either electron-beam damaged or thermally annealed surfaces. Aor all damaged surfaces, exposure to O_2 resulted in the rapid restoration of surface stoichiometry, as witnessed by the disappearance of the UPS defect signature. XPS studies confirm this for thermal defects and electron-beam damage, but also show that only partial healing appears on the argon-sputtered surface. This suggests that both thermal and electron-beam created defects are limited to the topmost surface layer, while argon-sputtering causes extensive damage over multiple

layers. Since XPS probes more deeply into the material than UPS, the damaged underlayers still appear in the XPS spectrum after the O_2 exposure has healed the topmost surface layer. More discussion of the creation and observation of defects on these surfaces can be found in Sections 3.5.2.3, 4.3.6, and 5.2.2.

2.4 Interactions Between Small Molecules and TiO_2 Surfaces

Most studies of interactions between TiO_2 surfaces and small molecules focus on determining whether the molecules in question adsorb on the surface either at room or at low temperature. Some studies then compare molecular adsorption on surfaces with defects to that observed on shoichiometric surfaces. Typically, the interest in these studies is on monitoring the chemistry of the adsorbed species, such that the fate of defects after adsorption is not tracked. The research in this thesis will suggest that both aspects of the interaction between surfaces and molecules should be monitored because in some cases the valence state of the defect remains unchanged despite molecular adsorption while in others the defect is "healed" so that it again has a shoichiometric Ti^{4+} valence. In this section, current literature addressing interactions between $TiO_2(110)$ surfaces and small molecules will be presented. As this discussion will show, very little consensus has been reached concerning the mechanisms that drive such reactions. Studies of adsorption at low temperatures will be briefly mentioned, but not emphasized, since all work presented in this thesis is done at room temperature.

2.4.1 Oxygen Adsorption

Many experiments show that stoichiometric rutile $TiO_2(110)$ surfaces do not interact with O_2 at room temperature [31, 32, 33]. (O_2 does adsorb on these surfaces at low temperature (105 K) [34], however, and is subsequently seen to have two different thermal desorption states (164 K and 416 K) [35]. Isotope labeling shows that there is no mixing between adsorbed oxygen and surface lattice oxygen, suggesting that only physisorption is occurring.) But surfaces with defects do react strongly with O_2 such that surface Ti^{3+}

defect sites are eliminated by O_2 exposure. The mechanism for this defect "healing" by O_2 remains under debate. Some groups contend that the O_2 simply dissociates to physically heal the defect with the needed O^{2-} ion [32], resulting in a stoichiometric surface. Others argue that a charge transfer between the Ti^{3+} defect and an intact O_2 molecule results in a Ti^{4+}:O_2^- complex [36]. Such a chemisorbed complex would represent "electronic" healing of the surface, that is the electronic signature of the Ti^{3+} defect is gone and the Ti atom now appears fully coordinated, but does not constitute "physical" healing of the defect. This would create difficulties in surface analysis because surfaces with such defect-molecule complexes would be indistinguishable from surfaces that were truly stoichiometric (using conventional surface science techniques). Results in this thesis and in the previous (001) studies by our group [23] provide additional insight into this debate.

2.4.2 H_2 Adsorption

Conflicting reports concerning H_2 adsorption on TiO_2(110) surfaces can be found in the literature. Stoichiometric surfaces have been shown to be inert to H_2 [13, 36], and some studies indicate that surfaces with defects also do not interact with hydrogen [13, 23]. But other groups [31, 36] have observed that H_2 will dissociate on the surface and interact with a defect to form titanium hydride complexes (Ti^{4+} :H^-). These reports also include the observation of a very low sticking coefficient ($1x10^6$) for H_2 at room temperature, which may be responsible for other groups not observing this process [36]. Diffusion of the adsorbed hydrogen into the bulk was also observed [13], as previously mentioned in Section 2.2. One group reported enhancement of H_2 adsorption when low-energy H_2^+-ions were used to bombard the sample [31].

2.4.3 H_2O Adsorption

A great deal of research has been done to explore the interaction between H_2O and TiO_2 surfaces since photocatalytic decomposition of water on TiO_2 electrodes was observed [1]. These studies have found that water adsorbs on the surface molecularly only below 160

K. Heating such a surface results in molecular desorption of most of this water between 170-180 K. The small amount of remaining water is adsorbed dissociatively as hydroxyl groups which are not completely removed from the surface until it is heated to 350-400 K [32]. When surfaces were exposed to water at room temperature, no molecular H_2O adsorption was observed, and only a sub-monolayer coverage of hydroxyl groups was detected [37]. The surface used for this study was slightly defective, so it was thought that a defect provided the adsorption site for each hydroxyl. Later studies [31, 32], however, showed that hydroxyl adsorption was independent of defect coverage, and suggested that the defect density actually increased slightly with hydroxyl adsorption. On the basis of these observations, it was suggested that molecular H_2O reacts with a bridging oxygen atom to form two hydroxyl groups that then adsorb on the surface. This would create a defect where the bridging oxygen atom was, accounting for the additional observed defects, but requires that the adsorbed hydroxyl groups do NOT form complexes with defects of the type proposed for O_2 and H_2. A very recent study [38], which overlaps chronologically with the research presented in this thesis and confirms our observations, shows that D_2O molecules can be reduced by Ti^{3+} defects on the surface at room temperature to form D_2 and a healed defect. The unfortunate result of all of this research is that experimental evidence exists that suggests that water (1) does not interact with defects, (2) creates defects and (3) removes defects. This provides clear motivation for further study.

2.4.4 CO and CO_2 Adsorption

Both CO and CO_2 adsorb only very weakly on stoichiometric TiO_2 surfaces [36]. On surfaces with defects no additional CO_2 adsorption is seen, but CO is found to adsorb at the defect sites. The study does not specify whether this adsorption at a defect site is accompanied by removal of the defect signature, indicating that a defect-molecule complex such as Ti^{4+}:$(CO)^-$ or the like has formed. They do, however, observe that in some cases an adsorbed CO molecule interacts with a neighboring bridging oxygen atom to form CO_2 that then desorbs, resulting in an additional defect. These observations have the support of theoretical work in which *ab initio* molecular orbital calculations predict the strong

interaction between CO and defects [39]. Low temperature studies of CO on TiO_2 surfaces show only weak adsorption of CO on nearly defect-free surfaces below 150 K [34]. Two desorption states are seen following this adsorption [35]. These were attributed to CO interacting with surface oxygen atoms through the C-end of CO and CO interacting with defects through the O-end of the molecule.

2.4.5 NO and SO_2 Adsorption

Studies of TiO_2 powders at room temperature show that fully oxidized surfaces interact only weakly with NO. When damaged, these same surfaces react strongly to NO, such that the defect signature of the surfaces vanishes [40]. On these damaged powders, both molecular and dissociative adsorption states were identified, though, making it unclear whether defects were physically healed by a dissociated oxygen ion from an NO molecule or were only electronically healed by the formation of Ti^{4+}:$(NO)^-$ complexes. That dissociation products were present strongly suggests that physical healing occurred. No evidence conclusively shows this, however, and there remains no explanation for the presence of a larger number of molecular sites than appear on defect-free surfaces. In this case, it is possible that both types of healing are taking place. The complex topography of powder surfaces provides the additional concern that adsorption at steps may be taking place. At steps, oxygen-vacancy defects are likely to be more complex, allowing for reactions that would not occur on single-crystal surfaces. No room temperature results of NO on single-crystal samples have been reported.

At low temperature, NO is seen to adsorb only weakly on single-crystal (110) surfaces [38]. The adsorbed NO then desorbs at 120 K. But additional desorption of N_2O was seen at 169 K and 250 K. This was thought to happen in two steps, with the adsorbed NO interacting with a defect first (NO_a + vacancy $\rightarrow$ N_a + $O_{lattice}$) and then through interaction of the generated adsorbed nitrogen atom and another adsorbed NO (N_a + NO_a $\rightarrow$ N_2O). This discussion suggests that such an interaction requires a surface with a number of defects, and that the interaction results in physical healing of these defects. But it is important to note here that the existence and behavior of defects on this surface was not monitored. Aor

this reason, the mechanism proposed must be considered speculation. Evidence supporting this mechanism does exist, however, in similar TPD studies done on surfaces that were intentionally damaged [41]. Here more N_2O and N_2 reduction products were seen when more defects were created. For heavily damaged surfaces, no NO desorption was observed at all, with all desorption in the form of the products N_2O and N_2. But again, the fate of the defects was not determined in any direct fashion. Confirmation that the above mechanism is correct only comes from the direct observation of defect healing seen in the powder studies above.

Interaction between SO_2 and $TiO_2(110)$ surfaces have been studied as well [42]. Here direct observation of defect states show that surfaces with no defects do not react with SO_2, while surface with defects react strongly with SO_2 until all defect signature vanishes. This study suggests this happens by dissociation of the SO_2 to physically heal the defect. But in another study SO_3^{2-} was detected on the surface [43], pointing to the possibility of defect healing through a molecule-defect complex.

2.4.6 NH_3 and H_2S Adsorption

When stoichiometric $TiO_2(110)$ surfaces were exposed to NH_3, the NH_3 adsorbed in molecular form to reach a saturation coverage of ~0.16 monolayer (1 monolayer coverage represents 1 NH_3 molecule per surface atom). If surfaces with a large number of defects were examined, NH_3 adsorption was seen to be nearly the same, but a slightly higher coverage of ~0.19 monolayer [44]. A similar study showed similar coverages, but with slightly less NH_3 adsorption on surfaces with defects [45]. These opposing results suggest that it is unlikely that any interaction between defects and NH_3 occurs, with the slight variations in both studies being insignificant. But here again the number of defects present was not determined or monitored.

Interactions between H_2S and surfaces with defects were studied using UPS and XPS [46]. At low coverages, a small state appeared in the UPS spectrum that was consistent with sulfur ions bound to titanium cations in what was tentatively identified as a TiS_2-like structure. This would suggest dissociation of the H_2S molecules and reaction with

defects. A slight decrease in the number of defects accompanied this state, suggesting that some defect healing was taking place, but complete healing (as was seen for SO_2) did not occur. In addition, no defect healing or sulfur signature was seen using XPS. At larger exposures, molecular adsorption of H_2S in small quantities was detected, but again with only small changes in the number of defects observed using UPS and no changes observed using XPS. This leads to the overall conclusion that defective surfaces do not react strongly with H_2S. Why a small number of defects heal is unclear, but several possible situations could account for this behavior. Airst, it is possible that the observed defect healing could be happening only at defects on steps, which would react in a much more complicated fashion than defects on the crystal surface. This would allow for small, anomalous, defect interactions that are not observed on the pristine surface. Second, since the study was done on argon-sputtered surfaces, it is also possible that the interaction occurs only at the higher valence defect sites (Ti^{2+} or Ti^{0+}). Interaction with these defects could decrease the UPS defect signature, but might not alter the XPS peaks enough to be detected. This is possible because the XPS peaks for higher-valence defects are very small, such that small changes in them could be within experimental noise. But the XPS spectra were not included in the above study, with the authors stating that there was no observable difference in these spectra after H_2S exposure, so that this hypothesis can not be checked. Third, the small amount of defect healing could be explained if a small amount of H_2S dissociation resulted in the formation of Ti^{4+}:H^-, Ti^{4+}:S^- or Ti^{4+}:$(S_2)^-$ complexes. But since only a small amount of defect healing was seen even for large H_2S exposures, such dissociation would need to be a highly unfavorable interaction. Additional research presented in the above study shows that surfaces that defective have been exposed to large doses of H_2S interact weakly with O_2 thereafter. This suggests that the predominant interaction occurs as adsorbed molecular H_2S coordinates with defects without healing them, but making them inaccessible for future healing by O_2.

2.4.7 Organic Molecules

Many studies have been done to characterize reactions between organic molecules and surfaces of shoichiometric or damaged TiO_2. Oxygen-containing organic molecules commonly undergo dehydration, dehydrogenation, deoxygenation, and self-disproportionation reactions when exposed to TiO_2 surfaces. Aor example, deoxygenation of alcohols [47, 48], of ketones [49], and of aldehydes [50] has been observed in the presence of defects on $TiO_2(110)$ single crystal surfaces, TiO_2 powders, and other surfaces. Aor aldehydes, defect sites convert aldehyde (RCH=O) molecules to olefins (RCH=CHR). In all surface-organic reactions, removal of surface oxygen atoms or deposition of oxygen from the organic molecule to fill a defect site are central to the interaction. The many studies that have been done focus heavily on the chemistry of the reaction process in a descriptive way, trying each group of organic molecules in turn and determining how they are modified by interaction with the surface. Aew studies look at such interactions in a comprehensive and predictive fashion.

2.4.8 Summary

Some property or set of properties of the molecules studied must govern their interaction with TiO_2 surfaces. These factors would determine whether a molecule will interact with defects to cause defect healing (O_2 and SO_2), interact with surface oxygen atoms to create defects (NO and possibly H_2O), adsorb intact without interacting with defects (NH_3 and possibly H_2S) , or adsorb dissociatively without interacting with defects (possibly H_2O). So far, studies have focused on characterizing the chemistry of the interactions without pinpointing what drives them. One motivation for the work in this thesis is the search for the determining factor that dictates what form a surface-molecule interaction will take for a given molecule.

2.5 Photophysics of Small Molecules on TiO_2 Surfaces

Many experiments have demonstrated that TiO_2 is very photoactive. The wealth of catalysis research that has been done following the first reports of water splitting [1] is a

testimony to the diversity of interactions that can occur when TiO_2 surfaces are irradiated by UV light in the presence of molecules. The traditional mechanism invoked to explain photocatalytic processes on TiO_2 surfaces is that UV radiation excites an electron-hole pair in the bulk TiO_2 material just below the surface. The electron and hole then migrate to the surface, where they become available for interactions with molecules in the surrounding environment. The charge transfer that occurs during these interactions destabilizes the molecule in question, leading to its decomposition and to the formation of the observed reaction products. This mechanism leaves the physical structure of the surface unchanged during the interaction, with no creation or healing of defects allowed. Many processes of this type have been conclusively observed, including reactions where one molecular species reacts with generated holes while another reacts with generated electrons. Reference [11] provides a comprehensive and detailed review of such processes.

The unfortunate consequence of having such an established mechanism to explain the observed interactions is the tendency to invoke this mechanism for *every* reaction observed on the surface. The work in this thesis, and in previous research from this group [23], shows that irradiating TiO_2 surfaces with UV light creates surface oxygen vacancy defects. Since many of the molecules discussed in the previous section interact strongly with such defects, a second possible mechanism for observed interactions in the presence of UV must be considered. It is now possible that UV creates a defect on the surface which becomes a site for future interactions that do not rely on the UV creation of electron-hole pairs. Even the photo-assisted splitting of water, considered the first catalytic decomposition observed on these surfaces, has since been demonstrated to occur by this alternative mechanism [51, 52].

To obtain catalytic decomposition of water using the first mechanism, other materials must be deposited on the TiO_2 surface. Typically this involves depositing both metal particles (such as Pt) and oxide (such as RuO_2) particles on the surface. Then above band-gap UV illumination injects electrons into the metal and holes into the oxide. Trapped electrons in the metal then reduce water to from H_2, while trapped vacancies in the oxide oxidize water to form O_2 [53]. Other clever modifications to the surface that similarly result in the separation of UV generated electron-hole pairs have also been developed [4, 5, 6, 7].

With the creation of viable photo-electrochemical cells as the primary motivation for this research, it is not surprising that research has turned from study of pristine TiO_2 surfaces to study of more complicated systems.

This thesis returns focus to interactions that follow the second mechanism. The motivations here are (1) to understand the mechanism by which UV can create defects on a defect-free surface, and (2) to explore interactions between such defects and small molecules in an attempt to understand and finally predict what reactions will occur based on the properties of the molecule. Careful search of the literature unearths studies which demonstrate that UV can create defects on TiO_2 surfaces. Such reduction was observed on anatase powders [54, 55], and even on rutile (110) surfaces [56], but invoked little comment. The mechanism for this defect creation remains under debate. Direct photodesorption of lattice (or bridging) oxygen atoms is considered unlikely based on energetics. TiO_2 surfaces are quite stable, so it is reasonable to assume that surface atoms are bound by more energy than 3.1 eV. Aor similar reasons, UV generation of electron-hole pairs is not likely to lead to breaking of surface Ti-O bonds.

Several sources in the literature report the existence of chemisorbed molecular oxygen on the surface, providing a possible avenue for UV defect creation. In one study [57], rutile powder was treated to have thermal defects and then exposed to isotope $^{18}O_2$ at low temperature. Upon heating, desorption peaks for $^{18}O_2$ were seen, but no peaks for lattice oxygen or isotopic exchange with the lattice were seen. The authors proposed that molecular oxygen chemisorbed on the surface intact as O_2^-. Since many experiments demonstrate that defects react strongly with O_2, it is reasonable to assume that this adsorption occurred at defect sites and was accompanied by a charge transfer to form Ti^{4+}:$^{18}O_2^-$ complexes. But since defects were not monitored during this experiment, this can not be confirmed. This study also showed that exposing the isotope-covered surface to UV results in intact desorption of the $^{18}O_2$ for photon energies above the band gap. This suggests that UV can create defects by generating an electron-hole pair that then interacts with O_2^- adsorbed at defects sites. A recent study on TiO_2(110) surfaces, concurrent with the research in this thesis, observed the same behavior, and also reported no isotopic mixing even when a mixture of $^{16}O_2$ and $^{18}O_2$ was adsorbed on the surface [34]. This is strong evidence for

intact adsorption of molecular oxygen at defect sites. In this thesis, UV-induced defect creation will be demonstrated on surfaces that appear "defect-free" using XPS and UPS. This suggests either that "defect-free" surfaces are really covered with a substantial number of undetectable Ti^{4+}:O_2^- complexes or that some mechanism exist by which UV light can remove surface lattice (or bridging) oxygen atoms. In the first case, all studies of single-crystal surfaces deemed "defect-free" by techniques that measure their electronic structure must be called into question. Such surfaces may demonstrate ideal electronic structure without being truly stoichiometric.

CHAPTER 3
TECHNIQUES USED FOR SURFACE STUDY

3.1 Overview

Each of the surface science techniques used in this research provides unique information about the structure, properties, and behavior of surfaces studied. Circumstances dictate which techniques are most useful, depending on the external conditions of interest, and the type of information sought.

Most conventional surface science techniques rely on the detection of electrons or ions emitted from a surface, such that surfaces are necessarily studied in ultra-high vacuum (UHV) chambers. It is reasonable to question attempts to extrapolate surface behavior observed in UHV to realistic environments such as atmospheric-pressure and solution. For this reason, the development of surface science techniques which bridge the gap between the pristine world of the UHV chamber and the more complicated environments that surround us is essential. Optical probes are ideal for this purpose, since light can impinge on and be collected from a sample surface through a surrounding transparent medium. Optical signals arising from the surface of a sample then sometimes can be separated from contributions arising from both the bulk and the surrounding media. This allows information about surface structure and behavior in realistic environments to be gathered. Careful comparisons between more conventional UHV studies and optical studies in varied environments provide the link that allows future UHV work to be extrapolated to "real-world" applications.

Before the invention of the laser, the information that could be obtained by optical probes was limited. The low power of conventional light sources meant that only linear optical properties could be observed. Selection rules dictated that only a few electronic or vibrational transitions could be probed using linear optical techniques. Even then, surface signals were so small compared to bulk signals that separating the two was difficult. The introduction of the laser made possible the study of nonlinear optical behavior of materials. With two-, three-, and multi-photon events now common, selection rules allow all other states to be probed. Symmetry rules for nonlinear response could also be exploited to

separate bulk response from surface response, allowing for surface-specific nonlinear optical studies of materials.

The nonlinear optical response of a material depends on both its electronic structure (through resonance enhancement) and its physical structure (though symmetry arguments). Conventional surface probes usually are sensitive to only one of these factors, with the result that experiments using one technique may show changes in a material that do not appear using another. For example, a change in the LEED pattern (sensitive to surface symmetry) of a surface occurs during a reconstruction, but this is not necessarily accompanied by a detectable change in the XPS spectrum (sensitive only to electronic structure). Conversely, the introduction of a small number of electronic defects to a surface, detectable using XPS, will likely not result in any observable change in its LEED pattern. A nonlinear optical probe such as second harmonic generation, however, would be sensitive to either change, demonstrating its value as a surface science probe.

The following sections discuss the theory behind the experimental techniques used for surface studies presented here. Discussion of the phenomenological basis for surface-SHG is extensive. This is intentional and warranted considering the relative novelty and complexity of the technique as compared to the more conventional surface science probes that are discussed in later sections. XPS and UPS are discussed from a more practical perspective, with emphasis placed on how spectra are used to explore the structure of TiO_2 surfaces. Excellent discussions of these techniques are common in the literature [58], and will not be reproduced in detail here.

3.2 Nonlinear Optical Processes

Second Harmonic Generation (SHG) is a second-order nonlinear interaction between light and matter. Such nonlinear processes occur when very intense electromagnetic fields alter the optical properties of a material system from their expected linear behavior. Interactions of this type only occur appreciably at very high field strengths. For this reason, the observation of nonlinear optical effects, including SHG, did not occur until the advent of the laser. In fact, the beginning of the field of nonlinear optics can be identified as the

experimental discovery of second harmonic generation [59] in 1961, shortly after the first working laser, the ruby laser, was invented in 1960 [60].

Conventional optics describes only linear interactions between materials and electromagnetic radiation. At low light intensities such as those commonly found in nature, optical properties of materials remain only linearly dependent on the intensity of illumination. Here the interaction between light and matter occurs as the incident electric field induces a polarization in the material. This polarization is proportional to the electric field, and the proportionality tensor is a response function known as the *electric susceptibility* $\tilde{\chi}^{(1)}$. For time-harmonic fields, this can be expressed as

$$\vec{\mathbf{P}}^{(1)}(\omega) = \tilde{\chi}^{(1)}(\omega) : \vec{\mathbf{E}}(\omega). \tag{3.1}$$

The induced polarization gives rise to an induced current density through a term in the usual multipole expansion

$$\vec{\mathbf{J}} = \vec{\mathbf{J}}_{cond} + \frac{\partial \vec{\mathbf{P}}}{\partial t} + c\vec{\nabla} \times \vec{\mathbf{M}} - \frac{\partial}{\partial t}(\vec{\nabla} \cdot \vec{\mathbf{Q}}) + \cdots \tag{3.2}$$

which can then be used as a source term in Maxwell's equations

$$\begin{aligned} \vec{\nabla} \times \vec{\mathbf{B}} &= \tfrac{1}{c}\tfrac{\partial \vec{\mathbf{E}}}{\partial t} + \tfrac{4\pi}{c}\vec{\mathbf{J}} & \vec{\nabla} \cdot \vec{\mathbf{B}} &= 0 \\ \vec{\nabla} \times \vec{\mathbf{E}} &= -\tfrac{1}{c}\tfrac{\partial \vec{\mathbf{B}}}{\partial t} & \vec{\nabla} \cdot \vec{\mathbf{E}} &= 4\pi\rho. \end{aligned} \tag{3.3}$$

Recalling the expression for charge conservation $\vec{\nabla} \cdot \vec{\mathbf{J}} + \frac{\partial \rho}{\partial t} = 0$, and ignoring magnetic and electric quadrupole terms in the expansion of Equation 3.2 (this is the electric dipole approximation), Maxwell's equations become:

$$\begin{aligned} \vec{\nabla} \times \vec{\mathbf{B}} &= \tfrac{1}{c}\tfrac{\partial}{\partial t}\left(\vec{\mathbf{E}} + 4\pi\vec{\mathbf{P}}\right) + \tfrac{4\pi}{c}\vec{\mathbf{J}}_{cond} & \vec{\nabla} \cdot \vec{\mathbf{B}} &= 0 \\ \vec{\nabla} \times \vec{\mathbf{E}} &= -\tfrac{1}{c}\tfrac{\partial \vec{\mathbf{B}}}{\partial t} & \vec{\nabla} \cdot \left(\vec{\mathbf{E}} + 4\pi\vec{\mathbf{P}}\right) &= 0. \end{aligned} \tag{3.4}$$

Now the polarization is the only time-varying source term in Maxwell's equations, and solution of these equations yields the linear response of the medium [61, See Chapter 1].

The approach for nonlinear interactions between matter and fields is similar to the above. But now, the polarization induced in the medium can be expressed as an expansion in progressively higher orders of the field strength, given by [62, See Chapter 1]

$$\vec{\mathbf{P}}(\omega, 2\omega, 3\omega, \cdots) = \vec{\mathbf{P}}^{(1)}(\omega) + \vec{\mathbf{P}}^{(2)}(2\omega) + \vec{\mathbf{P}}^{(3)}(3\omega) + \cdots \tag{3.5}$$

where

$$\begin{aligned} \vec{\mathbf{P}}^{(1)}(\omega) &= \tilde{\chi}^{(1)}(\omega) : \vec{\mathbf{E}}(\omega), \\ \vec{\mathbf{P}}^{(2)}(2\omega) &= \tilde{\chi}^{(2)}(2\omega, \omega, \omega) : \vec{\mathbf{E}}(\omega)\vec{\mathbf{E}}(\omega), \\ \vec{\mathbf{P}}^{(3)}(3\omega) &= \tilde{\chi}^{(3)}(3\omega, \omega, \omega, \omega) : \vec{\mathbf{E}}(\omega)\vec{\mathbf{E}}(\omega)\vec{\mathbf{E}}(\omega). \end{aligned} \tag{3.6}$$

The first-order term of this expression is just the linear response of the material. The second-order term represents generation of an induced polarization at twice the fundamental frequency. In the same manner, the third-order term gives rise to an induced polarization at the third harmonic. Expansion in this fashion leads to a separate set of Maxwell's equations for the fields produced at each frequency. This allows for direct calculation of the field generated at the second harmonic during the interaction between the incident field and the material.

This can be generalized to include other nonlinear processes by considering the case where the light that interacts with the material in question consists of two (or more) distinct frequency components. The field incident on the material then can be written

$$\vec{\mathbf{E}}(t) = \vec{\mathbf{E}}_1 e^{-i\omega_1 t} + \vec{\mathbf{E}}_2 e^{-i\omega_2 t} + c.c., \tag{3.7}$$

and the induced polarization in the material becomes

$$\vec{\mathbf{P}}(t) = \tilde{\chi}^{(2)}(\vec{\mathbf{E}}(t))^2. \tag{3.8}$$

The resulting polarization that arises from squaring the complex field has five terms, each with a different frequency, representing five second-order nonlinear responses of the material. The amplitudes of these terms are given by

$$\begin{aligned} \vec{\mathbf{P}}(2\omega_1) &= \tilde{\chi}^{(2)} : \vec{\mathbf{E}}_1^2 && (SHG) \\ \vec{\mathbf{P}}(2\omega_2) &= \tilde{\chi}^{(2)} : \vec{\mathbf{E}}_2^2 && (SHG) \\ \vec{\mathbf{P}}(\omega_1 + \omega_2) &= 2\tilde{\chi}^{(2)} : \vec{\mathbf{E}}_1\vec{\mathbf{E}}_2 && (SFG) \\ \vec{\mathbf{P}}(\omega_1 - \omega_2) &= 2\tilde{\chi}^{(2)} : \vec{\mathbf{E}}_1\vec{\mathbf{E}}_2^* && (DFG) \\ \vec{\mathbf{P}}(0) &= 2\tilde{\chi}^{(2)} : \left(\vec{\mathbf{E}}_1\vec{\mathbf{E}}_1^* + \vec{\mathbf{E}}_2\vec{\mathbf{E}}_2^*\right) && (OR). \end{aligned} \tag{3.9}$$

where each amplitude is labeled with the physical process it represents, i.e. second harmonic generation (SHG), sum frequency generation (SFG), difference frequency generation (DFG), and optical rectification (OR). These processes are known as three-wave mixing processes, counting the two incident and one generated fields. Each polarization term leads to a set of Maxwell's equations (Equation 3.4) that are valid for that frequency component. Solution of these equations yields the nonlinear response of the material.

When the above process of generalization is applied to the third order susceptibility tensor, four-wave mixing processes such as third harmonic generation, coherent anti-stokes raman spectroscopy (CARS) and others directly follow. Of the resulting multitude of non-linear optical processes that can be used to probe the optical properties and structure of materials, the appropriate technique to study the system in question must be chosen. This choice is made by considering the physical symmetry of the material to be studied. Often symmetry arguments dictate that one process is forbidden in a material such that another can be isolated. The locations of electronic or vibrational states of interest also dictate which techniques will be useful. Resonances will occur whenever the photon energies can be tuned to a real electronic or vibrational level in the material system (see Section 3.4.4). This means that vibrational states are best studied by DFG or CARS techniques where subtraction of optical frequencies allows resonances at small frequencies to be probed. Likewise SHG, SFH, third harmonic generation, and other techniques where direct summing of optical frequencies occurs are best used to study electronic states that are spaced at energies corresponding to optical frequencies. These concerns lead to the choice of SHG as a probe of electronic states on surfaces of materials with inversion symmetry, as discussed in the next section.

3.3 Surface Second Harmonic Generation

3.3.1 Symmetry Arguments and Surface Specificity

Since susceptibility tensors characterize the physical behavior of a material, they can be expected to reflect the symmetry of that material. In centrosymmetric media for example, opposite directions are completely equivalent (the material has *inversion symmetry*). This

means that the polarization induced by an electric field should change sign if the electric field is reversed. But Equation 3.6 dictates that the second-order induced polarization does *not* change sign if the electric field is reversed since this polarization depends on the square of the electric field. This leads to the relation $\vec{\mathbf{P}} = -\vec{\mathbf{P}}$, which can only be satisfied if $\vec{\mathbf{P}} = 0$. This dictates that $\tilde{\chi}^{(2)} = \mathbf{0}$ for materials with inversion symmetry. Thus no second harmonic signal can arise from a bulk sample of centrosymmetric material. (This relies on the electric dipole approximation. If quadrupole terms are present, a second harmonic signal from the bulk can occur that must be separated from the surface signal.)

It is for centrosymmetric materials that SHG demonstrates its value as a surface science technique. Inversion symmetry is necessarily broken at a boundary between a centrosymmetric material and another medium, leading to an interface-specific second harmonic signal that is not accompanied by any contribution from the bulk. The theoretical formalism for understanding the interaction between light and surfaces of nonlinear media was first developed by Bloembergen and Pershan [63]. Discussions of SHG in bulk materials can be found in many nonlinear optics texts [61, 64, 65, 62, 66]. Detailed discussions for surface-specific SHG are less common, and usually found as journal articles rather than in texts (see [67] for the most complete treatment). For this reason, much of the theoretical development of SHG as a surface science probe will be included here.

The experimental history of surface SHG is also of interest. After the theoretical framework for the technique was established, the surface-specificity of this technique was demonstrated for many centrosymmetric materials [68, 69, 70]. In addition, SHG was able to detect molecular adsorption on metals with submonolayer sensitivity [71, 72]. But these initial observations went largely unnoticed until surface enhanced Raman scattering on noble metals was discovered [73] in 1974. The usefulness of this technique led researchers to re-examine SHG as a surface probe [74]. The conclusion was that even without the surface enhancement relied on for surface Raman work, SHG was capable of detecting molecular adsorption on the surface of any centrosymmetric material [75]. Since its rediscovery, SHG has been applied to almost all subfields of surface science, with the promising recent application to surface electrochemistry. (See [76] for an excellent recent review of SHG as a probe of surface chemistry.)

3.3.2 The Nonlinear Plane-Parallel Slab Model of Surface SHG

The above symmetry argument leads to the conclusion that SHG always occurs on surfaces. This is because inversion symmetry is always broken, at least along the surface normal, when the material is truncated. The top few surface layers may then contribute to a nonlinear susceptibility that gives rise to harmonic generation from the surface. Both inside the material and out, Maxwell's equations must be valid for all the fields. In addition, the boundary conditions implied by the surface must be satisfied. For each frequency component, Maxwell's Equations can be written (for a lossless, nonlinear, dielectric material) as

$$\begin{aligned} \vec{\nabla} \times \vec{\mathbf{H}} - \tfrac{1}{c}\tfrac{\partial \vec{\mathbf{D}}}{\partial t} = 0 \qquad & \qquad \vec{\nabla} \cdot \vec{\mathbf{B}} = 0 \\ \vec{\nabla} \times \vec{\mathbf{E}} + \tfrac{1}{c}\tfrac{\partial \vec{\mathbf{B}}}{\partial t} = 0 \qquad & \qquad \vec{\nabla} \cdot \vec{\mathbf{D}} = 0. \end{aligned} \tag{3.10}$$

Here the auxiliary fields $\vec{\mathbf{H}}$ and $\vec{\mathbf{D}} = \vec{\mathbf{E}} + 4\pi\vec{\mathbf{P}}$ have been introduced. For non-magnetic materials, $\vec{\mathbf{H}} = \vec{\mathbf{B}}$. For second harmonic generation, the electric displacement $\vec{\mathbf{D}}$ can be written as

$$\begin{aligned} \vec{\mathbf{D}} &= \vec{\mathbf{E}} + 4\pi\vec{\mathbf{P}}^{(1)} + 4\pi\vec{\mathbf{P}}^{(2)} \\ &= \epsilon\vec{\mathbf{E}} + 4\pi\vec{\mathbf{P}}^{(2)}, \end{aligned} \tag{3.11}$$

such that the linear response of the material is contained in the dielectric constant ϵ. Combining the two curl Maxwell's equations results in the inhomogeneous wave equation for the harmonic field:

$$\vec{\nabla} \times \vec{\nabla} \times \vec{\mathbf{E}}_{2\omega} + \frac{1}{c^2}\frac{\partial^2\left(\epsilon_{2\omega}\vec{\mathbf{E}}_{2\omega}\right)}{\partial t^2} = -\frac{4\pi}{c^2}\frac{\partial^2\vec{\mathbf{P}}^{(2)}_{2\omega}}{\partial t^2}. \tag{3.12}$$

The right side of this equation is the nonlinear source term for second harmonic generation, and it is this equation which must be solved with the appropriate boundary conditions to determine the nonlinear properties of a material.

3.3.3 Determination of the Harmonic Fields Generated at a Surface

Bloembergen and Pershan proposed that surfaces could be treated as thin slabs of nonlinear material sandwiched between two bulk materials with only linear properties (i.e.

Figure 3.1: Nonlinear plane-parallel slab model of surface SHG.

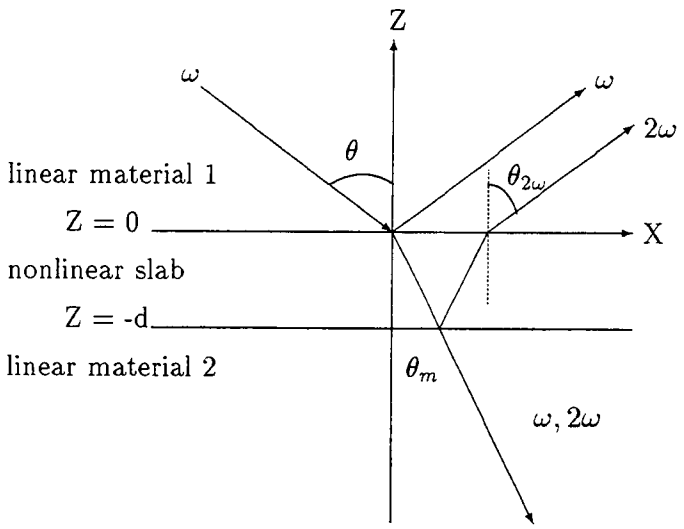

the bulk material and the surrounding environment) [63]. A diagram of this model is shown in Figure 3.1. Consider medium 1 in this figure to be the vacuum, medium 2 to be the linear bulk material, and the thin slab between $z = 0$ and $z = -d$ to be a material with both a linear and a nonlinear response allowed (the linear response of the slab is assumed to the same as the linear response of medium 2). Then light incident from the vacuum onto the slab refracts at the vacuum-slab interface. Within the nonlinear slab, the harmonic signal at 2ω begins to grow, and propagates along with the linear response at ω. When the interface between the slab and the linear medium is reached, part of the generated harmonic is reflected back into the slab, and the remaining linear and harmonic response continue into the bulk material. The portion of the harmonic which reflects back into the slab then propagates back to the slab-vacuum interface and refracts back into the vacuum. Within each material, the wave equation given in Equation 3.12 must hold, with a nonlinear source term existing only in the slab. In addition, boundary conditions are that the tangential components of both $\vec{\mathbf{E}}$ and $\vec{\mathbf{H}}$ must be continuous across $Z = 0$.

Several approximations are made to simplify the solution process. The first is the previously mentioned electric dipole approximation. It also is assumed that the incident

light is in the form of infinite plane-waves, with the additional restriction that once the plane-wave portion of the time dependence is factored out only slowly-varying amplitudes can remain. Also, the small-signal approximation is assumed, such that no depletion of the incident light occurs. With these approximations, the coupled wave equations that are given in Equation 3.12 can be solved with the appropriate boundary conditions in a straight-forward, if tedious, manipulation [63]. If the thickness d of the slab is then reduced to be much smaller than the wavelength of the incident light, the reflected and transmitted harmonic fields can be determined. The results of the above manipulation depend on the polarization of the incident light, and are as follows:

- for light polarized perpendicular to the scattering XZ plane (s-polarization), the reflected and transmitted harmonic fields are identical, and are given by

$$E_{2\omega}^{R} = E_{2\omega}^{T} = 4\pi i P_{\perp}^{(2)} \left(\frac{2\omega d}{c}\right) \frac{1}{n_{2\omega}\cos\theta_m + \cos\theta} \tag{3.13}$$

- for light polarized parallel to the scattering plane (p-polarization), the reflected and transmitted harmonic fields are given by

  1. Reflected harmonic field:

$$E_{2\omega}^{R} = -4\pi i P_{\parallel}^{(2)} \left(\frac{2\omega d}{c}\right) \frac{(\cos\theta_m \sin\alpha + \sin\theta_m \cos\alpha)}{n_{2\omega}\cos\theta + \cos\theta_m} \tag{3.14}$$

  2. Transmitted harmonic field:

$$E_{2\omega}^{T} = 4\pi i P_{\parallel}^{(2)} \left(\frac{2\omega d}{c}\right) \frac{\left(\cos\theta \sin\alpha - \frac{1}{n_{2\omega}} \sin\theta_m \cos\alpha\right)}{n_{2\omega}\cos\theta + \cos\theta_m}. \tag{3.15}$$

Here $n_{2\omega}$ is the nonlinear refractive index of the slab and α is the angle between the $-z$ axis and the nonlinear polarization vector. The s and p polarization directions can be written in terms of Cartesian coordinates by transforming in the usual way. For the nonlinear polarization, the transformation is

$$\begin{aligned} \vec{\mathbf{P}}^{(2)} &= P_{\perp}^{(2)}\hat{s} + P_{\parallel}^{(2)}\hat{p} \\ &= P_{\perp}^{(2)}\hat{y} + P_{\parallel}^{(2)}\left(\hat{x}\sin\alpha - \hat{z}\cos\alpha\right) \end{aligned} \tag{3.16}$$

while for the reflected harmonic field, the transformation is

$$\begin{aligned}\vec{\mathbf{E}}^R_{2\omega} &= E^R_{2\omega,s}\hat{s} + E^R_{2\omega,p}\hat{p} \\ &= E^R_{2\omega,s}\hat{y} + E^R_{2\omega,p}\left(\hat{z}\sin\theta - \hat{x}\cos\theta\right).\end{aligned} \tag{3.17}$$

The propagation directions for both the transmitted and reflected harmonic fields are determined by applying the constraint that tangential components of the momenta for each frequency at the boundary must be conserved. This leads to $k_{\omega,x} = k^R_{\omega,x} = k^T_{\omega,x}$ for the tangential (x) component of the fundamental field, and $2k^T_{\omega,x} = k^R_{2\omega,x} = k^T_{2\omega,x}$ for the harmonic field. The expression for the fundamental frequency leads to equal angles of incidence and reflection for the fundamental field and Snell's law for the transmitted fundamental field in the usual way. For the reflected harmonic field, geometry dictates that

$$\sin\theta_{2\omega} = \frac{k^R_{2\omega,x}}{\left|k^R_{2\omega}\right|}. \tag{3.18}$$

The right side of this can be simplified using the above equalities for the wave vectors, such that

$$\sin\theta_{2\omega} = \frac{k^R_{2\omega,x}}{\left|k^R_{2\omega}\right|} = \frac{2k_{\omega,x}}{2\left|k^R_{\omega}\right|} = \sin\theta. \tag{3.19}$$

This means that $\theta_{2\omega} = \theta$, and the reflected harmonic field travels in the same direction as the reflected fundamental. Likewise for the transmitted harmonic field, geometry and the wave-vector equalities lead to the expression

$$\sin\theta_m = \frac{k^T_{2\omega,x}}{\left|k^T_{2\omega}\right|} = \frac{2k^T_{\omega,x}}{n_{2\omega}\left|2k_{\omega}\right|} = \frac{2}{n_{2\omega}}\sin\theta, \tag{3.20}$$

which gives a modified version of Snell's law for the generated harmonic.

3.3.4 The Reflected Harmonic Intensity

Now that the reflected harmonic fields have been found (for both polarizations) as expressed in Equations 3.13 and 3.14, they can be combined to allow calculation of the second harmonic intensity from the surface. It is useful to do this by casting the fields in terms of the Fresnel transmission coefficients. Any field that is incident from vacuum into a dielectric material with refractive index n at incident angle θ (refracting at angle θ_m) will

experience an amplitude change by a factor of the Fresnel transmission coefficient. These coefficients can be written as a diagonal tensor with elements

$$\begin{aligned}\left(\tilde{L}_\omega\right)_{yy} &= \tfrac{2\cos\theta}{\cos\theta+n_\omega\cos\theta_m} \\ \left(\tilde{L}_\omega\right)_{xx} &= \tfrac{2\cos\theta_m}{n_\omega\cos\theta+\cos\theta_m} \\ \left(\tilde{L}_\omega\right)_{zz} &= \tfrac{2\cos\theta}{n_\omega(n_\omega\cos\theta+\cos\theta_m)}.\end{aligned} \tag{3.21}$$

Terms matching these coefficients can be found in the expressions for the reflected harmonic field, such that after some manipulation it becomes clear that the total reflected field for surface SHG can be expressed conveniently as a tensor contraction

$$\vec{\mathbf{E}}^R_{2\omega} = 4\pi i\left(\frac{\omega d}{c}\right)\frac{1}{\cos\theta}\left\{\tilde{L}_{2\omega}\cdot\tilde{\chi}^{(2)}(2\omega,\omega,\omega):\left[\tilde{L}_\omega\cdot\vec{\mathbf{E}}_\omega\right]\left[\tilde{L}_\omega\cdot\vec{\mathbf{E}}_\omega\right]\right\} \tag{3.22}$$

The intensity of the reflected SHG signal from the surface is then just the time average of the Poynting vector of the electromagnetic field, or

$$I_{2\omega} = \frac{c}{2\pi}\left|\vec{\mathbf{E}}_{2\omega}\right|^2. \tag{3.23}$$

This leads to the most commonly used expression for surface SHG intensity in the form

$$I_{2\omega} = \frac{32\pi^3\omega^2}{c^3}\sec^2\theta\left|\left[\hat{e}_{2\omega}\cdot\tilde{L}_{2\omega}\right]\cdot\tilde{\chi}^{(2)}(2\omega,\omega,\omega):\left[\tilde{L}_\omega\cdot\hat{e}_\omega\right]\left[\tilde{L}_\omega\cdot\hat{e}_\omega\right]\right|^2 I_\omega^2. \tag{3.24}$$

Here I_ω is the intensity of the fundamental source, and $\hat{e}_\omega$ and $\hat{e}_{2\omega}$ are the polarizations of the fundamental and harmonic fields respectively. In this expression, the slab thickness d has been absorbed into the susceptibility tensor ($\tilde{\chi}^{(2)}d \rightarrow \tilde{\chi}^{(2)}$). This is appropriate because it redefines the susceptibility as a surface susceptibility rather than a bulk susceptibility. For the bulk of the nonlinear slab, the radiation source is a volume polarization density. When the thickness of the slab is shrunk to less than a wavelength, this three dimensional volume polarization density must be replaced by its two dimensional surface counterpart. Absorbing d into $\tilde{\chi}^{(2)}$ accomplished just that. The factor of $\sec^2\theta$ dictates that the SHG intensity is a complicated function of the incidence angle, with a maximum between normal and grazing incidence. Clearly this theoretical construction is not valid at grazing incidence, where a maximum should occur due to the extremely long interaction length.

When pulsed laser sources are used, as they are in this research, it is desirable to express the output as the number of harmonic photons generated per input laser pulse.

For a Gaussian beam with pulse width T (FWHM) and spot size A (cross section to 1/e intensity), this is expressed as

$$S_{2\omega} = \frac{32\pi^3\omega}{\hbar c^3}\sec^2\theta\left|\left[\hat{e}_{2\omega}\cdot\tilde{L}_{2\omega}\right]\cdot\tilde{\chi}^{(2)}(2\omega,\omega,\omega):\left[\tilde{L}_{\omega}\cdot\hat{e}_{\omega}\right]\left[\tilde{L}_{\omega}\cdot\hat{e}_{\omega}\right]\right|^2 I_{\omega}^2 AT. \qquad (3.25)$$

All derivations here are in Gaussian units, which must be preserved and carefully treated when numerical analysis of surface SHG signals is attempted.

3.3.5 Other Phenomenological Treatments of Surface SHG

The nonlinear plane-parallel slab model is just one possible approach to treatment of surface SHG. The step where the slab thickness is decreased to less than a wavelength limits the validity of this approach. The model uses dielectric constants, which are intrinsically bulk properties. Once the slab is shrunk, its bulk dielectric constant should no longer be used. That this model produces an expression that so closely matches experiment is surprising, considering the number of approximations used in its development. Other theoretical approaches include the use of a dipole sheet of no thickness to model the surface [67]. This model yields the same result as the nonlinear slab model. Another approach uses Green's functions and a dipole sheet on the surface of a dielectric substrate [77]. The result is the same as the thin slab model, with the exception of a factor of $n_{2\omega}^2$. This factor arises because this model assigns no linear properties to the surface layer, effectively moving it outside the linear substrate. Recent efforts in this group [78] have involved using a semi-microscopic model to exactly solve for the microscopic response of the material. This approach integrates the radiation field from a continuous sheet of nonlinear dipole moments in the surface region of a linear bulk material. The result of this calculation shows the same angular dependence as the thin slab model, but is different in amplitude by a local field factor. This approach also takes into consideration the response of the linear medium to the presence of the nonlinear dipole moments, representing a more accurate description of the physical system.

3.4 Practical Considerations for Surface Analysis using SHG

3.4.1 Surface Specificity and Sensitivity Concerns

The above derivation of the SHG intensity from a surface relies on the electric dipole approximation. Generally, the bulk linear material will have a nonlinearity arising from higher multipole terms. This additional nonlinearity can be incorporated into the above analysis if the susceptibility tensor is replaced by an effective susceptibility tensor that includes the bulk quadrupole terms. Once the effective susceptibility has been determined, the reflected harmonic fields and intensity above follow without any change in form. In general, if a bulk nonlinearity is present, it can not be separated from the surface signal. In this case, it becomes necessary to establish the relative magnitudes of the two contributions to the signal. If the surface contribution dominates, or the two contributions are comparable, then surface changes can still be observed. But if the bulk multipole terms dominate, extraction of the surface signal may not be practical. In some cases, the surface signal can be extracted by carefully selecting polarization conditions for which the bulk contribution vanishes.

The electric dipole term in the polarization expansion is usually larger than the electric quadrupole and magnetic dipole terms by a factor of $\lambda/2\pi a$ where a is the size of a unit cell of the material. The bulk contribution can be assumed to come from a layer of thickness $\lambda/2\pi$ near the surface. If the allowed surface contribution comes from a slab of thickness d, then the relative surface to bulk ratio for SHG is on the order of $(d/a)^2$, assuming surface and bulk susceptibility tensors of comparable magnitude. Since d typically corresponds to a few atomic layers, this ratio is greater than or equal to unity. This dictates that the dipole SHG contribution from the surface will always be at least on the order of the multipole terms from the bulk. The surface term can be further enhanced by energy resonances (see Section 3.4.4) or through careful selection of incident polarizations (see Section 3.4.3).

Equation 3.25 allows the number of harmonic photons generated by a surface to be estimated. This number must be large enough to be detected if surface SHG studies are to be practical. For a typical surface, the surface nonlinear susceptibility is on the order of $1\text{x}10^{-16}$ esu/cm^2. This is determined by assuming that the nonlinearity arises from a

monolayer of molecules ($1x10^{14}$ molecules/cm^2) on the surface that each have a microscopic polarizability of about $1x10^{-30}$ esu [79]. For the laser used in this research, a Q-switched mode-locked Nd:YAG laser at 532 nm, there are 500 Q-switched pulse trains each second. Each pulse train consists of about 30 modelocked pulses each of 100 picosecond width. The laser spot area is about $1x10^{-3}$ cm^2, and the laser intensity is about 60 MW/cm^2. (For simplicity, the Fresnel factors are assumed to be 1.) Using these estimated values in Equation 3.25 yields a surface SHG response on the order of 10^3 photons/second. This is easily detectable.

The surface susceptibility $\tilde{\chi}^{(2)}$ is very material dependent. In general, metals have susceptibilities on the order of 10^{-14} esu/cm^2, while for dielectrics and insulators this is only 10^{-16} esu/cm^2. The factor of 100 difference in these susceptibility translates to a factor of 10000 difference in the surface SHG signal. With a signal strength of 10^3 photons/second, as calculated above for dielectrics, sub-monolayer changes in surface structure should be detectable if the detectors used are sensitive to variations of 10 photons/sec. or smaller. For a more accurate approximation, the Fresnel factors should be taken into account.

3.4.2 Detection of Adsorbed Layers on Surfaces

When the surface is complicated through the addition of adsorbates, the surface nonlinear susceptibility will consist of three parts: the bare surface susceptibility $\tilde{\chi}^{(2)}_{bs}$, the susceptibility of the adsorbate layer $\tilde{\chi}^{(2)}_{a}$, and an additional susceptibility $\tilde{\chi}^{(2)}_{I}$ to account for interactions between the surface and the adsorbate layer. Then the effective surface susceptibility is just $\tilde{\chi}^{(2)}_{eff} = \tilde{\chi}^{(2)}_{bs} + \tilde{\chi}^{(2)}_{a} + \tilde{\chi}^{(2)}_{I}$. The relative contribution from each component of this susceptibility depends on the material and adsorbate involved. The adsorbate term may dominate if the adsorbed molecules are highly asymmetric and if the interaction term is small. If a highly symmetric molecule is adsorbed, then the primary contribution to the susceptibility may be the interaction term. In either case, surface SHG studies would be sensitive to the presence of the adsorbed molecular layer. If a change in the density of adsorbed molecules occurs, this will be accompanied by a corresponding change in the surface SHG signal. The signal can be either proportional to the adsorbate density or to

this density squared, depending on whether the signal comes from the interaction term or the adsorbate susceptibility term. Thus surface SHG can be used to monitor adsorption and desorption from surfaces.

3.4.3 Determination of Surface Structure using SHG

Susceptibility tensors are subject to various levels of symmetry restriction such as permutation symmetry, time-reversal symmetry and spatial symmetry. Permutation and time-reversal symmetries are inherent properties of susceptibilities that arise from principles of time invariance and causality, while the spatial symmetry of a tensor is dictated by the structural properties of the nonlinear medium. These symmetry constraints may cause some elements of the susceptibility tensor to vanish entirely and some remaining elements to be related to each other. The space group that a crystal structure belongs to dictates the pattern that the tensor elements follow. Measurement of these tensor elements can thus lead to descriptions of the physical structure of a crystal.

The second-order electric susceptibility tensor has 27 elements. These elements are labeled χ_{ijk}, with the subscripts referring to each of the three cartesian directions. Convention varies concerning the order of these indices. Here the first index refers to the direction of a component of the output field at 2ω, while the second and third indices are directions for components of the incident field at ω. Degeneracy of the input photons reduces the number of independent elements of the susceptibility tensor to 18, since $\chi_{ijk} = \chi_{ikj}$ is required. If the surface to be studied has a certain symmetry, the number of non-zero tensor elements can be greatly reduced. The higher the symmetry of a surface, the fewer non-zero tensor elements it will have. Table 3.1 lists the non-zero tensor elements for a few surface geometries. Whether an element is non-zero is determined by applying symmetry operators to the system's coordinates. Tensor elements should be invariant when the appropriate symmetry operations are applied to the coordinates. If a symmetry operation on the coordinates produces a sign change in that element, then it is necessary that the tensor element vanish to satisfy $\chi_{ijk} = -\chi_{ijk}$.

TiO_2 surfaces belong to the C_{2v} point group. This group has a 2-fold rotation axis (z) and two mirror planes (xz and yz). The rotation operator $C_2(z)$ requires that the transformation $(x,y,z)\rightarrow(-x,-y,z)$ leaves tensor elements unchanged. Likewise the mirror operators σ_{xz} and σ_{yz} required symmetry under the transformations $(x,y,z)\rightarrow(x,-y,z)$ and $(x,y,z)\rightarrow(-x,y,z)$, respectively. Under $C_2(z)$, all tensor elements are eliminated except χ_{zzz} and any combination that has one index $= z$ and the other two either $= x$ or $= y$. Under the mirror operators, elements with only one index that is x or y vanish. What is left are χ_{zzz} and the six possible elements for which one index is $= z$ and the other two are either both $= x$ or both $= y$ (see Table 3.1). Photon degeneracy further restricts these elements so that $\chi_{xxz}=\chi_{xzx}$ and $\chi_{yyz}=\chi_{yzy}$. Non-zero elements for the other listed symmetry groups can be obtained in the same way.

The tensor form of $\tilde{\chi}^{(2)}$ results in a certain pattern in the SHG intensity as a function of the input and output polarization directions. By selecting particular input and output polarizations, specific non-zero elements of $\tilde{\chi}^{(2)}$ can be extracted so that only they contribute to the measured SHG intensity. On the surface with C_{2v} symmetry, for example, if light is incident with a component of polarization in the y-direction, only χ_{zyy} will contribute to the SHG intensity. Thus the light from the surface will be polarized in the z-direction, and measuring its intensity allows one element of the susceptibility tensor to be numerically determined. Careful choice of other polarization conditions allows extraction of the other elements. In this way, variations from the expected polarization behavior can be used to determine how close a real surface is to its ideal structure. Similarly, changes in the intensity pattern over time can be used to monitor changes in surface structure.

3.4.4 Surface Spectroscopy Using SHG

So far the electric susceptibility tensor $\tilde{\chi}^{(2)}$ has been treated as a macroscopic response function that reflects the symmetry properties of a material. Connection with the material on the molecular scale must be made so that these response functions can be determined theoretically. For a molecular solid, $\tilde{\chi}^{(2)}$ is just an ensemble average of the second-order microscopic molecular polarizability tensor $\tilde{\beta}^{(2)}$. Every macroscopic response function can

Table 3.1: Non-zero tensor elements for surfaces with various symmetries. Here the index convention $\chi_{out,in,in}$ is used. The number in parenthesis is the number of nonvanishing elements, while the number is brackets is the number of independent elements. Tensor elements extracted under certain polarization conditions are also listed, with the convention $I_{out,in}$. Here the sample is in the xy plane, and xz is taken to be the scattering plane. Thus $\hat{s}$ is $\hat{y}$, and $\hat{p}$ has components in both $\hat{x}$ and $\hat{z}$.

Symmetry Class	Nonvanishing Tensor Elements	Elements Sampled by Simple Polarization Experiments
C_{1v} (yz mirror plane)	(14)-[10] a=zzz, b=zxx, c=zyy, d=xxz=xzx, e=yyz=yzy, f=zzy=zyz,g=xxy=xyx, h=yyy, i=yxx, j=yzz	$I_{ss} \rightarrow$ h $I_{ps} \rightarrow$ c $I_{sp} \rightarrow$ e, i, j $I_{pp} \rightarrow$ a, b, d, f, g
C_2 (no mirror plane)	(13)-[8] a=zzz, b=zxx, c=zyy, d=xxz=xzx, e=yyz=yzy, f=zxy=zyx,g=yxz=yzx, h=xyz=xzy	$I_{ss} \rightarrow 0$ $I_{ps} \rightarrow$ c $I_{sp} \rightarrow$ e, g $I_{pp} \rightarrow$ a, b, d, f, h
C_{2v} (yz and xz mirror planes)	(7)-[5] a=zzz, b=zxx, c=zyy, d=xxz=xzx, e=yyz=yzy,	$I_{ss} \rightarrow 0$ $I_{ps} \rightarrow$ c $I_{sp} \rightarrow 0$ $I_{pp} \rightarrow$ a, b, d
C_3 (no mirror plane)	(19)-[6] a=zzz, b=zxx=zyy, c=xxz=xzx=yyz=yzy, d=yyy=-yxx=-xxy=-xyx, e=xxx=-xyy=-yxy f=xyz=xzy=-yxz=-yzx	$I_{ss} \rightarrow$ d $I_{ps} \rightarrow$ b, e $I_{sp} \rightarrow$ d. f $I_{pp} \rightarrow$ a, b, c, e
C_{3v} (yz mirror plane)	(11)-[4] a=zzz, b=zxx=zyy, c=xxz=xzx=yyz=yzy, d=yyy=-yxx=-xxy=-xyx	$I_{ss} \rightarrow$ d $I_{ps} \rightarrow$ b $I_{sp} \rightarrow$ d $I_{pp} \rightarrow$ a, b, c
C_4 or C_6 (no mirror plane)	(11)-[4] a=zzz, b=zxx=zyy, c=xxz=xzx=yyz=yzy, d=xyz=xzy=-yxz=-yzx	$I_{ss} \rightarrow 0$ $I_{ps} \rightarrow$ b $I_{sp} \rightarrow$ d $I_{pp} \rightarrow$ a, b, c
C_{4v} or C_{6v} (xz and yz mirror planes)	(7)-[3] a=zzz, b=zxx=zyy, c=xxz=xzx=yyz=yzy,	$I_{ss} \rightarrow 0$ $I_{ps} \rightarrow$ b $I_{sp} \rightarrow 0$ $I_{pp} \rightarrow$ a, b, c

be related in this way to a microscopic counterpart (for the linear response, $\tilde{\chi}^{(1)}$, the microscopic counterpart is just α, the molecular polarizability). From the microscopic standpoint, these polarizabilities can be calculated by fully quantizing both the material system and the radiation field. Then second harmonic generation can be interpreted as a three-photon process in which two photons from the fundamental field are annihilated while a photon at the harmonic frequency is created. Then the polarizability can be calculated using third-order perturbation theory to be

$$\beta_{abc}(2\omega;\omega,\omega) = \sum_{j,k}\left[\frac{\langle i|a|k\rangle\langle k|b|j\rangle\langle j|c|i\rangle}{(E_k - 2\hbar\omega - i\Gamma_k)(E_j - \hbar\omega - i\Gamma_j)}\right. \tag{3.26}$$
$$\left. + \frac{\langle i|c|k\rangle\langle k|a|j\rangle\langle j|b|i\rangle}{(E_k+\hbar\omega-i\Gamma_k)(E_j-\hbar\omega-i\Gamma_j)} + \frac{\langle i|c|k\rangle\langle k|b|j\rangle\langle j|a|i\rangle}{(E_k+\hbar\omega-i\Gamma_k)(E_j+2\hbar\omega-i\Gamma_j)}\right].$$

Here $|i\rangle$ is the ground state of the material system, while $|j\rangle$ and $|k\rangle$ are intermediate states. The energy level of each state is E, and Γ is the phenomenological damping term. The operators a, b, and c are the electric dipole operators x, y, or z. The summations are carried out over complete sets of states. If a photon energy is close to a real energy level in the system, the energy denominators dictate that the molecular susceptibility is greatly enhanced. Such enhancements are called *resonances*, and can be used to determine the location of the electronic states of a material.

Since the dipole operators are odd with respect to inversion, non-zero transition moments only occur for transitions that go from an even state to an odd state, or vice versa. If a molecule has a center of symmetry, its wavefunctions are either odd or even functions in space. It is not possible to connect such a ground state back to itself through three odd transitions. That is, for the transition $|i\rangle \rightarrow |j\rangle \rightarrow |k\rangle \rightarrow |i\rangle$, the dipole operators dictate that the transition follow even→odd→even→odd or odd→even→odd→even. Since this is not possible for ground states that are entirely odd or even (not a combination of the two), the transition is forbidden. This is the microscopic argument that dictates that second harmonic generation is forbidden in centrosymmetric materials. Again at a surface, symmetry is broken along the surface normal, and these transitions are allowed.

The three terms in Equation 3.26 can be expressed as three time-ordered quantum mechanical diagrams, as shown in Figure 3.2. The diagrams correspond to the terms in the order they appear in the molecular polarizability equation. In the first time-ordering,

Figure 3.2: Time-ordered diagrams for second harmonic generation, showing possible resonances.

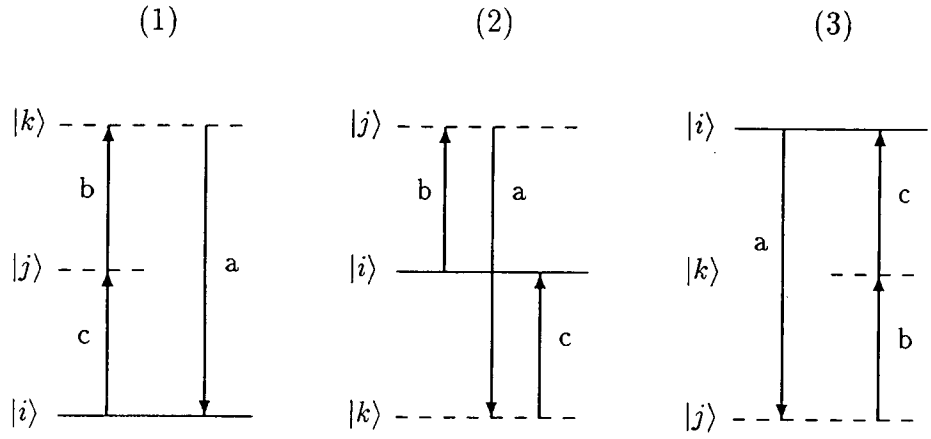

two resonances are possible if real electronic states appear at energies $\hbar\omega$ or $2\hbar\omega$. In the second diagram, only one resonance is possible, while no resonances are possible in the third diagram. All three of these terms contribute to the nonlinear response of the material. Matching photon frequencies to real electronic levels above the ground state enhances the first two processes, but not the third, such that the third is negligible when compared to the others. Signal enhancement on resonance makes it possible for SHG to be used as a spectroscopic tool for surfaces and adsorbed molecular layers. If the laser frequency can be tuned, scanning through a range of frequencies will locate resonances and allow determination of the surface electronic states. For a fixed laser frequency, changes in the surface electronic structure during molecular adsorption or desorption will appear as changes in the SHG signal, allowing SHG to be used as a probe of surface dynamics.

3.5 X-ray Photoelectron Spectroscopy

Since its development in the years between 1955 and 1970, X-ray Photoelectron Spectroscopy (XPS) has become one of the most widely used and broadly applicable surface science techniques available [58]. Typically XPS is used to determine the chemical composition of material surfaces, though depth-profiling studies can be done in some circumstances

to examine the chemical makeup of bulk materials. XPS is better known as Electron Spectroscopy for Chemical Analysis (ESCA). This is perhaps a more precise description of the technique because the electron spectrum obtained by irradiating a sample with X-rays contains not only electrons produced through the photoelectric effect, but also secondary Auger electrons. In recent years, spectrometers have been developed that have sufficient resolution to detect differences in the valence state of atoms on the surface. This makes it possible to employ XPS as a tool to study defects on surfaces, even when those defects occur in densities that are fractions of a monolayer. Lineshapes for high-resolution spectra are remarkably reproducible, such that minute changes in these lines can be interpreted as real physical changes in the surface. The following sections describe the basic theory behind this technique.

3.5.1 XPS Spectra of Elements

3.5.1.1 X-ray Generation of Photoelectrons

In XPS, monochromatic soft X-rays from either a Mg ($h\nu = 1253.6eV$) or Al ($h\nu = 1486.6eV$) source are used to irradiate the surface of the material to be characterized in UHV. These X-rays ionize atoms in the material, resulting in the ejection of electrons with kinetic energies given by $KE = h\nu - BE$, where $h\nu$ is the energy of the X-ray and BE is the binding energy of the orbital from which the electron originates. A schematic diagram of this process appears in Figure 3.3. If this electron comes from an atom on the surface of the material, and if it has enough kinetic energy to overcome the work function (ϕ) of the surface, the electron can leave the material entirely. Such electrons can then be detected and sorted by their kinetic energy, which is now given by

$$KE = h\nu - BE - \phi. \tag{3.27}$$

Since the photon energy is known and the work function can be measured, this kinetic energy spectrum consists only of sharp peaks occurring at kinetic energies that correspond to the electron's binding energy to its parent atom. Every element has a unique set of electron orbitals, and thus a unique set of discrete electron binding energies. Thus the

Figure 3.3: The photoelectric effect gives rise to photoelectrons observed in XPS spectra

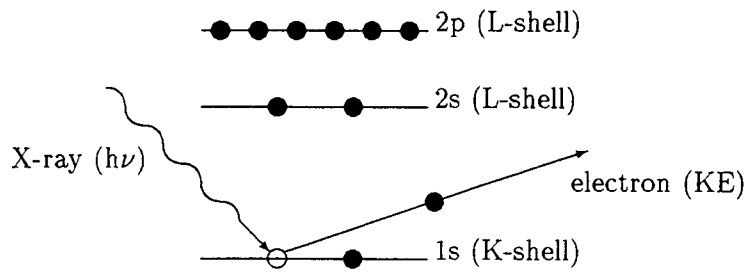

location of the peaks in the electron kinetic energy distribution from an irradiated sample can be used to identify the elements that comprise the sample. In addition, the cross section for ejection of an electron in a particular orbital varies from orbital to orbital, and from element to element, such that the ratios of the various peak heights in the spectrum of an element are also uniquely characteristic of that element.

The above description only includes "elastic" photoemission events where the emitted electron undergoes no energy change between its ejection by its parent atom and its detection (except for the energy loss due to the surface work function, which has already been included). This is appropriate for electrons right at the surface of the material, but electrons in the layers below typically collide with atoms in the upper layers before escaping the material. Electrons lose energy in these collisions, such that they are not detected in the main photopeak. Instead, they contribute to a "tail" to lower kinetic energy (higher binding energy) on the photopeak. This is referred to as "inelastic" photoemission, and is responsible for most of the "background" signal seen in an XPS spectrum. (An additional small background of detected electrons is seen due to Bremsstrahlung radiation.) X-rays from a typical source penetrate a solid to a depth on the order of 10 microns. But electrons in a solid have a mean free path on the order of ten of Angstroms, such that only electrons which are ejected very near the surface will escape the material without energy loss to appear in a photopeak. This guarantees that the photopeaks in XPS spectra are surface specific, originating within the top few atomic layers.

Table 3.2: Area ratios for spin-orbit doublets

Subshell	j values	Area ratio
s	$\frac{1}{2}$	no doublet
p	$\frac{1}{2}, \frac{3}{2}$	1:2
d	$\frac{3}{2}, \frac{5}{2}$	2:3
f	$\frac{5}{2}, \frac{7}{2}$	3:4

Electrons bound more tightly than the X-ray photon energy clearly can not be removed from their parent atom by the X-rays, and thus are not seen in the photoelectron spectrum. But all other electron orbitals (quantum numbers nl) will have corresponding photopeaks. Except for s-orbitals ($l = 0$), all orbitals are doublets as a consequence of spin-orbit coupling. Here there are two possible states, characterized by the quantum number $j(\vec{\mathbf{J}} = \vec{\mathbf{L}} + \vec{\mathbf{S}})$ that arise when $l > 0$. (For example p-orbitals ($l = 1$) are doublets with $j = \frac{1}{2}, \frac{3}{2}$, while d-orbitals are doublets with $j = \frac{3}{2}, \frac{5}{2}$, and so on.) The relative intensities of these doublet peaks are given by the ratio of their respective degeneracies $(2j + 1)$. Table 3.2 lists the j values and area ratios of several orbital subshells. The energy splitting ΔE_j of each doublet is proportional to the spin-orbit coupling constant ξ_{nl}, which in turn depends on the expectation value $\langle 1/r^3 \rangle$ for the orbital in question. Thus the quantum numbers of observed photopeaks can be determined by measuring the ratio of the doublet heights (yields l) and the separation of the doublet peaks (yields n). Additionally, the doublet splitting is expected to increase in size as atomic Z increases for a given subshell (constant n, l). For this reason, doublets for many low-Z elements can not be resolved.

Thus the XPS spectrum for an element contains photopeaks corresponding to all electron orbitals with energy less than the X-ray photon energy. The location and relative heights of these peaks provide a "fingerprint" that allows unique identification of the element. But spectra will also contain peaks corresponding to Auger electrons emitted in the wake of photoelectric events.

Figure 3.4: Electrons from higher levels fill the vacancy left by X-ray photoemission, resulting in the ejection of Auger electrons

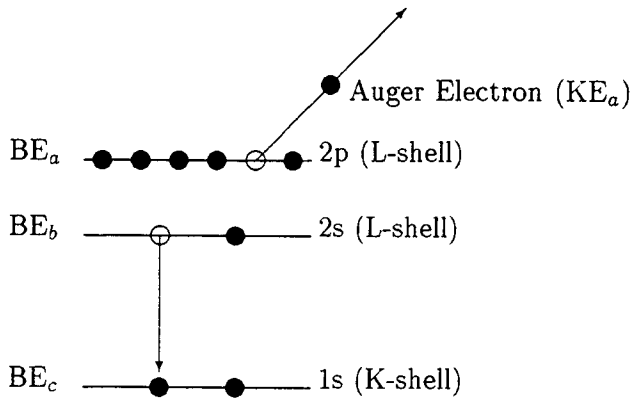

3.5.1.2 Generation of Auger Electrons

When a soft X-ray ejects an electron, the hole left behind will be filled as an electron makes a transition down from a higher shell. As this occurs, the energy released in the transition can eject still another electron, called an Auger electron. If this Auger electron can overcome the work function of the surface, it will be collected along with the direct photoelectrons in XPS. The result is a superimposed Auger spectrum on every XPS spectrum. The location and relative size of these Auger peaks are also unique to each element, and can be used to help identify a material. Inelastic Auger electrons will also be detected in a tail to lower kinetic energy of the Auger peak, in direct analogy to the inelastic photoelectrons previously discussed.

A schematic picture of Auger electron ejection appears in Figure 3.4. Here an electron from level b falls to fill the vacancy in level c. Conserving energy for this transition gives the amount of energy $\Delta E = BE_c - BE_b$ released in this transition. Because electron binding energies are negative, ΔE is a negative number. If this liberated energy is then used to eject an electron from level a, conservation of energy dictates that this Auger electron have kinetic energy given by

$$KE_a = BE_a + BE_b - BE_c. \tag{3.28}$$

A typical XPS spectrum may have several groups of Auger peaks, each corresponding to a different combination of the three levels needed for a complete Auger electron emission. These groups are identified by specifying the shells of the initial core vacancy and the two final vacancies. In most Auger processes observed in XPS spectra, the two final vacancies occur in the same subshell (same n), and the difference in principle quantum number between the initial and final vacancy levels is one. For example, the KLL Auger group includes all Auger peaks that arise when a K-level ($n = 1$) vacancy is filled by an L-shell ($n = 2$) electron, with the ejection of an L-shell Auger electron as a consequence. Other groups observed are LMM, MNN, and NOO. The KLL group consists of nine possible lines (all combinations of L-shell electrons) and the other groups have still more [58, See Section 3.2]. It is also possible for the initial vacancy to be filled by electrons in the valence (V) band of a material, with these transitions giving rise to KVV peaks.

3.5.1.3 Examples: Elemental Spectra for Titanium and Oxygen

Figures 3.5 and 3.6 show typical XPS spectra for titanium and oxygen respectively using Mg-K_α X-rays [80]. The energy axis for both plots is the calculated *binding* energy of the electron detected (from Equation 3.27). Electrons on the left of the graph have the smallest kinetic energy (254 eV), while electrons to the far right have the largest (1254 eV). Here the photopeaks are the narrower features, labeled by their quantum numbers, while the Auger peaks are broad (containing multiple unresolved peaks). The inelastic tail of each feature is visible as the background jump to its left. Linewidths for the photopeaks are limited by the linewidth of the incident X-rays and the ultimate energy resolution of the electron detector.

In the titanium spectrum, which comes from a nearly-pure titanium metal sample, the 2s (565 eV), 2p (doublet 464 and 458 eV), 3s (62 eV), and 3p (unresolved doublet at 37 eV) photopeaks appear. The 1s level is too tightly bound to be removed by these X-rays, so it does not appear in the spectrum. The 2p doublet with an energy splitting of about 6 eV is clearly resolved in this spectrum, while the 3p doublet with a smaller energy splitting is not. The electronic configuration of Ti is $1s^2 2s^2 2p^6 3s^2 3p^6 4s^2 3d^2$, indicating that

Figure 3.5: XPS spectrum of Ti metal

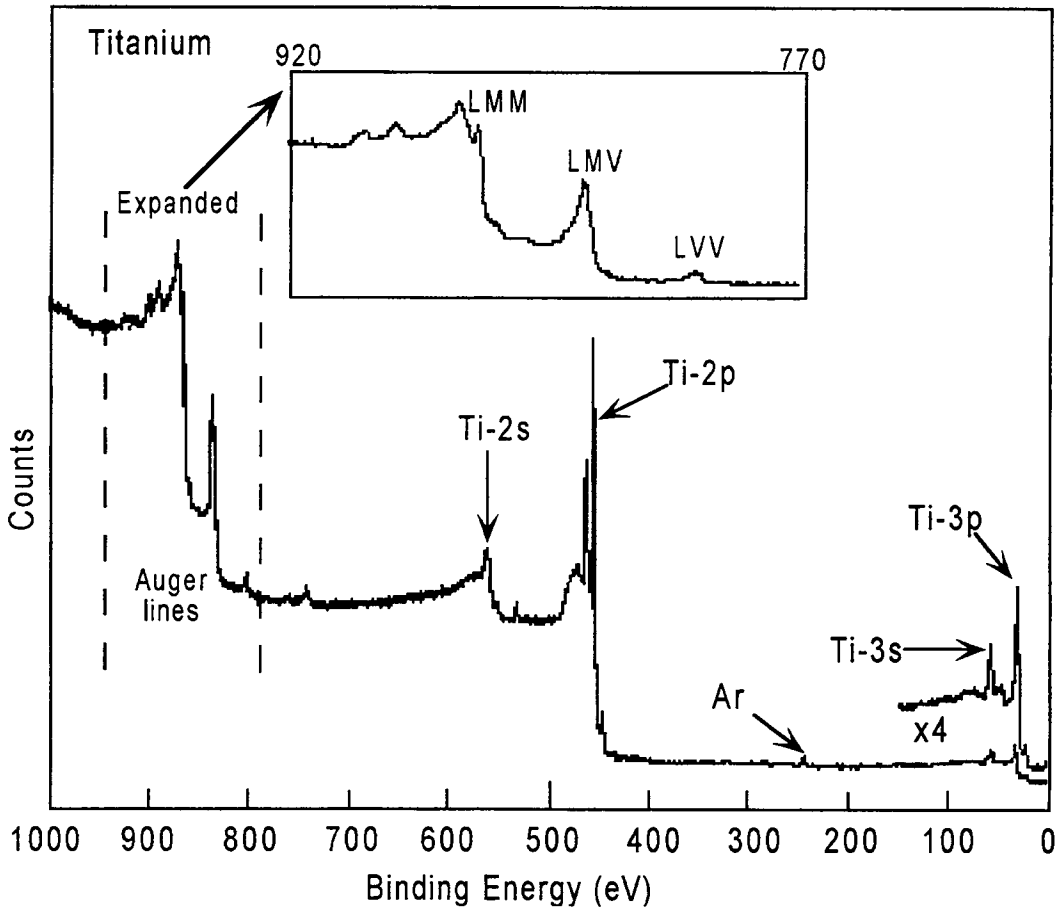

we should also expect to see 4s and 3d peaks. These peaks do occur in the spectrum (to the right of the 3p peak shown), but the cross section for their ejection by X-rays is very small, leading to very small peaks that are difficult to resolve. (Typically, the cross section for photoemission is much larger for electrons nearer the core of the atom, meaning that XPS is not a good tool for studying outer-level electrons or valence electrons in a material. Spectrometer resolution also decreases slightly for electrons with very high kinetic energies, leading to broadening in the peaks with binding energies below about 50 eV.) Auger peaks for Ti appear between binding energies of 910 eV and 700 eV and are predominantly LMM transitions. Small LMV and LVV peaks appear as well. The inset in this figure shows these peaks on an expanded scale with slightly better resolution. But even at this resolution the

Figure 3.6: XPS spectrum of Oxygen in Al_2O_3

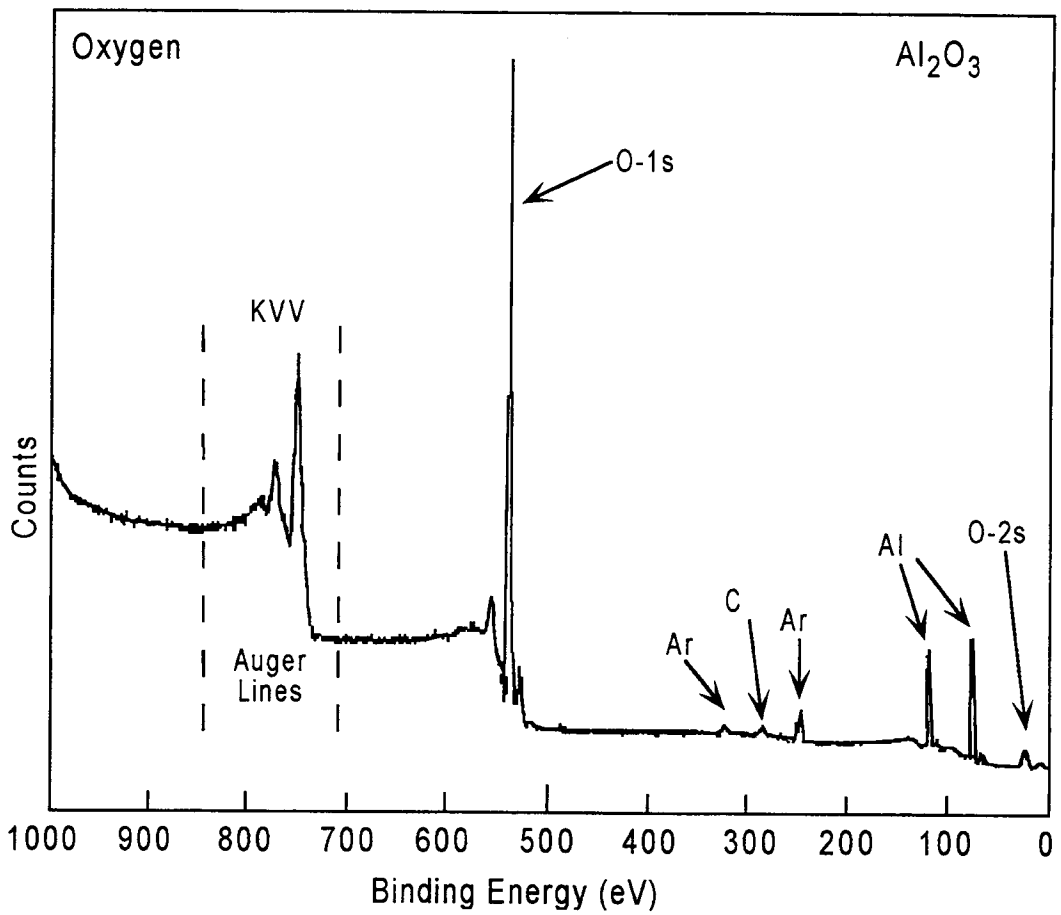

distinct peaks in the Auger groups can not be distinguished. Small contamination peaks from oxygen (1s at 531 eV and Auger around 750 eV) and argon (2p at 241 eV) also appear in this spectrum. Oxygen contamination is an indication of the difficulty faced in obtaining pure metal surfaces for metals that preferentially form an oxide layer. Argon ion sputtering is used to remove this oxide layer in UHV, resulting in very small oxygen contamination with an accompanying implantation of a small number of argon atoms.

The oxygen ($1s^2 2s^2 2p^4$) spectrum shown in Figure 3.6 was generated using Mg-K_α X-rays on an Al_2O_3 surface. Since pure oxygen is a molecular gas, standard spectra for oxygen are taken from oxygen-containing solid compounds. (Spectra for gases can be taken, but this requires a different experimental XPS geometry. It is desirable to take all standard

spectra on the same system, so a suitable solid standard is chosen.) Here the 1s (531 eV) and 2s (23 eV) photopeaks are large enough to be discerned; the 2p peak is visible, but small and broad. The Auger group seen between 800 and 700 eV in binding energy is a consequence of Auger transitions to core K-levels from the valence band, which is in this case the oxygen L-shell. Peaks from the aluminum in the sample are seen in the spectrum, as expected.

The slight carbon contamination (285 eV) is indicative of *adventitious* carbon. This is carbon from hydrocarbons endemic on surfaces due to handling in preparation. It is typically sputtered off using argon ions, which explains why this small remaining carbon signal is accompanied by small amounts of argon implanted during the sputtering process. (A discussion of the use of argon sputtering to clean surfaces during sample preparation can be found in Section 4.3.6.3.) But trace amounts of adventitious carbon can sometimes be useful, particularly on insulating samples that experience *charging* during XPS data collection. Charging occurs because the work function of the surface changes slightly as electrons leave the surface of an insulator. This shifts all peaks in the XPS spectrum from their true values by an equal amount. This shift can be corrected for, and the photopeaks returned to their true positions, if a material such as adventitious carbon that has a known true peak location is present in quantities large enough to be detected but small enough not to interfere with experiments. Further discussion of charging can be found in Section 5.2.2.2.

3.5.2 XPS Spectra of Compounds

Using Al_2O_3 above to obtain a standard spectrum for oxygen raises questions concerning how spectra for pure elemental materials, such as metals, will compare to spectra for compounds containing those elements, such as metal oxides. Will the spectrum for a compound just be a superposition of the spectra of the individual elements of that compound? Can the relative peak heights for the elements seen in a compound spectrum be used to determine the chemical structure of the compounds? Do peaks for an element vary

in location or shape for different compounds containing that element? The following discussion addresses these questions, and discusses what chemical information can be obtained from spectra of compounds.

3.5.2.1 An Example: TiO_2

The gross features of elemental spectra are in general preserved when that element is part of a compound. The spectrum for the compound is then roughly a superposition of the spectra for its constituent elements. The photopeaks and Auger lines for each element appear at about the same energies, and with the same peak height ratios. It is thus possible to identify each element in the compound as long as characteristic peaks for one element do not overlap peaks for other elements too drastically. Comparing peaks heights element-to-element allows the compound stoichiometry to be determined. Figure 3.7 shows an XPS spectrum for a surface of stoichiometric rutile $TiO_2(110)$. The previously seen Ti-2s (565 eV), Ti-2p (doublet 464 and 458 eV), Ti-3s (62 eV), and Ti-3p (37 eV) photopeaks are easily identified, as are the Auger peaks between 910 and 700 eV. But now O-1s (531 eV), O-2s (23 eV), and O-Auger (between 800 and 700 eV) peaks are also present, superimposed on the titanium spectrum. A small amount of adventitious carbon (287 eV) is also visible.

3.5.2.2 Determination of Surface Stoichiometry Using XPS Spectra

The compound spectrum shown above not only allows the elements present on the surface to be identified, but also allows surface stoichiometry to be determined. In stoichiometric TiO_2 a 2:1 oxygen to titanium ratio is expected. But the observed O-1s and Ti-2p peaks in the compound spectrum are about the same size. This is because the cross section for photoemission varies for each element, such that these peak heights can not be compared until the "sensitivity" of the spectrometer to each element is determined. XPS handbooks list empirically derived sensitivity factors for standard spectrometers [58, See Appendix 6], but it is necessary for these to be confirmed for each spectrometer if accurate atomic ratios are to be guaranteed. The sensitivity factor scale is set such that the fluorine

Figure 3.7: XPS spectrum of rutile TiO_2

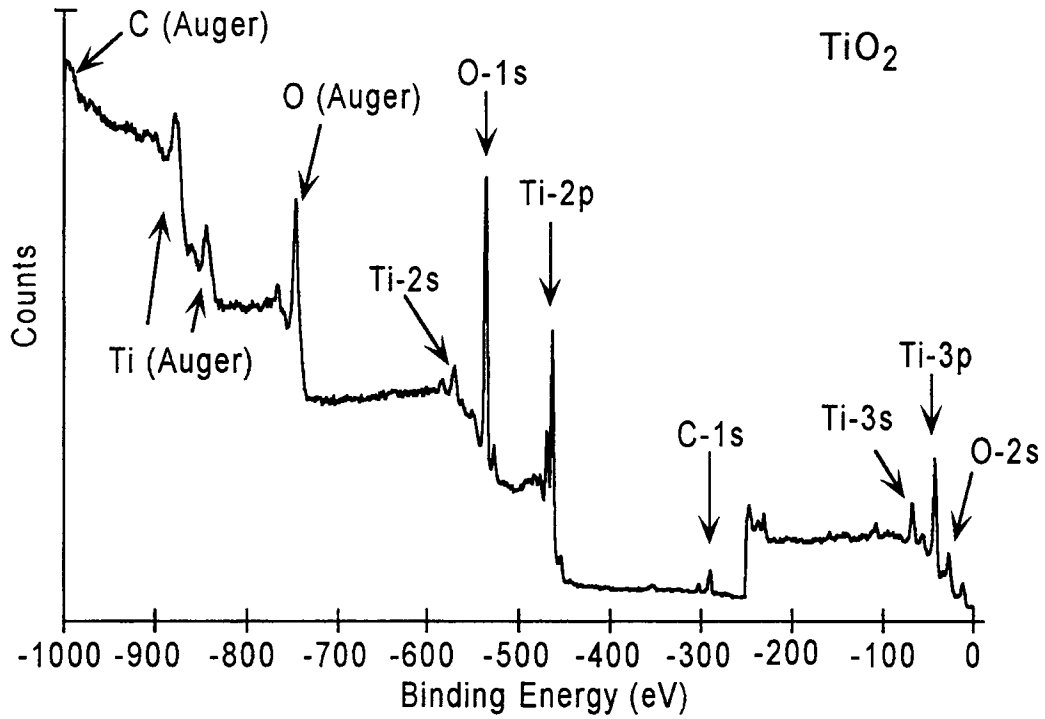

1s line is defined to have a sensitivity factor of one. Each photopeak for a given element will have a different sensitivity factor reflecting the relative peak heights for that element. Likewise for a given orbital, each element can be expected to have a different sensitivity factor. Peaks for processes with a smaller cross sections have smaller sensitivity factors, so that determination of the stoichiometry of a compound is achieved by *dividing* the peak height for each element in the compound by its appropriate sensitivity factor to compensate. For example, the sensitivity factor for oxygen 1s electrons is small (0.66), and is about half that of titanium 2p electrons (1.2). This easily explains why a stoichiometric TiO_2 sample produces O-1s and Ti-2p peaks that are roughly the same size. Dividing these peak heights by the appropriate sensitivity factors gives "corrected" peak heights with correct stoichiometry. Compounds containing many elements can be analyzed in a similar fashion, allowing the stoichiometry, or the percent of each element present in the compound, to be determined. Usually such determinations of atomic percent for the elements in a compound

are considered valid only to about 5%. This can be improved by carefully determining the sensitivity factors for each spectrometer rather than using the empirically derived values.

3.5.2.3 Determination of surface chemical state using XPS spectra

The above discussion implies that few variations occur between the spectrum for an element and the spectrum for that element in a compound. While this is true for the gross structure of the photopeaks, there are fine changes in peak location and shape that reflect the changes in electronic structure that occur when an element becomes part of a compound. These variations are not resolvable on the energy scale used for identification of peaks, but can be seen easily using high resolution scans over just a few electron-volts of energy. These variations are relatively small, but they are also remarkably reproducible, allowing them to be used to determine the chemical state of the element. In many cases defects in the structure can also be detected as small changes in high resolution spectra. The following section gives examples of this and shows how defects are observed on the TiO_2 surfaces examined here.

High resolution scans of the Ti-2p doublet over 20 eV for both elemental Ti and the Ti found in rutile TiO_2 are shown in Figure 3.8. Comparison of these spectra shows that the Ti-$2p_{3/2}$ photopeak for the compound is shifted 4.7 eV to higher binding energy as compared to the elemental peak. In addition, the doublet for the compound is separated by 5.7 eV, while the doublet for the element is spaced by 6.15 eV. Clearly titanium atoms bound in a crystal oxide can be expected to have a different electronic structure than those found in a metal. This difference shows up in these variations in peak location and separation as seen by XPS. Peaks in the oxide also have a different shape than peaks in the metal, with the oxide peaks being nearly symmetric. Narrow, symmetric Ti-2p peaks at these energies are signature characteristics of titanium atoms in TiO_2 that are fully coordinated to surrounding oxygen atoms. Such Ti atoms are in a 4+ valence state. If an oxygen vacancy is produced on the surface, the coordination of the Ti atom that remains behind is reduced and the Ti atom will be in a 3+ valence state. A shift of 1.7 eV in the location of the Ti-2p peaks accompanies this change. If a substantial number of these defects are created,

Figure 3.8: High resolution XPS spectra of Titanium in Ti metal and TiO_2

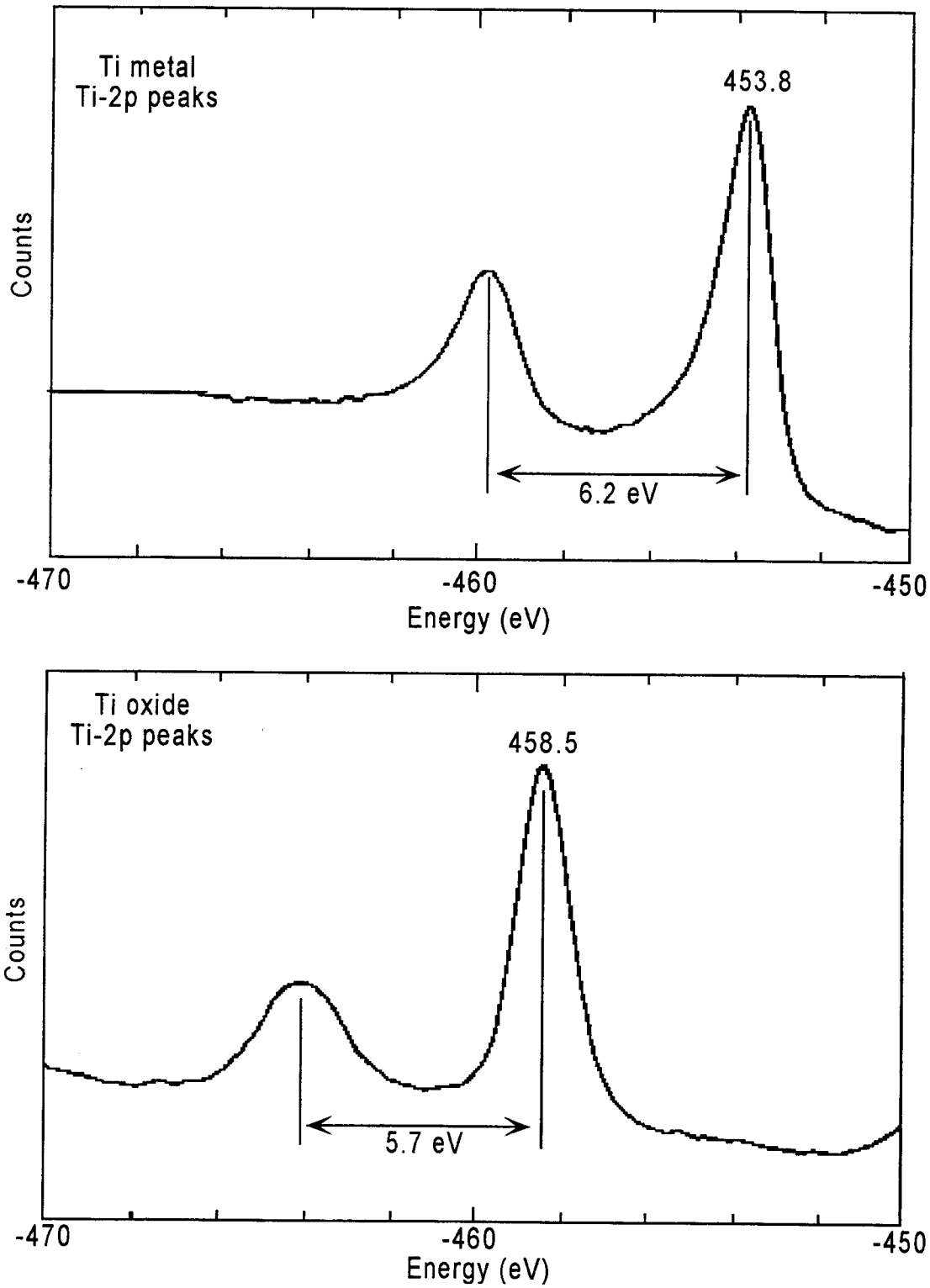

Ti atoms at the new Ti^{3+} peak-energy contribute to a "shoulder" that appears on the low binding energy side of the peaks for the remaining Ti^{4+} atoms. If the coordination number of the Ti atoms is reduced further by removing more oxygen atoms, peaks associated with Ti^{2+}, Ti^{1+} and Ti^{0+} will grow in as well. The Ti^{0+} state, which is metallic in nature, will have peaks located at the elemental peak-energies. Curve-fitting spectra for a damaged surface results in an estimate of the defect density for each type of valence state present. Examples of spectra with defect shoulders are presented in Chapter 5.

3.5.3 Summary

This discussion shows how XPS spectra can be used to determine the elemental composition, stoichiometry, chemical state, and even defect concentration of surfaces. For experiments in this thesis, scans over a broad energy range are frequently taken to ensure that no contamination is present on TiO_2 surfaces. But the spectra presented and discussed in detail here will be "multiplex" scans over small energy windows that are expected to contain peaks of interest. The resulting peaks will be overlapped for different surface treatments, and any changes in peak lineshapes will be interpreted as arising from physical changes on the surface.

3.6 Ultraviolet Photoelectron Spectroscopy

Ultraviolet photoelectron spectroscopy (UPS) is in many ways similar to XPS. Incident photons eject electrons from the surface, and these electrons are collected and sorted by energy. But for UPS, ultraviolet rather than X-ray photons are used. UV photons are considerably less energetic (21.2 eV for UPS -vs.- 1254 eV for XPS), and only eject electrons from the valence band of the surface. Thus UPS is used to measure band structure for the surface, rather than electronic structure of individual atoms, as XPS measures. Changes in this band structure are complex, making interpretation of changes in UPS spectra somewhat subjective. The ambiguities that result from this will be extensively discussed as UPS experiments are presented. UPS spectra for TiO_2 surfaces show that the surface valence

band ends about 3.1 eV below the conduction band edge, consistent with the bulk band-gap. When defects are present, a state appears in this gap that corresponds to population of empty Ti-3d orbitals. This state is used as a defect "signature" for studies of defect-molecule interactions. Additional features in UPS spectra for TiO_2 will be discussed as spectra are presented beginning in Section 5.2.3. Here UPS will not be emphasized because experiments presented here will show that it can provide ambiguous results that depend heavily on methods used to overlap spectra.

CHAPTER 4
EXPERIMENTAL DETAILS

4.1 Overview

This thesis compares experimental results from several different surface science techniques. All nonlinear optical experiments were done at Oregon State University, while all experiments using other surface science techniques (XPS and UPS) were done during my six months of on-site collaboration at Pacific Northwest Laboratory (a national laboratory in Richland, WA. operated by the Battelle Memorial Institute). In this section, I will separately describe the experimental details of each system used for these experiments. Efforts were made to duplicate experimental conditions exactly in different systems. In some cases, this was simply not possible. Any differences between procedures at OSU and PNL are noted and discussed.

4.2 Second Harmonic Generation

All Second Harmonic Generation experiments presented here for $TiO_2(110)$ surfaces were done using the same equipment and a similar setup as experiments done previously in this group by Winyann Jang on $TiO_2(001)$ surfaces. My treatment of the experimental details thus necessarily parallels his treatment, found in his thesis [23]. Naturally, any differences between our experimental procedures will be noted.

4.2.1 Laser Systems

Over the last 35 years since their invention, lasers have become one of the most valuable tools available in scientific research. In contrast to other light sources, lasers provide coherent, directional, and monochromatic light with a variety of wavelengths spanning almost the entire UV, visible, and IR spectrum. Lasers also can be designed to provide light at whatever the desired power, from the few-milliwatt laser pointers used in lectures to the multiple watt giants used to cut, weld, and ablate materials in industry. Most solid state and gas lasers provide only a single wavelength of light, or at most several discrete

lines. Tunability, useful for spectroscopy, can be achieved using liquid dye lasers for the visible range or Ti:Sapphire lasers in the near infra-red. The development of high power CW and pulsed lasers has resulted in the rise of nonlinear optical techniques, which can be exploited to frequency double, triple, or Raman shift single line lasers, providing still more variety in available wavelengths.

One of the most commonly used lasers on the market today is the Nd:YAG laser, which operates in the near-IR with a wavelength of 1064.14 nm. This laser can be operated in CW mode, or Q-switched and mode-locked to provide pulsed output. Typically, Nd:YAG laser output is frequency doubled using second harmonic generation in a nonlinear crystal to provide visible output at 532 nm. Additional doubling can also be used to generate UV light at 266 nm, if needed. All second harmonic generation (SHG) experiments presented here were done using a Q-switched, mode-locked, frequency doubled (532 nm) Nd:YAG laser as the incident beam on the sample. A twice doubled UV beam (266 nm) was often used to excite the surface.

4.2.2 Q-switched, Modelocked Nd:YAG Laser System

4.2.2.1 The Nd:YAG Laser

The laser system used for SHG experiments presented here is a modified Quantronics 116 Nd:YAG laser. Neodymium-doped yttrium aluminum garnet (Nd:YAG) crystals possess a combination of mechanical, chemical, and physical properties uniquely favorable to laser operation. The YAG host crystal is hard, is of good optical quality, has a high thermal conductivity, is stable over a large range of temperatures, and has a cubic structure which results in a narrow fluorescent linewidth, leading to low threshold for lasing and high gain [81].

The Nd:YAG laser is a four-level system, and a simplified energy diagram for its operation is shown in Figure 4.1. The ground state of this system is the $^4I_{9/2}$ level. Pumping excites atoms to the pump bands shown, where they then can relax to lower levels. The upper laser level ($^4F_{3/2}$) has a fluorescence efficiency of greater than 99.5%, and a lifetime of

230 μsec. Thus most of the excited atoms eventually wind up at this level, resulting in the population inversion necessary for lasing. Branching ratios from this state are as follows: $^4F_{3/2} \rightarrow {}^4I_{9/2} = 0.25$, $^4F_{3/2} \rightarrow {}^4I_{11/2} = 0.60$, $^4F_{3/2} \rightarrow {}^4I_{13/2} = 0.14$, and $^4F_{3/2} \rightarrow {}^4I_{15/2} < 0.01$. The laser transition occurs between the R_2 component of the $^4F_{3/2}$ energy level and the Y_3 component of the $^4I_{11/2}$ level, with 60% of the population inversion contributing to lasing. As a consequence of Boltzmann's law, at room temperature only 40% of the $^4F_{3/2}$ population is in the R_2 sublevel, with the remaining 60% of the population occupying the lower R_1 sublevel. Lasing only occurs from the R_2 level, which is continually replenished from the R_1 sublevel by thermal transitions. Since the terminal laser level ($^4I_{11/2}$) is far enough above the ground state that it is not populated thermally, the threshold condition is easy to achieve [81].

For our specific laser, the lasing medium is a 4x90 mm rod of YAG host crystal with a doping concentration of about 1% Nd^+. The laser rod is continuously pumped by a 5 kW krypton lamp. These components, which make up the laser head, are located at the foci of a gold, hollow, elliptical cylinder. The laser head is cooled by circulating distilled, de-ionized water. Both the rod and the lamp are protected by flow tubes which guide water flow to provide efficient cooling. The cooling water must have an electrical resistivity not less than 1 MΩ/cm. The resistivity of the water was measured previously [23] to be 3 MΩ/cm, an acceptable value. Additionally, the glass flow tube around the laser rod absorbs any UV light produced by the krypton lamp, since such light is harmful to the laser rod. Heat generated by the lamp is carried away by flowing tap water through a heat exchanger, which keeps the primary cooling water at a temperature of 24°C. An internal sensor turns off the power to the krypton lamp if the temperature of the cooling water exceeds about 28°C.

The laser cavity is made up of a concave-convex resonator. The high-reflecting end-mirror of the cavity is a 100% reflecting concave mirror, and the output coupler is an 88% partially reflecting mirror with a radius of curvature of 1 meter. The optical cavity length is 1.5 m, though the separation between the two mirrors is only 1.4 m. A high-quality optical flat plate made of fused silica is inserted at Brewster's angle (55.6° for fused silica with n = 1.46) so that the laser light is polarized vertically. A 1 mm diameter aperture

Figure 4.1: Simplified energy level diagram for a Nd:YAG laser.

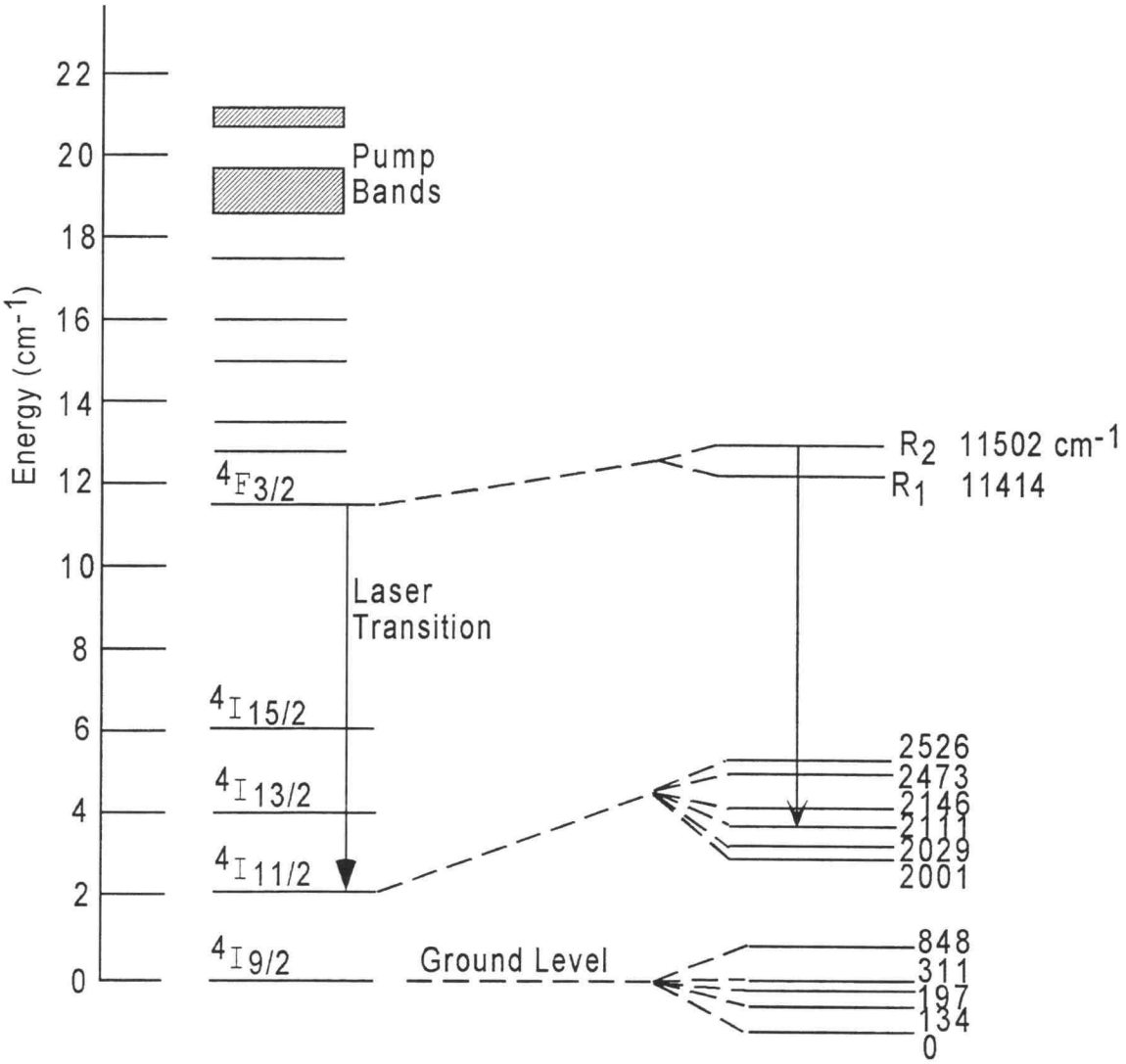

is placed in the cavity so that all lasing modes except TEM_{00} are eliminated [23]. The mirrors are mounted on a super invar rod with a very small thermal expansion coefficient. This minimizes variation of cavity length and changes in component location as temperature fluctuates (see Section 4.2.2.4). When operated CW using only these components, this laser produces about 8.5 Watts (W) of infra-red output at a wavelength of 1064.14 nm.

Nonlinear optical studies require very high laser intensities. These are achieved by compressing the energy found in a CW-mode laser into pulses of large amplitude, but short duration. This results in a drop in average power output, but a large increase in peak power output. The desired energetic pulses are achieved by Q-switching and mode-locking the laser. Mode-locking produces pulses down to a few picoseconds (ps), while Q-switching produces grand pulses a several hundred nanoseconds (ns) in duration. The combination of the two results in a pulse train several hundred nanoseconds long that is made up of about 30 pulses of picosecond width. If pulses shorter than a picosecond are required, mode-locked pulses must be chirped and further compressed. This section describes active mode-locking for the Nd:YAG laser; the following section discusses Q-switching.

4.2.2.2 Active Mode-locking

In a laser that has not been mode-locked, competition between longitudinal cavity modes occurs. This is due to the lack of any definite relationship between the amplitudes and phases of the various modes. Laser output is just the time-averaged statistical mean value of the combined modes. Transverse modes are easily restricted to TEM_{00} by inserting an aperture of appropriate diameter, as is done for the laser used here. There can be, however, as many as a few hundred longitudinal modes within the lasing frequency bandwidth. Each of these modes has a discrete frequency, and each resulting spectral line in the frequency domain is separated by the axial mode interval $\frac{c}{2L}$ where c is the speed of light (appropriately modified to account for the refractive indices of the various cavity elements) and L is the effective cavity length. But the phase distribution of these modes is random, causing the laser intensity to fluctuate randomly in the time domain. The result is known as temporal incoherence, which is just a time-varying power output. Mode-locking forces the modes

to have a fixed phase relationship, removing these random fluctuations. The result is a periodic train of short pulses with equal intensity and period $T = \frac{2L}{C}$.

Mode-locking can be achieved by modulating the loss of the laser at a frequency equal to the inter-mode frequency spacing of the resonator ($f_{mod} = \frac{c}{2L}$). An amplitude modulator with this frequency, placed close to a mirror in the laser cavity, will generate side-bands on each axial mode that overlap with adjoining modes. This couples all the modes within the laser linewidth so that they have a well-defined amplitude and phase through the modulator. The stability of the amplitude and phase relationships between the modes grows with each round trip through the laser. In the time domain, this means that if a pulse reaches the modulator during a low loss state, it passes through the modulator without modification. This pulse will then produce gain in the lasing medium, and since the modulation period is equal to the round trip time of the laser, it will return to the modulator when the modulator is again at a low loss state, resulting in repeated amplification of the pulse. The amplitude of such a pulse will consequently grow to a stable value. Conversely, any pulse that arrives at the modulator in a high loss state will have its amplitude successively attenuated with each pass through the modulator, such that after a few round trips it will disappear. Thus the modulator induces pulses with large, stable amplitudes. The mode-locked laser output is thus a stable, repeating series of pulses of equal amplitude and period $T = \frac{2L}{C}$ such that the output power now has temporal coherence [66, See Section 11.2].

So to mode-lock a laser, some component must be introduced into the cavity that alternates between being a low-loss and a high-loss medium with a frequency that can be set to match the intermode frequency spacing. For our laser system, this is done using the acousto-optic effect. An acousto-optical fused silica block is inserted near the rear (100% reflecting) mirror of the resonator. The block is slightly wedged on the long sides to avoid etalon effects, and is anti-reflection coated to reduce insertion loss. This block is placed with the wedged surfaces facing the laser beam path. A piezoelectric transducer driven by a 7.5 W RF signal launches an acoustic wave into the block from one of the non-wedged sides. The block is cut so that this acoustic signal establishes a standing acoustic wave between the parallel surfaces of the block. This results in a periodic variation of the index of refraction of the block through the photoelastic effect [66, See Section 14.8]. This variation scatters

the incident optical beam. Setting the angle between the laser beam and the acoustic plane wave to the Bragg angle [66, See Section 14.9] maximizes this scattering loss, thus maximizing loss in the modulator. Since the modulator is driven by a sinusoidal source, the acoustic standing wave is produced, and then vanishes, twice with every oscillation of the source. The result is alternating states of low and high loss in the block, as needed to produce mode-locking.

Laser output is generated by partial transmission of the pulses circulating in the cavity through the output mirror. These pulses are spaced by the round trip transit time, and their width τ_0 depends on the number N of axial modes which are locked in phase, and hence the lasing bandwidth $\Delta\nu$ according to [66, See Section 11.2]:

$$\tau_0 = \frac{2L}{cN} \approx \frac{1}{\Delta\nu}. \tag{4.1}$$

The laser gain bandwidth here is about 0.045 nm, corresponding to $\Delta\nu \approx 12$ GHz (since $c = \nu\lambda$, $\Delta\nu = \frac{-c}{\lambda^2}\Delta\lambda$). Equation 4.1 then predicts a pulse width of about 80 ps. The actual pulse width, measured using autocorrelation [78], is 100 ps, in good agreement with the theoretical value. Thus the laser output consists of pulses 100 ps in duration, repeating at a rate of 100 MHz (spaced by 10 ns). When mode-locked only, our Nd:YAG laser output power is about 7.5 W at 1064 nm. Since there are $100\text{x}10^6$ pulses each second, this corresponds to a peak pulse energy of $7.5\text{x}10^{-8}$ Joules/pulse.

4.2.2.3 Q-switching

To increase the peak energy of each pulse, the laser is Q-switched. This takes the laser out of mode-locked CW operation where pulses are continuously produced. Instead, repeating "giant" pulses of larger amplitude and hundred-nanosecond duration are created. These "giant" pulses actually contain many discrete mode-locked pulses in a pulse train (about 30 pulses/train) which have significantly larger peak energy per pulse than when mode-locked only.

The quality factor Q of a laser is defined as the ratio of the energy stored in the resonator to the power loss in the resonator. A laser in CW operation has a high Q-value,

indicating little loss in the cavity. In these circumstances, the population inversion in the gain medium is constantly kept just a little above threshold by stimulated emission. The resultant power output is steady, but relatively low. If a loss mechanism is introduced into the cavity, however, the Q-value decreases. The population inversion in the gain medium increases as more and more atoms are pumped above threshold but not stimulated to make the lasing transition. If the loss mechanism is then removed just as this population inversion reaches its peak value, the Q-value is restored, and the population inversion rapidly depletes in a burst of emission (the "giant" pulse) until the inversion is exhausted.

As with mode-locking, Q-switching modulation is achieved using an acousto-optic fused silica block driven by a RF source. The block, placed near the front mirror of the cavity, is again slightly wedge-shaped, anti-reflection coated, and inserted so that the wedged sides face the laser beam path to eliminate etalon effects. As with the mode-locking modulator, the Q-switching modulator must be placed at the Bragg angle to maximize loss. But for Q-switching, the acousto-optic mechanism is slightly different. Here a standing wave is not established. Rather, the acoustic wave originates at the RF source on a flat face of the fused silica block, makes one pass from the source to the opposite flat end of the block, and is terminated through absorption by a metal plate. The laser beam is scattered as a consequence whenever the RF signal is present, resulting in loss and a decrease in Q-value, and allowing the population inversion to increase dramatically. When the RF signal is subsequently removed, loss is again minimized, the Q-value is high, and the "giant" pulse is emitted as the population inversion depletes. Switching the Q-value back and forth in this way creates periodic "giant" pulses (actually pulse trains), and the rate at which these pulses repeat can be varied by varying the rate at which the RF source is turned off and on. Our Q-switching rate is 500 Hz, producing a new "giant" pulse every 2 ms.

The combined result of Q-switching and mode-locking our laser is repeating trains of about 30 energetic mode-locked pulses, each still 100 ps wide and separated by 10 ns. Such trains repeat every 2 msec (500 Hz switching rate). When Q-switched and mode-locked the laser power output is about 0.8 W, which is considerably lower than the 7.5 W output observed for mode-locking only. But for the mode-locked laser, the 7.5 W output came from 100×10^{6} pulses/second, corresponding to only 7.5×10^{-8} Joules/pulse. For the Q-switched

laser, the 0.8 W of output power comes from only 15000 pulses/second, corresponding to $5.3x10^{-5}$ Joules/pulse. Thus Q-switching increases the energy per pulse by a factor of 10^3.

4.2.2.4 Stabilizing Laser Pulses and Maximizing Laser Power

To successfully execute nonlinear optical experiments, the pulsed output of the Nd:YAG laser must be stable, both in power output and in pulse width. This stability is compromised by thermal expansion of cavity elements as well as thermal fluctuations in index of refraction of the modulators. Degradation of mode-locking occurs for very small variations in cavity length, while Q-switching is less sensitive to such changes. Both Q-switching and mode-locking stability are compromised by thermal changes in the refractive index of the modulators. Each acousto-optic modulator is temperature stabilized by being attached to a Peltier plate [78]. Heat is carried away from the modulator by this Peltier plate, which is cooled by direct contact with a copper heat exchanger that uses constantly flowing tap water. A thermal sensor imbedded in the modulator base monitors temperature, and a control circuit that references this temperature operates the Peltier.

Stable mode-locking requires an exact match between cavity length and modulation frequency. If cavity length fluctuates, frequency mismatch will occur, leading to broader, weaker pulses. To hold the cavity length as constant as possible, the distance between the rear and front mirror must be rigidly controlled. This is usually achieved by attaching the laser components to a metal base-plate. Since thermal expansion of such a base-plate will necessarily move the laser components, a material with a very small thermal expansion coefficient is needed to ensure a stable cavity length. The original laser components of the Quantronix 116 Nd:YAG laser used for these experiments were mounted on an aluminum rail. While aluminum is a sturdy and light material that is commonly used for optical mounts and holders, it has a large thermal expansion coefficient, and thus is not a good material when thermal expansion concerns surface.

The modulation frequency for mode-locking was chosen to be $f_{mod} = \frac{c}{2L}$ to ensure match with the axial mode separation. If the end-mirrors of our cavity of length L are

Table 4.1: Mismatch of mode-locking due to thermal expansion of structural materials used in the laser cavity

material	$\alpha(10^{-6}/°C)$	$\Delta L(microns/°C)$	$\Delta f_{mod}(Hz/°C)$
aluminum	26	39	2600
iron	12	18	1200
invar	1.8	2.7	180
super invar	0.36	0.54	36

fastened to a metal base-plate with thermal expansion coefficient α, then any fluctuation ΔL in the cavity length results in a frequency mismatch of

$$\Delta f_{mod} = -\frac{c}{2L^2}\Delta L. \tag{4.2}$$

Since thermal expansion is linear, $\Delta L = L\alpha\Delta T$, and a change in temperature of 1°C results in a cavity length change of $\Delta L = L\alpha$. Combining this with Equation 4.2 allows frequency mismatch to be calculated using

$$\Delta f_{mod}(/°C) = -\frac{\alpha c}{2L}. \tag{4.3}$$

Using L=1.5 meters, and thermal expansion coefficients for four common metals, Table 4.1 shows the mode-locking frequency mismatch that can be expected for each degree of temperature variation in the laser. Since mode-locking of Nd:YAG only allows a few hundred Hz of frequency mismatch before axial modes go completely out of phase, it is clear that super invar should be used for the base of this laser.

Originally, the Quantronix 116 Nd:YAG laser components were placed on an aluminum base rail. This rail would expand 39 $\mu m/°C$, resulting in a frequency mismatch of thousands of Hertz for only relatively small changes in local temperature. This made mode-locking somewhat variable. For this reason the aluminum base was discarded and replaced with a super invar rod, which is used to maintain the distance between the front and back mirrors. It has a 3/4 inch diameter and is 5 feet (1.52 m) long. The rod is tightly inserted into two aluminum blocks which serve as mounts for the mirrors. The rear aluminum block is

fastened directly to the optical table, while the front aluminum block is attached to a free-moving translation stage that is bolted to the optical table. This fixes the distance between the blocks to the length of the super invar rod, and prevents the distance between them from varying with any thermal expansion of the optical table. The front mirror (output coupler) of the laser is mounted directly to the front aluminum block, while the back mirror is placed on a differential translation stage that is mounted to the back aluminum block. This allows very precise placement of the cavity length through fine adjustments of the position of the back mirror. Thermal expansion of the aluminum mounting blocks and stages is negligible because both mirrors are centered on their mounts, and thus sit atop fixed points. The laser head assembly and all other cavity elements, including modulators, are fixed to the optical table. These modifications, made prior to my experience with this laser [23, 78], give a relatively stable cavity length and allow for effective mode-locking.

Despite this improvement, stabilizing the laser remains one of the more challenging aspects of these experiments. Thermal fluctuations still result in small changes in refractive index and placement of cavity elements, resulting in a tendency for the laser to slowly de-tune from optimal performance with use. Stable windows of operation can be found, though, and close monitoring of laser output power during experiments allows periods of instability to be identified and accounted for in data analysis.

4.2.3 Frequency Doubling the Nd:YAG Output

The 1064 nm output of the Nd:YAG is not used in the experiments presented here. Instead, this output is frequency doubled to produce visible (green) output at 532 nm. The resulting green beam is then used as the probe beam for SHG experiments. To generate the green beam, a nonlinear crystal of $KTiOPO_4$ (KTP) is used to convert the incident 1064 nm light to the desired 532 nm through second harmonic generation. The following sections discuss in detail the process by which optical frequency conversion occurs in crystals, and the concerns that must be addressed when selecting an appropriate crystal for a particular application.

4.2.3.1 Second Harmonic Generation in Nonlinear Crystals

Nonlinear materials are often used to convert the output of a laser from its fundamental wavelength to another that is of more use in a particular application. Additionally, these crystals can be used to mix the output of two or more lasers to generate still more variety in coherent output. Multi-wave mixing processes such as sum frequency generation, difference frequency generation, second harmonic generation, third harmonic generation, and many others are used for these purposes. Second and third harmonic generation in particular are the best and most commonly used means of converting the IR output beam of a Nd:YAG laser to either a visible (532 nm) or UV (355 nm) beam. Of particular interest here is generation of 532 nm light using second harmonic generation. Nonlinear crystals such as KD*P, (KD_2PO_4), ADP ($NH_4H_2PO_4$), KTP ($KTiOPO_4$), BBO (β-BaB_2O_4), LBO (LiB_3O_5) and others have been developed for this purpose.

Second harmonic generation, as discussed previously in the theoretical portion of this thesis (see Section 3.3), only occurs in materials that have non-centrosymmetric structures. For such dielectric materials, intense incident radiation at frequency ω induces a nonlinear polarization at 2ω which then radiates coherently. The efficiency of this process depends on the nature of the incident light as well as on the nonlinear behavior and optical quality of the frequency-doubling crystal. Of critical importance is the geometrical arrangement of the three propagating waves in the crystal (the two annihilated photons at ω and the generated at photon at 2ω). Finding the optimal relationship between these waves is known as "phase-matching", and the details of determining what phase-matching conditions are necessary for efficient second harmonic generation are described here.

Solving Maxwell's equation for the coupled fundamental and harmonic waves produced and propagating in an anisotropic crystal allows the conversion efficiency for the second harmonic beam from the incident beam to be determined. This derivation, which relies on a plane wave approximation and takes into consideration depletion of the incident beam, results in an expression for the conversion efficiency η as follows [64, 65, 62, 66]:

$$\eta = \frac{P_{2\omega}}{P_\omega} = \tanh^2\left[C\left(\frac{P_\omega}{A}\right)^{\frac{1}{2}} \frac{\sin\left(\frac{\Delta kl}{2}\right)}{\frac{\Delta kl}{2}}\right]. \tag{4.4}$$

Here P_ω and $P_{2\omega}$ are the power of the input fundamental beam and the generated harmonic beam, respectively; A is the area of the fundamental beam; l is the crystal length, and $\Delta\vec{k} = \vec{k}_\omega + \vec{k}_\omega - \vec{k}_{2\omega}$ is the phase mismatch between the wavevectors of the fundamental and harmonic beams. The factor C is related to the nonlinear susceptibility $\chi^{(2)}$ of the crystal by

$$C = \left(\frac{32\pi^3\omega^2}{c^3\epsilon_\omega\sqrt{\epsilon_{2\omega}}}\right)^{\frac{1}{2}} \chi^{(2)}_{eff} \tag{4.5}$$

where $\chi^{(2)}_{eff} = \hat{e}_{2\omega} \cdot \chi^{(2)} : \hat{e}_\omega\hat{e}_\omega$ is the effective nonlinear susceptibility. Here ω is the fundamental frequency; ϵ_ω and $\epsilon_{2\omega}$ are the permitivities of the dielectric medium at the fundamental and harmonic frequencies respectively; and $\hat{e}_\omega$ and $\hat{e}_{2\omega}$ are the polarizations of the fundamental and harmonic beams respectively.

From this it is clear that a large nonlinear susceptibility of the doubling medium and high incident laser power are both required to achieve large conversion efficiency. Additionally, Equation 4.4 shows that a phase-matching condition $\Delta\vec{k} = 0$ is also required for efficient nonlinear conversion. This condition can be met in several ways, depending on the nature of the nonlinear medium and the geometry of the incident and propagating waves.

If the fundamental and harmonic beams are to be collinear, there are two ways to satisfy the phase-matching criterion. If the two fundamental photons (frequency ω) annihilated in the second harmonic generation process have parallel polarizations, then the phase-matching condition demands that the refractive index of the nonlinear medium satisfies:

$$n_{2\omega} = n_\omega. \tag{4.6}$$

This is called parallel or Type I phase-matching. But if the two fundamental photons that are annihilated can have orthogonal polarizations then collinear phase-matching is achieved when

$$n_{2\omega} = \frac{1}{2}\left(n_\omega + n_\omega^{'}\right), \tag{4.7}$$

where n_ω and n'_ω are the material's refractive indices for light with the two orthogonal polarizations used. This is known as orthogonal or Type II phase-matching.

Dispersion prevents phase-matching from occurring in isotropic materials. It is thus necessary to use a uniaxial birefringent crystal or a biaxial crystal to achieve efficient second harmonic generation. In the first case Type I phase-matching is employed, while in the second case either Type I or Type II can be used. Over the years, various nonlinear crystals have been used to frequency double the IR output of our Nd:YAG laser. In early experiments [23], a KD*P (uniaxial birefringent) crystal was used with Type I phase-matching. This was later replaced with a KTP (biaxial) crystal with Type II phase-matching. For the experiments presented here, KTP alone was used. In addition, frequency doubling of this type is also used to generate 266 nm UV from a portion of the 532 nm output of the doubled YAG. This UV was generated using an ADP (uniaxial birefringent) crystal in early experiments, and a BBO (uniaxial birefringent) crystal in later experiments. The following sections discuss the details of phase-matching in these crystal types.

4.2.3.2 Type I Phase-matching in Uniaxial Birefringent Crystals

In a birefringent crystal, the index of refraction is a function of the polarization of light propagating in the crystal. For this reason, the phase velocity in the medium is also polarization dependent. If the crystal is uniaxial the index of refraction is constant for light polarized perpendicular to the optical axis, but varies with propagation direction for light polarized in the plane containing the optic axis. "Ordinary" waves, or "o-rays", are those polarized perpendicular to the optic axis, while "extraordinary" waves, or "e-rays" are those polarized in the plane of the optic axis. The index of refraction n^o for an ordinary wave is thus constant, regardless of direction of propagation, while the index of refraction $n^e(\theta)$ for an extraordinary wave varies with propagation direction according to [66, See Section 5.4]:

$$\frac{1}{(n^e(\theta))^2} = \frac{\cos^2\theta}{(n^o)^2} + \frac{\sin^2\theta}{(n^e)^2} \tag{4.8}$$

where n^e is the index for extraordinary propagation along the optic axis, and θ is the angle between the optic axis and the direction of extraordinary propagation.

Figure 4.2: Index surfaces for negative uniaxial crystals.

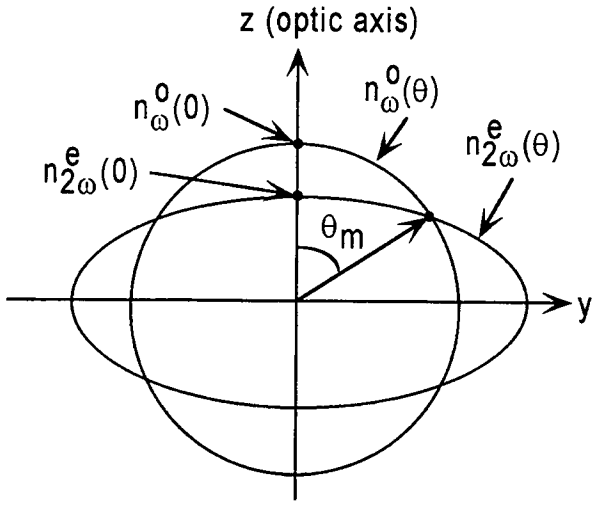

Both the ordinary and extraordinary waves in a birefringent crystal are subject to dispersion, making it impossible to satisfy the Type I phase-matching condition of Equation 4.6 if both the fundamental and the harmonic are beams of the same type (both ordinary or both extraordinary). But Equation 4.6 can be satisfied under certain conditions if the waves are of different type (one ordinary and one extraordinary). Figure 4.2 best illustrates this. Here the z-axis corresponds to the optic axis in this figure. The angle θ is between the incident beam and the optic axis as shown, and an additional angle ϕ (not shown) gives the angle between the incident beam and the x-z plane. This shows the "index surfaces" of the material, which represent the magnitude of the index of refraction in any direction of propagation. The index surface of an ordinary wave (constant index) is a sphere, while the index surface of and extraordinary wave is an ellipsoid (the refractive index varies with direction θ of propagation). Places where index surfaces at the fundamental frequency overlap with index surfaces at the harmonic frequency are where phase-matching can occur. With the same ray type, index surfaces such as these never overlap, since dispersion leads to concentric circles for o-rays and concentric ellipses for e-rays. But if one wave is ordinary and the other extraordinary, overlaps can occur.

For a "positive" uniaxial crystal, with ($n^e > n^o$) along the optic axis, the index surfaces will not overlap in general. But a "negative" uniaxial crystal has ($n^e < n^o$) along the optic axis, such that an angle θ_m can exist for which $n^e_{2\omega}(\theta_m) = n^o_\omega$, satisfying the Type I phase-matching criterion. Substituting this condition into Equation 4.8 and solving for the angle needed to achieve this phase-matching yields [66, 62]:

$$\sin^2\theta_m = \frac{(n^o_\omega)^{-2} - (n^o_{2\omega})^{-2}}{(n^e_{2\omega})^{-2} - (n^o_{2\omega})^{-2}}. \tag{4.9}$$

Thus bringing the fundamental beam in at the phase-matching angle θ_m for a negative uniaxial crystal results in efficient production of second harmonic signal, as desired.

In practice, crystals of this type are usually cut so that the optic axis is at the phase-matching angle when the input surface is perpendicular to the incident beam. The angle ϕ between the optic axis and the x-axis must also be carefully chosen to maximize the effective nonlinear susceptibility for the polarizations used.

Many uniaxial crystals exist that can be employed to double the Nd:YAG 1064 nm output, generating 532 nm light. Initially, a 30 mm uniaxial KD*P crystal was used for this purpose. This crystal had an effective nonlinear susceptibility that could be calculated using [82] $\chi^{(2)}_{eff} = \chi^{(2)}_{zxy} \sin\theta_m \sin 2\phi$. Table 4.2 lists the refractive indices [83] for KD*P at the fundamental (1064 nm) and harmonic (532 nm), allowing the phase matching angle to be calculated using Equation 4.9. The result is $\theta_m = 36.7°$, and $\phi = 45°$ is chosen to maximize $\chi^{(2)}_{eff}$. Unfortunately, the conversion efficiency for this crystal was only 20%, leading to only 200 mW of generated green 532 nm light for 1 W of 1064 nm Nd:YAG input. Because of this low efficiency, which resulted in low overall signal-to-noise ratio for the experiment, the KD*P crystal was replaced with a biaxial KTP crystal, which will be discussed in the next section.

Another uniaxial crystal was used later in the beam path to convert a portion of the 532 nm light into 266 nm UV light needed for surface excitation. Initially, a 25 mm ADP ($NH_4H_2PO_4$) crystal was used for this purpose. Since ADP belongs to the same symmetry class as KD*P, its effective nonlinear susceptibility takes the same form as that used for KD*P. A phase-matching angle of 80.2° results when the appropriate indices for ADP (fundamental 532 nm and harmonic 266 nm light) found in Table 4.2 [84] are substituted into

Table 4.2: Refractive indices for KD*P and ADP doubling crystals at the appropriate frequencies for calculation of phase-matching angle.

**Extrapolated from values given for nearby wavelengths.

Material	wavelength	n^o	n^e	θ_m
KD*P[83]	1064 nm (fund)	1.49314	1.45824	36.7°
	532 nm (harm)	1.507**	1.468**	
ADP[84]	532 nm (fund)	1.52754	1.48153	80.2°
	266 nm (harm)	1.57913	1.52609	
BBO[84]	532 nm (fund)	1.67421	1.55466	48.0°
	266 nm (harm)	1.75853	1.61262	

Equation 4.9. When 300 mW of 532 nm green was focused using a 20-cm focal length lens into this ADP crystal, 20 mW of second harmonic at 266 nm was generated, corresponding to a conversion efficiency of 7%. When this crystal was inadvertently damaged, it was replaced by a BBO crystal which could promise greater efficiency. BBO has a phase matching angle of 48°, calculated from the indices in Table 4.2 [84]. The 5x5x7 mm crystal used in replacement of the damaged ADP crystal provides 35 mW of second harmonic at 266 nm for 300 mW of green input, corresponding to an efficiency of 12%.

4.2.3.3 Type II Phase-matching in Biaxial Nonlinear Crystals

In biaxial crystals, the equation governing the index surfaces is more complicated than that of uniaxial crystals, and is found to be [85]:

$$\frac{\sin^2\theta\cos^2\phi}{n^{-2}-(n^x)^{-2}}+\frac{\sin^2\theta\sin^2\phi}{n^{-2}-(n^y)^{-2}}+\frac{\cos^2\theta}{n^{-2}-(n^z)^{-2}}=0. \tag{4.10}$$

Here x, y, and z are the principal axes of the crystal, n_x, n_y, and n_z are the principle refractive indices along these respective axes, and n is the refractive index for waves propagating at angle θ from the z-axis and angle ϕ from the x-axis. This equation holds separately (with appropriate indices) for both the fundamental and the generated harmonic frequencies, and involves solving numerically for $\phi(\theta)$. For crystals with normal dispersion and principal axes

that do not vary with frequency, the phase-matching direction can determined by finding the intersection between the index surfaces found using Equation 4.10 for both frequencies [86]. Either Type I and Type II phase-matching conditions can be chosen. In all, fourteen types of phase-matching loci have been classified according to the relationship between the principle indices by solving Equation 4.10 together with a phase-matching condition for various types of biaxial crystals and geometries [87].

When waves propagate in one of the principle planes (xy, yz or xz), determination of phase-matching angle follows closely the arguments used for uniaxial crystals. In KTP crystals [88, 89, 90], as an example, efficient generation of second harmonic from 1064 nm input is found for Type I phase-matching at $\theta = 90°$ (on the xy plane). Symmetry arguments for this crystal, however, indicate that a much larger nonlinear susceptibility can be realized using Type II phase-matching at this angle, so Type I is not typically used. The Type II phase-matching that is used instead occurs when

$$n^s_{2\omega}(\phi_m) = \frac{1}{2}\left(n^s_\omega(\phi_m) + n^z_\omega\right) \tag{4.11}$$

where $\hat{s}$ denotes a beam polarized on the xy plane and ϕ_m is the phase-matching angle to be determined for given refractive indices.

With beams restricted to the xy plane ($\theta = 90°$), Equation 4.10 simplifies to

$$\frac{1}{n^s_\omega(\phi)} = \frac{\sin^2\phi}{\left(n^x_\omega\right)^2} + \frac{\cos^2\phi}{\left(n^y_\omega\right)^2}. \tag{4.12}$$

for the fundamental index surface, with an identical second equation holding for the harmonic index surface. These expressions for the indices can now be substituted into Equation 4.11, resulting in a complicated expression relating the phase-matching angle to the refractive indices of the principle axes:

$$\left[\frac{\sin^2\phi_m}{\left(n^x_{2\omega}\right)^2} + \frac{\cos^2\phi_m}{\left(n^y_{2\omega}\right)^2}\right]^{-1} = \frac{1}{2}\left\{\left[\frac{\sin^2\phi_m}{\left(n^x_\omega\right)^2} + \frac{\cos^2\phi_m}{\left(n^y_\omega\right)^2}\right]^{-1} + n^z_\omega\right\}. \tag{4.13}$$

There is no convenient closed-form solution to this equation, so numerical solution is required once the indices along each principle axis at both frequencies are known.

For these experiments, a 3x3x7 flux-grown KTP crystal was used to frequency double the Nd:YAG output. Refractive indices along the principle axes of this crystal at 1064 nm

Table 4.3: Refractive indices along the principle axes of KTP for 1064 nm and 532 nm light

Wavelength	n^x	n^y	n^z
1064 nm	1.7377	1.7453	1.8297
532 nm	1.7780	1.7886	1.8887

and 532 nm are given in Table 4.3 [91]. Using these values, solution of Equation 4.13 leads to a phase-matching angle of $\phi_m = 24.3°$. In practice, the phase-matching angle may vary from 1 to 2 degrees from this value from crystal to crystal when flux-grown. Hydrothermally grown crystals may have phase-matching angles that vary as much as 5 degrees from this value.

4.2.3.4 Gaussian Beams in Second Harmonic Generation

The plane wave approximation has been invoked to generate Equation 4.4 for second harmonic generation in nonlinear crystals. Once phase-matching concerns have been addressed such that $\Delta k = 0$, this efficiency appears to favor longer crystal lengths. In practice there is an optimum crystal length such that longer crystals result in less efficiency.

Laser beams are Gaussian in nature, and are always focused into the nonlinear doubling crystals. This increases the power density, and thus the efficiency, of the harmonic generation. But this also decreases the cross-sectional area of the beam, threatening the plane-wave approximation. For a Gaussian profile characterized by $\exp(-z^2/W_0^2)$, where W_0 is the beam waist, distances along the beam axis in the focal region are described using the confocal parameter $b = kW_0^2$. This parameter corresponds to a distance from the axis that is between the cross-sectional area determined by beam waist and a point where the cross-sectional area along the axis is twice that of the beam waist. As long as the crystal length is shorter than this parameter, the plane-wave approximation is valid, with the substitution $A = \pi W_0^2$. In this region, focusing the beam further will result in greater conversion efficiency. But once the limit $b \approx l$ is obtained, any further focusing of the beam will invalidate the plane-wave approximation and result in less efficiency. (A numerical study

[92] of conversion efficiency with focused Gaussian beams further narrowed this condition by determining that optimum focusing occurred for $b = l/2.8$ for a given l. The limit $b \approx l$ is adequate to approximate this with little cost in efficiency.) Thus for a crystal of a given length, there is a limit to how tightly one can focus the fundamental input beam and still obtain good conversion efficiency. The result is a trade-off between power density obtained by focusing and crystal length: shorter crystals allow tighter focusing, and thus higher power densities, but provide less nonlinear material in which the harmonic frequency can be generated; longer crystals provide more nonlinear material for frequency conversion, but demand less focused beams and thus less power density. An optimum focusing condition of $b \approx l$ results.

4.2.4 Optical Components and Set-up for SHG Experiments

Second Harmonic Generation on the $TiO_2(110)$ surfaces studied here was carried out using the frequency-doubled output of the Q-switched, mode-locked Nd:YAG laser system described in the previous section. Figure 4.3 shows a schematic diagram of all of the optical components used to modify and direct the laser output to carry out these experiments. This section will describe in detail each optical component in the beam paths shown, and will also address data collection electronics.

4.2.4.1 Obtaining a Pure 532 nm Beam

Focusing the 1 Watt infrared output of the Nd:YAG laser into the frequency-doubling crystal results in two collinear output beams, one of green harmonic light at 532 nm and the other of the remaining, unconverted fundamental IR light at 1064 nm. If a biaxial doubling crystal (KTP) is used, the output green light has a polarization that is rotated 45° with respect to the input IR beam. In this case, a birefringent quartz plate is set at the appropriate azimuthal angle and rotation angle to rotate the green beam an additional 45° such that it will be perpendicular to the residual IR beam. Then the IR and green are separated using a dielectric coated beam-splitter that reflects 99.9% of the green beam and

Figure 4.3: Schematic of the beam path and optical components used for SHG experiments

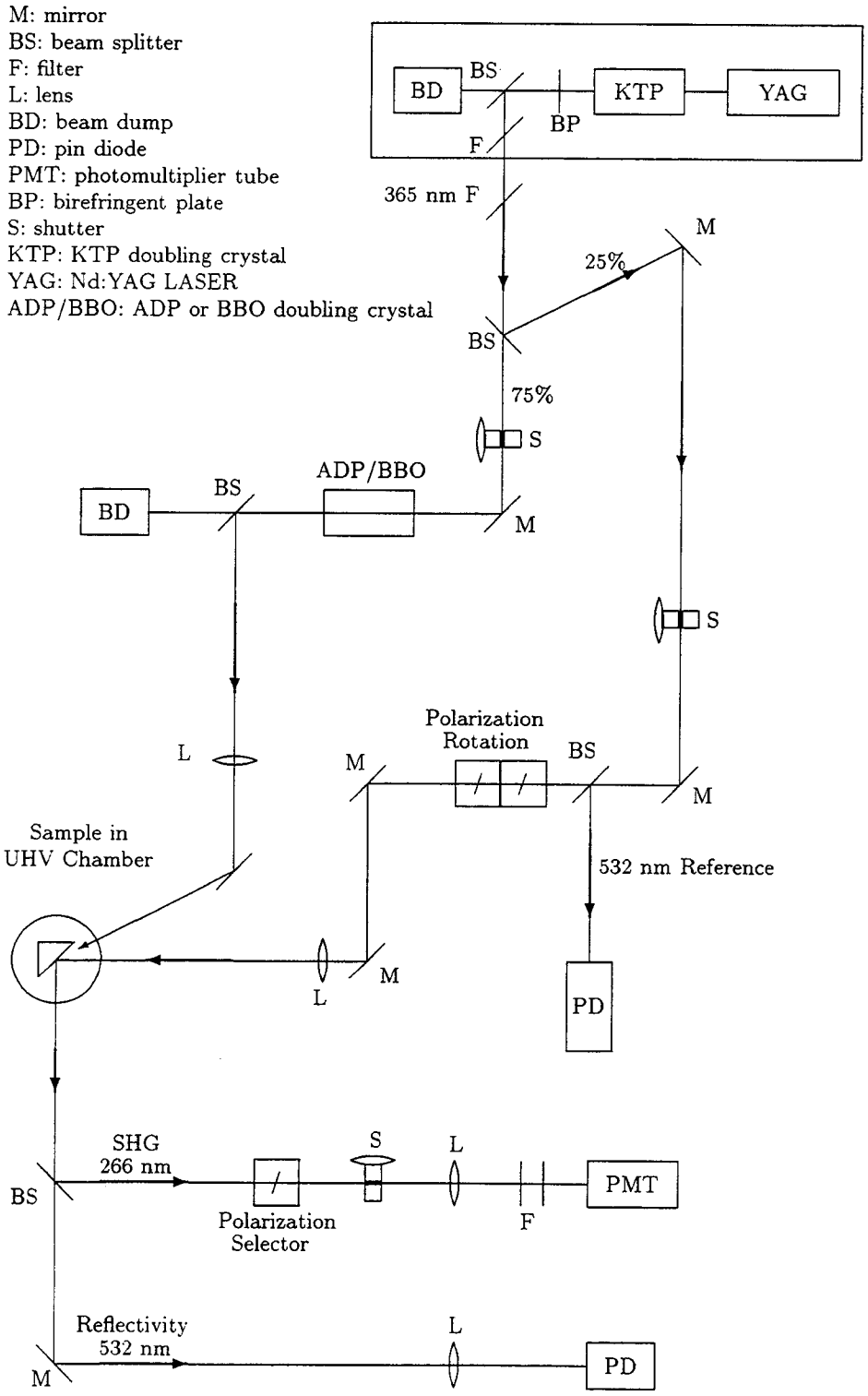

transmits 99% of the IR beam when placed at 45° in the beam path. The transmitted IR beam is dissipated in a beam dump. Finally, the nearly-pure reflected green beam is passed through an IR reflection mirror again set at a 45° angle to remove the last of the residual IR. If the frequency doubling crystal is a uniaxial crystal (KD*P), then the polarizations of the IR and green output beams are perpendicular. The IR and green beams in this case are separated by first directing the beam to the dielectric beam-splitter, and then passing the nearly-pure green reflected beam through a polarizer or IR reflection mirror to remove the remaining residual IR.

The laser system and frequency doubling optics described above are enclosed in a black box with a small aperture cut in the side such that only the pure green beam exits the box. IR leakage from this aperture is less than 30 μW, and is further dissipated by using dielectric mirrors coated for green reflection to direct the beam as it exits the laser. A small amount of the IR third harmonic at 355 nm is also present in the green output. This is removed with minimal insertion loss in the green beam by inserting a glass filter at Brewster's angle early in the beam path. This is necessary because the UV detectors used to measure the SHG signal at 266 nm would also pick up this 355 nm component, giving a false amplification of the signal level.

The result of the above separation and filtering of the doubled beam in KTP results is about 400 mW (this can vary 20 mW from day to day with laser performance) of s-polarized, pulsed light at 532 nm that can be used for experiments. Each pulse train consists of about 30 mode-locked, 100 picosecond pulses each separated by 10 nanoseconds. The repetition rate of Q-switching is 500 Hz, such that a new pulse train is generated every 2 milliseconds.

This green beam performs two functions in SHG experiments presented here. Immediately after the beam has been filtered to contain only 532 nm light it is split into two beams, one for each function. One portion of the beam is focused on the sample and used to probe the TiO_2(110) surface, generating a surface-specific second harmonic (266 nm) signal in reflection. The other portion of the beam is diverted and frequency doubled to generate a 266 nm UV beam that is used to excite the surface. The green beam used to generate SHG signal from the surface will be referred to as the "probe" beam, and the 266 nm UV beam used to excite the surface will be referred to as the "pump" beam. During

UV excitation using the pump beam (at 266 nm), the second harmonic signal generated by the probe beam (also at 266 nm) can not be measured. The 400 mW green beam is divided into two beams using a beam-splitter with a 1 to 3 ratio. Thus 100 mW of green reflects off this beam-splitter and is used to generate the probe beam (and reference signal for normalization), while the remaining 300 mW of green is transmitted and used to generate the UV pump beam. Creation and modification of these beams will be discussed here, beginning with the probe beam.

4.2.4.2 The Probe Beam and Signal Generation

The 100 mW portion of the 532 nm green beam is directed using a mirror to pass through an 32% transmission beam-splitter. This diverts a portion of the beam so that a reference for laser power can be measured and reduces the probe beam power to between 30 and 35 mW. This attenuation is needed so that the applied power density is well below the damage threshold of the surface when the probe beam is focused on the sample. A solenoid-driven shutter is inserted just before this beam-splitter so that the probe beam can be applied to the sample under computer control. The diverted beam is passed through a diffuser and into a pin-diode. The resulting signal is used as a measure of laser power and stability so that signals from the sample can be normalized to exclude fluctuations in laser power. The remainder of the beam then passes through a pair of Fresnel rhombs mounted on a translating stage that allows them to be either placed in the beam path or removed from the beam path. These Fresnel rhombs are used to change the polarization of the green beam from s (the green polarization) to p or circular as needed. The beam then is directed using two mirrors onto the sample in the vacuum chamber through a fused silica window. A lens with focal length 60 cm is used to focus the beam onto the sample, which is positioned in the chamber so that this beam is incident at 45°. The focused spot size of this beam was measured to be 250 μm in diameter, corresponding to a probe beam power density of 40-47 MW/cm^2. This is well below the measured damage threshold of 488 MW/cm^2 for rutile in UHV at 532 nm [23].

The reflected beam has two components: the green reflectivity from the sample and the very weak surface second harmonic (SH) signal that travels collinear with the reflectivity. These come off the sample at 45° and pass out of the chamber through another fused silica window (see Section 4.2.5.1 for a description of the chamber geometry). Both the green reflectivity beam and collinear SH beam are allowed to expand before separation. The SH signal is then extracted from the reflected beam using a dielectric beam-splitter that provides 99% reflection of the 266 nm SH signal when placed at 45°. A polarizer is added to the resulting 266 nm signal path whenever the polarization of the SH signal is to be measured. The SH signal is then passed through two Schott UG5 filters that transmit 45% of the signal at 266 nm but block any remaining green light. The 266 nm signal is then focused using a 14 cm fused silica lens (50% transmission at 266 nm) onto an UV sensitive (visible blind) photomultiplier tube (PMT). The Schott filters, focusing lens, and PMT are all enclosed in a black paper box and swaddled with black cloth to prevent external light from entering the PMT. To further block stray light, the SH signal enters the detection box through an aperture and then must pass through a second aperture 80 cm away before striking the PMT. A shutter just outside the box allows the PMT to be blocked when there is ambient UV (from the pump beam) that could saturate and damage the tube. The PMT is placed about 1.2 meters away from the sample surface so that only the SH signal, which is collinear with the reflected beam, can be detected. This eliminates any possible contributions from isotropic two-photon fluorescence that might be present. The green reflectivity signal that passes through the UV separation beam-splitter is also monitored. This light is directed through a diffuser onto a pin-diode detector.

Photo-current signals from the PMT and pin-diodes are sent to a gated integrator where they are converted to voltages by integrating the entire mode-locked pulse train in a Q-switched pulse. The integrator has a 1 nanofarad capacitor and is gated at the Q-switching frequency of 500 Hz. The integration capacitor is discharged before integration of each pulse train, and integration of the pulse-train occurs about 10 μseconds after the Q-switch pulse is launched. Sampling time is about 4μseconds, and after sampling the circuit holds the voltage until just before the next pulse is launched. Then the voltage signal is further amplified, sent to an inverter that converts the negative voltage to a positive

voltage that is then collected in a computer through a 12-bit analog-to-digital converter. Each data point collected is an average over at least a few hundred Q-switch pulses (shots) to improve the signal to noise ratio. Typically, 2000 shots were averaged per data point. When analyzing data, each reflectivity data point is divided by its corresponding reference signal data point. This normalizes out any fluctuations in laser power. The SH signal however depends on the square of the laser power, so SH signal data points are divided by the square of the corresponding reference signal data points for normalization.

4.2.4.3 The Pump Beam and Surface Excitation

The remaining 300 mW portion of 532 nm laser light that is not used to make the probe beam is diverted and used to create a focused beam of 266 nm UV light. To do this, the 300 mW beam is focused into either an ADP (early experiments) or a BBO (more recent experiments) nonlinear crystal using a 20 cm focal length lens. The crystals are placed at and fine-tuned to their appropriate phase-matching angles to ensure maximum conversion efficiency. The ADP crystal produced 20 mW of second harmonic light at 266 nm under these condition, while BBO generates 35 mW. Two mirrors coated to reflect UV light then direct this beam onto the sample surface. A 40 cm fused silica lens is inserted to focus this beam on the sample. By the time the UV beam passes through the focusing lens and fused silica window, the power has been cut to about 25 mW. The spot size of this UV beam is about 1 mm, corresponding to a peak power density of about 2 MW/cm^2 that is well below the rutile damage threshold [23]. A solenoid-controlled shutter is placed in the beam path before the lens that focuses the green beam onto the doubling crystal so that the UV pump beam can be computer controlled. A great deal of scattered UV light is present whenever the pump beam is on. Some of this scattered light inevitably enters the detection system for the SH signal, causing the PMT to saturate. For this reason the PMT is always shuttered off when the pump beam is shuttered on, and SH signal can not be measured while the surface is being excited by the pump beam.

4.2.5 Ultra-high Vacuum System and Gas Introduction Lines

SHG experiments were performed in a Ultra-high Vacuum (UHV) system with a base pressure of about $1x10^{-8}$ Torr. During experiments various pressures of gas are introduced into the chamber, often to pressures in the Torr range, so that interactions between $TiO_2(110)$ surfaces and gas molecules can be observed *in situ*. Then the system is pumped down again to the base pressure. This frequent cycling is responsible for the relatively high base pressure of the system. A better base pressure (about $1x10^{-9}$ Torr) can be obtained by baking, but can not be re-obtained without baking once gas has been introduced into the system. For XPS experiments presented later, a different chamber with a re-obtainable base pressure of less than $1x10^{-9}$ Torr was used. But *in situ* gas doses in the XPS chamber were limited to pressures less than $1x10^{-6}$ Torr, precluding observation of any high-pressure interactions. Comparison between these SHG and XPS experiments show that the same low-pressure surface-molecule interactions are seen in both chambers, independent of the order of magnitude difference in base pressure between the two chambers. For this reason, the SHG system base pressure is considered "good enough" for these experiments.

4.2.5.1 UHV System for SHG Experiments

The UHV system used for SHG experiments, shown in Figure 4.4, consists primarily of a stainless steel chamber, a mechanical pump, a diffusion pump and an ion pump. Thermocouple and ionization gauges are attached to the chamber and pumping lines in various places to monitor pressure at all stages of the pumping process. A residual gas analyzer (RGA) is attached to the chamber to monitor component gases in UHV. A cold-trap filled with liquid nitrogen is placed between the diffusion pump and the UHV chamber to prevent diffusion pump-oil vapor from entering the chamber. This also greatly reduces chamber pressure by attracting molecules which then adsorb on the cold-trap walls.

The mechanical pump rough-pumps the system down to $1x10^{-2}$ Torr (T), and also serves as a backing pump for the diffusion pump. Two valves control whether the mechanical pump is open to the chamber or to the backing port of the diffusion pump. It is important

Figure 4.4: Ultra-high vacuum system used for SHG experiments

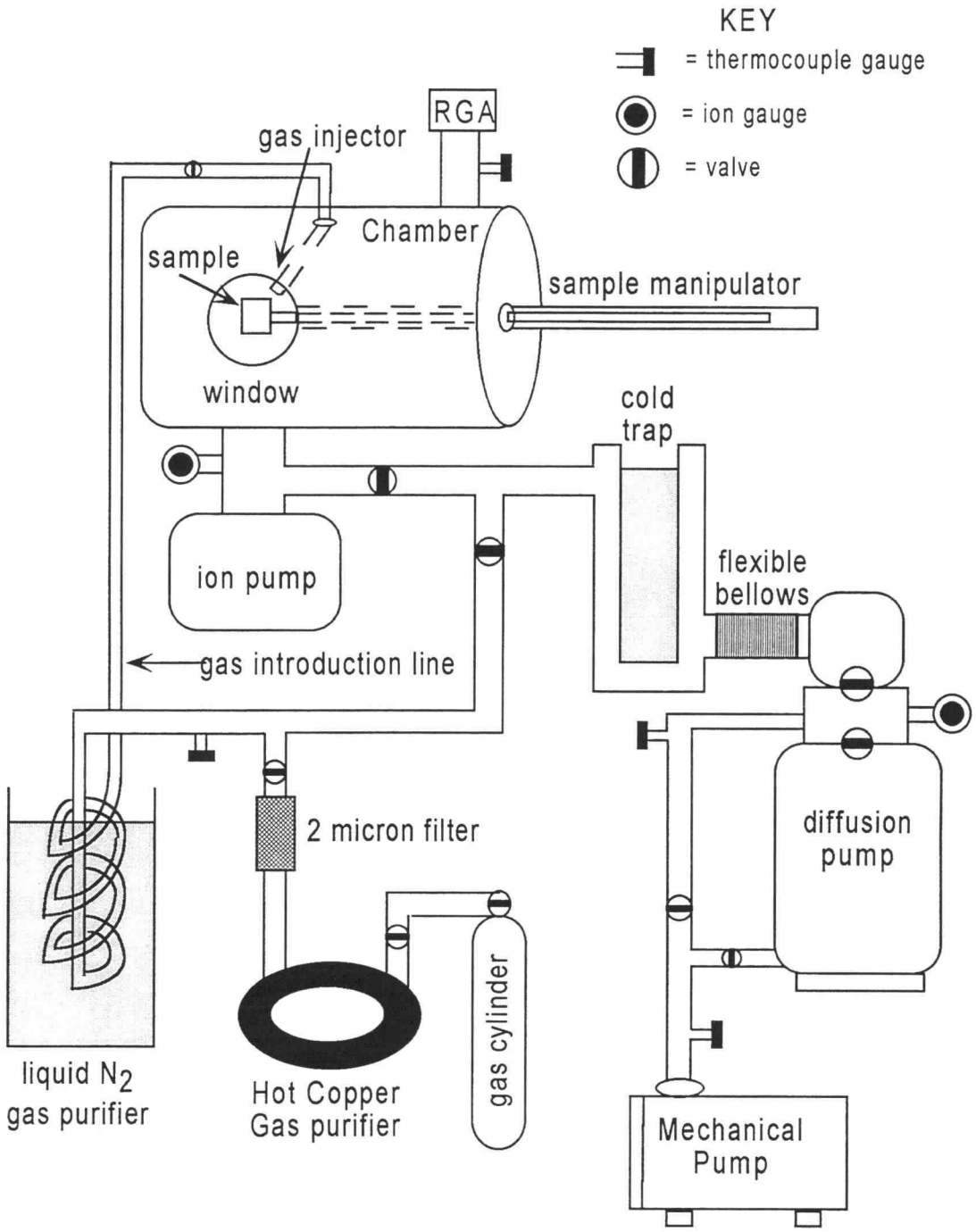

that these valves are not both open at the same time. When changing from roughing to backing, the valve connecting the chamber and the mechanical pump must first be closed, then the valve connecting the backing port of the diffusion pump and mechanical pump can be opened. Likewise to switch from backing to roughing the backing valve must first be closed, and then the roughing valve can be opened. This two-valve system replaces one three-way valve that was used in previous experiments [23] but has since failed. Once the system has been roughed to $1x10^{-2}$ T, and the diffusion pump has been turned on and back-pumped to the same pressure, the valve connecting the diffusion pump to the chamber can be opened. The diffusion pump will then take the system pressure down to $1x10^{-7}$ T. The diffusion pump is externally cooled by flowing tap water, and internally cooled using cold fingers attached to a cryogenic liquid nitrogen reservoir (not shown). Once a chamber pressure of $1x10^{-7}$ T is achieved, the chamber is isolated from the diffusion/mechanical pumping system by closing the main chamber valve. The ion pump is then turned on, and will maintain the system pressure at $2x10^{-8}$ T without further pumping by the diffusion pump. If the system is then baked, this pressure can be improved to yield a base pressure below $1x10^{-8}$ T. Base pressures of $1x10^{-9}$ T and lower have been achieved by extensively baking this chamber, but such base pressures can not be re-obtained without baking once any gas molecules are introduced into the chamber during experiments. Once experiments begin, the ion pump-maintained pressure of about $2x10^{-8}$ T is the best achievable.

The vacuum chamber has three view ports, located in the same optical plane at 45° from each other. The two ports located 90° apart are fitted with fused silica windows to allow transmission of both UV and visible light. One port is used for input of the 532 nm green beam used for SHG and the 266 nm UV beam used for surface excitation. The other port is then used to observe the SHG and reflectivity output signals from the sample. Welded windows were not used because distortions around the edge limit input and exit angles. Also, fused silica windows are fragile under pressure, precluding the use of copper gaskets as vacuum seals. Instead, Viton O-rings are used. This limits the ultimate pressure of the system to the range between $1x10^{-9}$ and $1x10^{-8}$ T obtained using baking and the ion pump, and also dictates that baking be done slowly and at temperatures below about 150°C. The port located between the fused silica ports (at 45°) is made of optical glass

and will block UV. This port is used for viewing the sample when aligning the green laser beam and the UV excitation beam.

Samples are mounted on a stainless steel manipulating rod that translates perpendicular to the plane of the optical ports. This rod is sealed in a barrel that extends out one side of the chamber. The connection between the barrel and the chamber is made through a flexible bellows, and the rod is translated perpendicular to the optical port axis using external magnets that encircle and slide along the barrel, engaging and translating the rod inside. Three translation stages are attached to a support for the barrel, allowing slight adjustments in the rod's position to be made along all axes. The rod is free to rotate about the translation axis, allowing the angle of incidence of light from the optical ports to be precisely set. This angle is set at 45° so that light incident through one of the fused silica ports will reflect off the sample and out the other fused silica port. Samples are mounted on an aluminum holder which can hold up to four samples at one time.

An Omega chromel/alumel K type wire thermocouple (not shown) is attached using stainless steel screws to electrical feed-throughs in the chamber and placed behind the sample holder. This gives an approximate sample temperature. Samples can be heated using a radiant heater that is also attached to an electrical feed-through port on the chamber (also not shown). This heater is made up of a 500-Watt filament in a glass tube, and is capable of heating the sample up to about 250°C. With aluminum sample holders, however, heating should be limited to temperatures below 200°C, where the aluminum vapor pressure becomes appreciable. Care also must be taken during sample heating with the radiant heater to ensure that the Viton O-ring seals on the fused silica optical ports are not heated above 150°C. The radiant heater is used to aid in baking, which is done using heat-tapes and heat-wires wound around the external walls of the chamber. The chamber is baked in this way (to well above 100°C but below 150°C for at least overnight) routinely, to greatly reduce the water vapor content of the residual gases in the chamber.

4.2.5.2 Gas Introduction Lines

Interactions between gas molecules and surfaces can be studied using either *in situ* or *ex situ* probes. *In situ* experiments are desirable for several reasons. Many *ex situ* studies require sample transfer from UHV to a reaction cell and back again, allowing for the introduction of contamination. *Ex situ* studies are also limited in that they can only be used to study interactions through "before" and "after" measurements of the surface, and can not be used to study reactions as they occur. For *in situ* studies, however, it is necessary to introduce the desired gas molecules into the main UHV chamber without also introducing other molecules. This requires a very pure source of gas. Such pure gases can be purchased, but they are expensive, hard to handle, and contamination can still occur as they are transferred from their cylinders to the research chamber. It is much more practical to purchase a lower grade gas and install a gas introduction line that is carefully designed to evacuate, filter, and trap any contaminant gases that may be present. (In many cases, the lower grades of purchased gases are identical to the higher grades, with the only distinction being the testing that is done to ensure gas purity.) As shown in Figure 4.4, this is achieved using a gas introduction system that employs a hot-copper gas purifying section, a 2-micron filter, a 77°K stainless steel liquid nitrogen cold trap, a warming section, and finally a 6-mm diameter stainless steel tube that penetrates into the chamber and releases gas molecules 1 cm from the sample surface. This line is also connected to the main pumping system. This connection is made just past the liquid nitrogen cold trap in the main line, and just before the valve to the chamber, meaning that the gas introduction line can be evacuated to about $1x10^{-7}$ T by the diffusion pump without pump-oil contamination. Valves are installed between each stage of the introduction line to control the flow of gas through each part of the purification process. A thermocouple gauge monitors the pressure in the line. The following discussion is a step-by-step description of gas preparation and purification.

The desired gas cylinder is attached in air to the manifold of reaction gases. All stages of the introduction line up to the gas injector are then rough pumped using the mechanical pump and then further evacuated to about $1x10^{-7}$ T using the diffusion pump. At this point, the hot-copper purifier is not turned on, and the liquid nitrogen cold trap is not

submerged in its liquid nitrogen bath, such that all tubing is at room temperature. A heat gun is then used to systematically bake all sections of the evacuated line to remove any water vapor or other molecules that have adsorbed on the walls of the tube at room temperature. The introduction line is then filled with the desired gas, evacuated again, and re-heated. This purge process is repeated several times, resulting in a clean, evacuated introduction line. Now the copper gas purifier is turned on and allowed to heat up and the liquid nitrogen trap is filled and allowed to cool while the lines are evacuated. (Note: the cold trap can be used without the hot-copper purifier, but the hot-copper purifier must always be followed by the cold trap. This is because one product of the hot copper purification process is water vapor, which must be removed from the gas in the cold-trap before the gas is introduced into the chamber.) Once the temperatures of these elements have stabilized, gas can slowly be bled through each stage of the purification process and introduced into the chamber.

The cold-trap in the introduction line is used mainly to freeze out any water that may remain in the introduction line or be present in the introduced gas. Care must be taken, however, when using this to trap gases that have melting points above that of liquid nitrogen. For example, O_2 (melting point = -218°C), will not freeze out on the walls of the liquid nitrogen (m.p. = -210°C) cold-trap, but N_2O (m.p. = -91°C) will. Thus the liquid nitrogen cold-trap can be used to trap O_2, but may cause problems if used to trap N_2O. Dry ice (m.p. = -57°C) can be substituted for liquid nitrogen in the cold-trap to successfully remove water from gases such as N_2O, though this was not done here. Here the liquid nitrogen reservoir was only partially filled and the cooling coils were only partially submerged, such that most of the cold trap was warm enough that N_2O would not condense, while still cold enough to condense water from the N_2O.

The hot-copper gas purifier was used to prepare high purity N_2 and H_2 gas in the previous study on $TiO_2(001)$ surfaces [23]. In the case of N_2, contamination by O_2 and H_2 was eliminated, while for H_2, contamination by O_2 was removed. Removal of H_2 from N_2 is achieved as the heated copper/copper-oxide system oxidizes the hydrogen to form water

[93]. This water is then removed by condensation in the cold-trap. The chemical reactions responsible for H_2 removal are [94]:

$$2CuO(s) + H_2(g) \rightarrow Cu_2O(s) + H_2O(g) \tag{4.14}$$

$$Cu_2O(s) + H_2(g) \rightarrow 2Cu(s) + H_2O(g) \tag{4.15}$$

Where (s) and (g) are solid and gas phases respectively. These reactions lead to highly reduced copper surfaces, which can then separate oxygen from the parent gas [95] through re-oxidation. This re-oxidation at high temperature occurs according to the reactions

$$2Cu(s) + 0.5O_2(g) \rightarrow Cu_2O(s) \tag{4.16}$$

$$Cu_2O(s) + 0.5O_2(g) \rightarrow 2CuO(s). \tag{4.17}$$

These reactions also lead to the removal of O_2 from H_2.

This gas purifier is made from a 15-foot long copper tube of 1/4 inch diameter that has been coiled into a donut shape with a radius of about 3 inches. Two heating tapes controlled by variable-voltage transformers (Variacs) are wrapped around this donut. A mercury thermometer or thermocouple is used to monitor the temperature of the coil, which is to be maintained at 250°C. The volume of the purifier is 0.144 liters, and is inner reactive surface area is 910 cm^2. When this purifier is filled to a pressure of 760 T with N_2, it contains about $6x10^{20}$ nitrogen molecules. Regular grade gases may have part-per-million (ppm) impurity levels of oxygen. For N_2, we expect 5 ppm oxygen contamination. Thus there are $3x10^{15}$ oxygen molecules to be removed. Assuming that one monolayer ($\sim 10^{14}$ atoms/cm^2) of surface copper atoms are available to react with this oxygen, the number of copper atoms that can be oxidized in the purifier is about $9x10^{16}$. It takes two copper atoms to remove one oxygen atom. If we assume a 10% reaction efficiency, then about $5x10^{15}$ oxygen molecules can be removed in the purification process. This exceeds the number we need to react, so that N_2 processed in this way can be considered free of O_2 conatmination. A similar argument for removal of O_2 from H_2 leads to the same conclusion.

For the SHG experiments done here, the surface was exposed to O_2 and N_2O. Only the cold trap was used to purify the O_2 by removing residual water. Both the cold trap and hot-gas purifier were used for purification of medical grade N_2O, as described above,

with care taken not to cool the coils to the point where the N_2O would condense. The hot-copper purifier in this case helps to remove residual O_2 and H_2, and also to remove any NO (which is thermodynamically unstable). Any N_2 contamination is not of concern here, as it was previously demonstrated that TiO_2 surfaces do not react with N_2. NO_2 would be of concern if it were a major contaminant gas, but RGA analysis of the N_2O injected into the chamber shows that virtually no NO_2 is present. With these gases accounted for, reasonably pure N_2O is all that remains to be injected into the chamber. (For XPS studies, research grade N_2O was used, with similar results.)

4.2.6 Sample Preparation Techniques

The two samples used for these SHG studies are single crystal rutile $TiO_2(110)$ surfaces. High optical quality right-angle prisms are cut to so that their long edge is the (110) surface plane to be studied, and then subjected to a fine optical polish with submicron polishing powder. This results an optically smooth surface that is actually relatively rough from a microscopic viewpoint [25]. One prism is left in this rough state, and will be called the "polished" or "rough" surface for these discussions. The other was chemically etched to achieve regions that are comparatively flat and have single crystal morphology. This sample will be referred to as the "etched" or "smooth" surface. Chemical etching in fuming sulfuric acid has been shown to remove surface impurities and achieve better flatness on a microscopic scale than can be achieved by polishing alone. It has been reported that chemical etching produces nearly perfect single crystal surfaces [96], and this has been supported by recent STM studies [97]. In the etching recipe adopted here [25], one mechanically polished sample was placed crystal-face down in 98% pure sulfuric acid. The acid was then heated to 250°C for two hours, including a 30-minute heating and a 30-minute cooling period. After this chemical treatment, the sample was removed from the acid and rinsed in distilled and de-ionized water. Then the sample was dried in a dry nitrogen stream. Both the etched and the polished surfaces were then carefully washed in clean methanol before being mounted on the sample holder and placed in the vacuum chamber. In the vacuum chamber, the samples were heated to 150°C for at least 24 hours to remove any residual water or methanol.

4.2.7 A Typical SHG Experiment

A typical SHG experiment on a rutile $TiO_2(110)$ surface begins by sampling the SHG signal for a fully oxidized surface. Usually data are collected for five to ten minutes so that an SHG signal level can be established, and any noise characterized. Then the SHG signal detector is blocked, and the pump beam is turned on so that excitation UV at 266 nm impinges on the sample. This beam is left on the surface for several minutes, until the saturation fluence of 360 J/cm^2 [23] for defect production has been exceeded. (In most experiments, the UV is turned off at some point near the end of UV exposure and the SHG signal detector is briefly turned on to sample the SHG signal level. Then the detector is blocked, and the UV beam is again turned on. Comparison between this level and the final level allows confirmation that any observed change in the SHG signal has saturated.) The UV beam is then blocked, and the SHG signal detector is again turned on. If this signal level has changed from the starting level, an indication that defects have been generated on the surface, data are collected for five to ten minutes to establish a signal level for the reduced surface. If interactions between defects and a gas molecule are of interest, the gas in then slowly introduced into the chamber to the desired partial pressure while the SHG signal is continually monitored. If any changes in SHG signal result, the signal level is allowed to stabilize before any further changes are made. Then the interaction gas is pumped out of the chamber while the SHG signal continues to be measured. This allows continuous observation of the interaction between surface defects and gas molecules in both high and low pressure regimés.

4.3 X-ray Photoelectron Spectroscopy

X-ray Photoelectron Spectroscopy (XPS) and Ultraviolet Photoelectron Spectroscopy were also used to examine surfaces of rutile $TiO_2(110)$. (This work was done by myself at Pacific Northwest Laboratory in Richland WA. in collaboration with Donald R. Baer and Li-Qiong Wang.) These experiments were designed to parallel the SHG studies done on these surfaces, providing both confirmation of our interpretation of the SHG experiments and additional information through comparison with other XPS studies. The following

sections describe the equipment used at PNL, including any necessary variations between experiments done with XPS or UPS and those done using SHG.

XPS and UPS experiments were performed using a Physical Electronics PHI-560 multiprobe surface analysis system equipped with a double pass cylindrical mirror analyzer (CMA). Spectra are obtained by irradiating the surface in vacuum with either X-rays (XPS) or ultraviolet (UPS) photons and analyzing the electrons emitted from the surface as a consequence of the photoelectric effect. X-rays remove electrons from the core levels of atoms on the surface of the sample, while ultraviolet photons probe electrons in the valence levels of surface atoms. The CMA collects electrons ejected from the surface and sorts them by energy. A plot of the number of electrons collected per energy interval versus the electron kinetic energy constitutes the spectrum of the surface. Since each element has a unique spectrum, and the spectrum for a compound is roughly the sum of the spectra of the elements that make up the compound, the resulting spectrum for a surface provides insight into the composition and chemical state of the surface (see Section 3.5 which describes XPS as a surface science technique). Because electrons react strongly with matter, these studies must be done in UHV and only electrons from the top layers ($\sim$10's of Angstroms) of the sample will reach the detector.

In the following sections, the PHI-560 system and its UHV chamber will be examined in detail. Discussion begins with the vacuum system that contains the spectrometer, and then focuses on the geometry of the sample and the various transfer arms that allow the sample to be moved to and from the main chamber. Then photon sources are discussed, followed by an explanation of how photoelectrons are detected. Sample alignment and spectrometer calibration are then explained. Then methods for preparing single-crystal shoichiometric $TiO_2(110)$ surfaces in this chamber are presented. Finally, a typical XPS or UPS experiment is described.

4.3.1 XPS Ultra-high Vacuum System

Figure 4.5 shows a top view and Figure 4.6 a front view of the UHV system used for the photoelectron spectroscopy studies presented here. While the spectrometer components

are standard for the PHI-560 system, this chamber is custom-designed to allow samples to be introduced from atmosphere through a sample-introduction chamber (pump-down chamber) and also to be transferred from the main chamber to another side-chamber (reaction chamber) where *ex situ* reactions between samples and controlled environments can take place. The geometry of sample transfer to and from these side-chambers is discussed in the next section.

The UHV chamber, pump-down chamber and reaction chamber are pumped primarily using a mechanical pump and a turbo-molecular pump. The mechanical pump is installed at the base of the turbo pump, allowing it to pull through the turbo pump when the turbo pump is off, and to back the turbo pump when the turbo pump is on. These pumps are mounted at the base of the reaction chamber. Two valves and a stainless-steel flexible bellows connect the reaction chamber to the pump-down chamber, such that the turbo/mechanical pump combination can establish a vacuum in the pump-down chamber as well. The main chamber can also be opened to these pumps for roughing by opening the sample transfer valve between the reaction chamber and the main chamber. When evacuating the chamber from atmospheric pressure, the mechanical pump is first used to rough the entire system down to $1x10^{-3}$ T. Then the turbo-molecular pump is activated and pumps the system down to about $1x10^{-7}$ T. If the turbo pump is acting only on the reaction chamber or the pump-down chamber, pressures of about $1x10^{-8}$ T can be achieved ($1x10^{-9}$ T if these chambers are thoroughly baked). The sheer volume of the main chamber limits the pressure that can be quickly obtained by turbo-pumping alone.

The main chamber is attached to several other types of pumps that are used to help achieve and maintain ultra-high vacuum. The primary pump is an ion pump. Once the system pressure reaches $1x10^{-7}$ T using the turbo pump, the ion pump can be turned on. The system will then pump down to $1x10^{-8}$ T fairly rapidly, and to lower pressures with more time. A titanium sublimation pump is cycled during this pump-down to speed evacuation. A cryogenic pump is attached to the main chamber, though it is rarely used. These pumps have pumping speeds that vary for different residual gases that may be in the chamber. The addition of the titanium sublimation and cryogenic pumps provides a way to quickly remove residual gases that the ion pump does not efficiently remove. Without

Figure 4.5: Top view of the ultra-high vacuum system used for XPS/UPS experiments

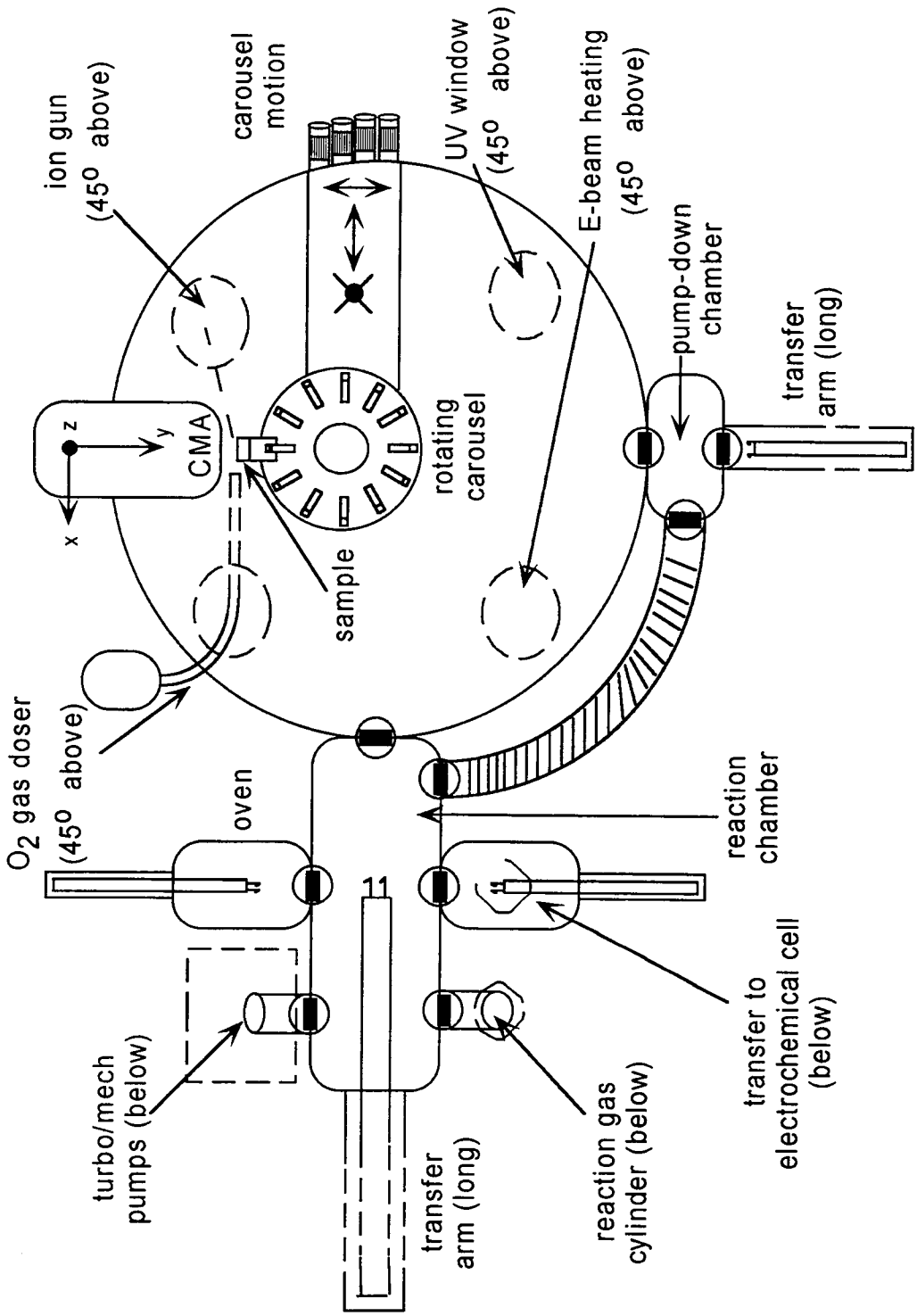

Figure 4.6: Front view of the ultra-high vacuum system used for XPS/UPS experiments

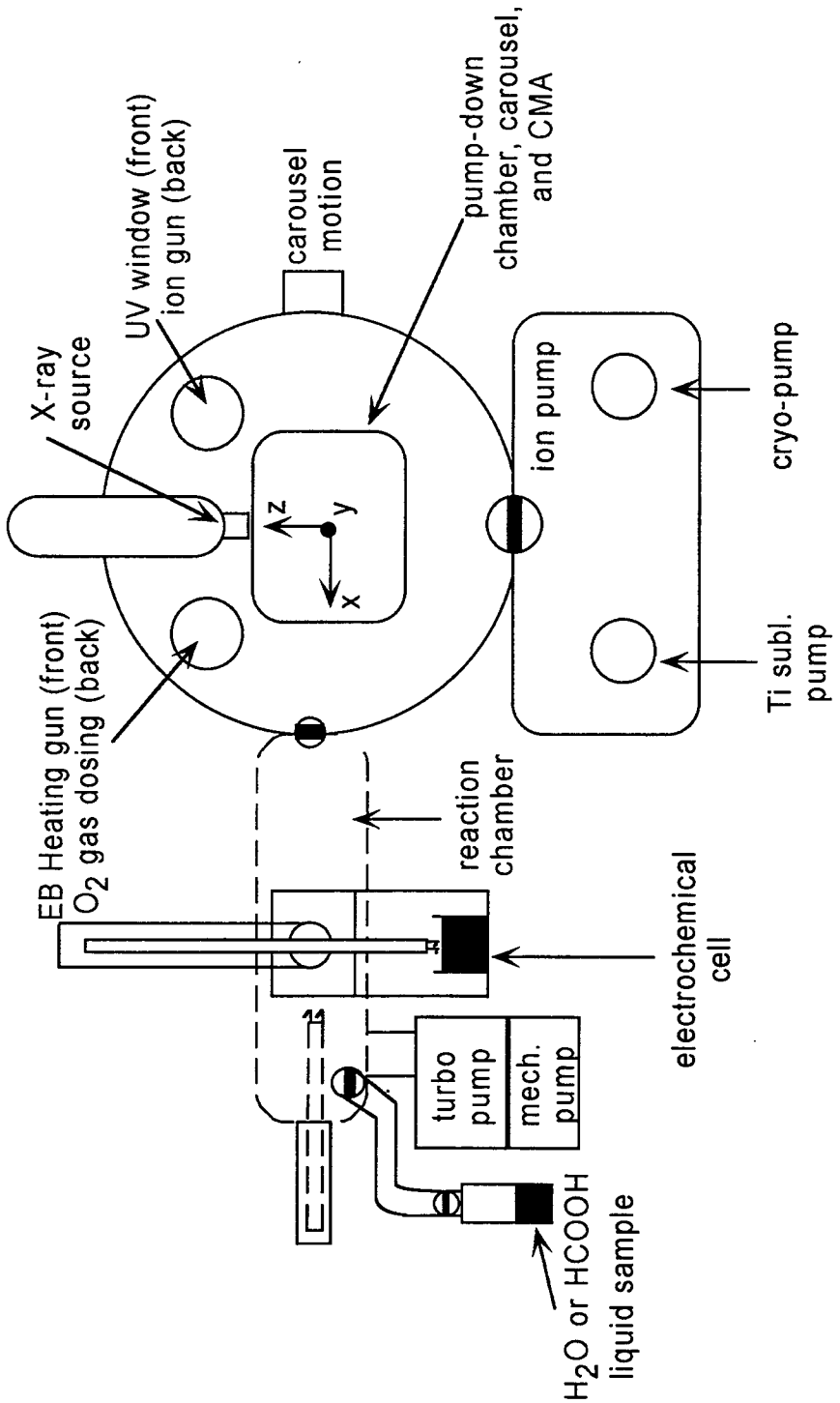

baking, these pumps in combination can achieve system pressures in the low 10^{-9} T region. This is the upper region of the "ultra-high" vacuum pressure range. When the system is baked, pressures as low as $1x10^{-10}$ can routinely be achieved. Baking involves heating the entire main chamber to over 150°C using radiant ovens placed at its base. When this is done, all electronic and water lines attached to the chamber must be removed to avoid damage. The chamber is typically baked for 8 hours into the ion pump, though longer baking cycles or baking into the turbo pump are prescribed when heavy contamination is present. Experiments done here always begin with a freshly baked chamber that contains only the TiO_2 sample to be studied and standard samples for spectrometer calibration. As with the SHG chamber, any gas doses that are subsequently done in the chamber necessarily raise this base pressure, usually to about $1x10^{-9}$ T. The very low base pressure then can not be reobtained without baking.

4.3.2 Sample Geometry and Transfer

The sample is mounted on a sample holder than can be placed on a rotating carousel that sits in front of the analyzer in the center of the main chamber. The sample carousel has 12 slots in which sample holders can be placed. It can be rotated such that each sample is placed in front of the analyzer in turn, and can also be translated in three dimensions, with one translation axis (y) along the axis of the CMA, and the others corresponding to motion in the left/right (x) and up/down (z) directions in front of the CMA. In the analysis position the sample faces the CMA, but the holder is tilted at a 60° angle with respect to the horizontal axis of the CMA. This tilt ensures that the ion beam used to sputter samples, described in Section 4.3.6.3, is incident normal to the sample surface. The sample holder has been specially designed so that it can be "grabbed" and removed from the carousel by either of two sample transfer rods that extend into the chamber from two side-chambers. Each side-chamber is isolated from the main chamber by a valve that is closed during experiments. When sample transfer becomes necessary one of these valves is opened, the sample transfer arm retrieves the sample from the carousel and takes it to

the side chamber, and the valve is again closed. This keeps main chamber exposure to the slightly higher pressures of either side-chamber to a minimum.

One side-chamber is the sample-introduction (pump-down) chamber where samples can be brought in from atmosphere and pumped down to UHV before being introduced to the main chamber and placed on the sample carousel. This side chamber is directly opposite the CMA such that the carousel must be rotated 180° (six carousel positions) to place an introduced sample in front of the analyzer. The second side-chamber is a reaction chamber where interactions between the sample and a controlled environment (such as a high partial-pressure of pure gas or a solution dip) can take place. This chamber is located parallel to the x-axis of the CMA, such that samples must be rotated 90° (three carousel positions) from the analysis position before being grabbed by the transfer arm and transferred to the reaction chamber.

In most of these experiments, the pump-down chamber is not used. The sample is mounted on the carousel when the main chamber is open to atmosphere. The system is then closed, pumped down, and baked. This is to keep the UHV environment as pristine as possible. Whenever a sample is brought in from atmosphere through the pump-down chamber, contaminants from the atmosphere are introduced to the main chamber. These are minimized by evacuating the pump-down chamber as much as possible. For routine studies aimed at determining the chemical composition of surfaces, this contamination is negligible. But for experiments where pristine single crystal surfaces are required, this contamination is measurable and unacceptable.

For many of these experiments, gas molecules are introduced into the main chamber through a capillary tube that has its outlet just above the sample. Here the partial pressure of these reaction gas is limited to $1x10^{-6}$ T so that the ion pump is not damaged. But this necessarily raises the base system pressure that can be reobtained without baking when the gas is pumped out. The alternative, for molecules that either are particularly difficult for the ion pump to remove or react strongly with the chamber walls, is to transfer the sample to the reaction chamber for the gas exposure. This minimizes exposure of the main chamber to the reaction gas. The reaction side-chamber is baked along with the main chamber to optimize vacuum conditions. But because it is only pumped by the turbo

pump, and is often exposed to highly reactive gases that adhere to the chamber walls, the reaction chamber must be considered as a source of contamination that can compromise the controlled environment of the experiment. To combat this, "blank" experiments where the sample is simply transferred to the reaction chamber and back with no gas dosing must be done to rule out chamber effects.

4.3.3 Photon Sources

X-rays used in XPS experiments were produced by a dual-anode (Mg/Al) Physical Electronics 04-500 X-ray source that was placed directly above the sample in the analysis position. This source is flange-mounted to the vacuum chamber and externally cooled by flowing tap water. Either Mg-K_α (1253.6 eV photon energy) or Al-K_α (1486.6 eV) X-rays could be selected, but the Mg anode was used exclusively during these experiments. The X-ray source consists of a filament that is placed next to pure samples of Mg (or Al). A high voltage (15 keV) is placed across the filament, causing a current (20 mA) to pass through it and resulting in the production of high energy electrons that boil off the filament and impinge on the Mg anode. These electrons excite or ionize core-level electrons in the anode, which emit characteristic X-rays as they transition back to the ground state. A thin (2 μm) aluminum window placed over then end of the X-ray source allows the X-rays to pass and impinge on the sample, but blocks any electrons from the filament from hitting the sample. These X-rays typically cover a 5 mm spot centered on the portion of the sample "seen" by the CMA. The power supplied to the X-ray filament can be varied from the 300 W setting described above. This setting was chosen because it provided enough X-rays to generate ample photoelectrons for good statistics, but not so many X-rays as to do damage to the sample. The height of the X-ray source could also be varied, providing more control over the number of X-rays striking the sample. Once a good signal level was established, the height of the X-ray source above the sample was recorded. This same height was used for all scans.

The UPS source (next to the ion gun, but not shown) irradiates the sample with 21.2 eV ultraviolet photons. To achieve this, He-I gas is first bled into the UPS source to about

$4x10^{-2}$ Torr where it also is allowed to back-fill the chamber to about $1x10^{-8}$ Torr. Since helium gas is inert, it does not interact with the sample or the chamber walls, and is easily pumped out of the chamber as needed. To generate the photons, a high voltage (3 kV) is placed across the gas discharge tube. This excites the helium atoms, which then emit 21.2 eV photons as they transition back to their ground state. The source is entirely closed except for a circular aperture that is aligned to point at the analysis position. The result is a "beam" of UV light that forms a spot on the sample about 4 mm in diameter. This spot must be carefully aligned to overlap the analysis region of the CMA so that the maximum number of photoelectrons possible are detected. (Note: In the experiments presented here, I show that 3.4 eV and 4.7 eV UV photons can create defects on TiO_2 surfaces. This raises some concern about doing UPS on these surfaces, in that it is possible that the 21.2 eV photons used for UPS could create defects as well. Such defect creation is not seen here however, because the flux of 21.2 eV photons from the UPS source is quite low. Several days of exposure to the UPS source would be required to match the total fluence of UV needed to saturate defect production using 3.4 eV or 4.7 eV photons.)

4.3.4 Detection of Photoelectrons

The heart of an XPS spectrometer is its electron analyzer. In the PHI-560 spectrometer a Perkin-Elmer 25-260AR Electron Energy Analyzer is employed to measure the energy spectrum of electrons emitted by a sample. This is an angle-resolved cylindrical mirror analyzer (CMA), a schematic of which is shown in Figure 4.7 [58]. Here electrons emitted by the surface enter the detector, where they are immediately retarded using a set of spherical retarding grids. The retardation voltage is set so that the energy of the electrons to be counted is fixed at a constant value, known as the pass energy. For example, with a pass energy of 100 eV, a retarding potential of 900 V is used when we want to count the number of 1000 eV electrons emitted by the surface. When a scan of the spectrum of electron energies is taken, the retarding potential is ramped step-by-step. Thus electrons at each energy in succession are retarded to 100 eV and sent to the CMA. This is necessary because the resolution of the CMA is strongly dependent on energy. For XPS, good resolution is

Figure 4.7: The Cylindrical Mirror Analyzer used to detect electrons in XPS and UPS experiments

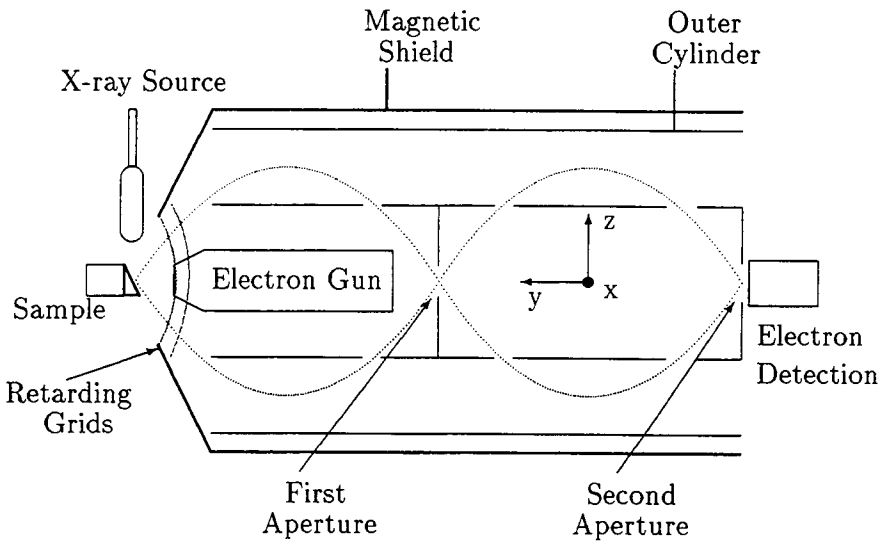

needed to separate closely-spaced peaks that arise from slight differences in the chemical state of an element. This resolution is much better for low electron energies, indicating that good resolution at all electron energies can be achieved if all the electrons are retarded to the same (low) energy before being sent to the CMA.

Once the electrons to be counted have been retarded to the pass energy, they are deflected through the path shown by placing an appropriate voltage on the outer cylinder of the analyzer. The slits are sufficiently narrow to exclude all electrons except those of the correct energy that come from a very small spot on the sample surface. The principle disadvantage of a CMA is that the detected electron energy is sensitive to the position of the sample in front of the analyzer. Electrons that come from a position 1 mm away from the optimal position in front of the analyzer can be shifted as much as 12 eV for 1000 eV electrons [58]. This degrades the resolution of the CMA unless only electrons from a very small region around the optimal analysis position are detected. Narrow apertures ensure exclusion of electrons from other areas, but at the expense of electron count rate. Electrons of the desired energy and from the correct location then make it through the CMA and are

detected using an electron multiplier. Under these optimum conditions, the resolution of the CMA is limited only by the natural linewidth of the X-ray source.

4.3.5 Sample Alignment and Spectrometer Calibration

The energy scale of the CMA is calibrated assuming that the sample is placed at a fixed distance from the entrance to the analyzer. This distance must be set for each sample studied, requiring that some reliable method of positioning the sample along the y-axis be employed. Such precise sample positioning is achieved using the electron gun that is directly in front of the sample in the analysis position. (This electron gun can also be used to do Auger spectroscopy on conducting samples.) To do this, the electron gun is set to emit 2 keV electrons which strike the sample. The CMA then detects the electrons that come off the sample, the majority of which are found in an elastic scattering peak at 2 keV. Once the CMA signal for the elastic peak has been located, the sample is translated toward the analyzer ($-y$ direction) until the CMA detects that the elastic peak is in the energy window centered at 2 keV. This ensures that every sample studied is placed in the same position in front of the analyzer, and that the CMA is roughly calibrated.

Additionally, the acceptance angle of the analyzer is such that only electrons that come from a roughly circular area about 1 mm across on a sample surface placed at this distance are counted. (The detection profile is roughly Gaussian, such that most of the electrons counted come from a much smaller area.) Since samples are typically much larger than this, careful positioning of the desired region of study in the xz-plane in front of the CMA is also necessary. The area of the sample to be analyzed is located by rastering across the sample using a low energy electron beam, collecting the resulting secondary electrons that are emitted from the sample surface, and constructing from the secondary electrons a focused image of the sample. This allows features on the sample surface to be identified, centered in the xz-plane in front of the analyzer, and located again if the sample is moved from the analysis position. The magnification of this image can be varied by changing the energy of electrons used. This allows the entire sample to be imaged first, followed by

expanded views of any surface features and precise selection of the portion of the sample surface to be studied.

The energy scale of the CMA is calibrated using XPS spectra from two highly-pure standard samples of Au and Cu that are kept on the sample carousels at all times. If the spectrometer is well calibrated, the Au 4f peak appears at 84.0 ev (±0.03 eV) and the Cu 2p-3/2 peak appears at 932.67 eV (±0.03 eV) [80]. This gives a high-energy and a low-energy peak at well-known energy to check the performance of the CMA. The positions of these peaks are checked prior to experiments, and periodically rechecked during long experiments.

4.3.6 XPS Sample Preparation

In early experiments, where XPS studies were performed to directly confirm SHG results, etched $TiO_2(110)$ samples (see section 4.2.6) from SHG experiments were exclusively used. But these samples were heavily carbon contaminated from handling in transfer from the SHG chamber to the XPS chamber. This carbon contamination could be greatly reduced by exposing the surface to UV light in an O_2 environment, but could never be entirely removed. This led to the study of oxygen-annealed single crystal $TiO_2(110)$ surfaces that could be sputter-cleaned and re-formed as needed. Such surfaces are the standard in the UHV industry, and are generally considered to be the "best" (most defect-free) single crystal surfaces producable. Many defect characterization studies have already been done on surfaces prepared in this way [29], providing valuable comparisons for the studies presented here. Once it has been established that etched surfaces and annealed surfaces are equivalent, behavior observed in studies done on one type of surface can be expected to occur on the other. Defect-free surfaces used in XPS studies are prepared by thermally annealing a clean surface of TiO_2 in an O_2 environment. The following sections discuss how this is achieved.

4.3.6.1 The Sample as Received

An 8x8x1 mm wafer of single crystal rutile TiO_2 is obtained from Princeton Scientific. This wafer is cut to expose the (110) surface and subjected to fine mechanical polishing until optically flat. The sample as received is sonicated in methanol, dried in dry N_2, mounted on the sample holder, and then placed in the vacuum chamber. After the vacuum chamber has been baked to establish pristine UHV conditions, the sample is heated in vacuum to ~600°C for several hours. This reduces the bulk material, which is necessary to minimize charging effects that shift XPS and UPS peaks (see Section 5.2.2.2). Reduction is complete when the sample has changed color from its usual transparent yellow to a nearly opaque blue.

4.3.6.2 Heating the Sample

Two different systems have been used for sample heating, depending on the experiments to be done. If gas dosing can be done in the main chamber such that the sample need not be moved, resistive heating is employed. Then the sample is mounted by coating the back of the sample with a thin gold film and clipping it to a tantalum foil holder. The Au film makes good thermal contact between the sample and the holder. Thin grooves are cut in the sides of the sample, allowing thin "clips" of tantalum to be formed by folding a thin foil of tantalum around the back of the sample. This holds the sample without having any of the Ta cover the sample surface. A diagram of this mounting system is shown in Figure 4.8. Copper leads can then be spot-welded to the Ta foil and passed through electrical feed-throughs to the outside of the UHV chamber. As current passes through the resulting circuit, the Ta foil and the sample are heated. A thermocouple inserted between the sample and the Ta foil provides a rough temperature reading for the sample.

If the sample is to undergo reactions with gases that can not be done in the main chamber, resistive heating can not be used. This is because no permanent leads can be attached to the sample if it is to be taken off the sample carousel and transferred to a side-chamber for reactions. In this case, electron-bombardment (EB) heating is substituted.

Figure 4.8: Method of mounting the $TiO_2(110)$ sample for XPS

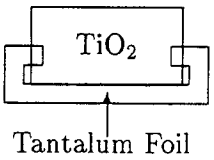

This form of heating is much more crude than resistive heating, and must be done carefully to prevent overheating and sample fracture. In EB-heating, the Au film is omitted. The sample is clipped directly to the Ta foil backing, and then the Ta backing is spot-welded to a stainless steel wire. This wire is bent and screwed to a standard sample holder used in the PHI-560 system. (This geometry is also preferred when samples are to be dipped in solution for electrochemical studies.) An additional electron gun is then mounted in the main chamber in the space between the pump-down chamber and the reaction chamber. This gun is aligned so that it directs a stream of electrons onto the sample when the sample is fixed directly in front of it. The sample must be rotated 4.5 slots from the analysis position to be placed in this position. The electron gun is then set to emit 1 keV electrons with a 5 mA emission current. These electrons strike the grounded sample in sufficient numbers to cause heating. The sample must be carefully placed to ensure that uniform heating takes place. If the electron beam is too focused on the sample, localized heating will occur that may cause the sample to fracture. In addition, heating must be done slowly and constantly monitored. If the sample is overheated it may fracture as well. In EB-heating, sample temperature is determined roughly by observing the color of the sample. At 600°C, the sample will begin to glow faintly red. At any higher temperature, the sample will glow more brightly and more orange. Clearly EB-heating is less controlled and less reproducible than resistive heating. It remains, however, the only practical method of heating when sample transfer is required.

4.3.6.3 Argon Ion Sputtering

Contamination from surfaces in UHV is typically removed by noble gas ion bombardment. Here argon ions (Ar^+) with energies between 500 eV and 5 keV with current densities on the order of 1 $\mu A/cm^2$ are directed at the sample surface. These ions collide with surface atoms and clusters, exchanging energy in the process, usually resulting in the ejection of these atoms and clusters. Thus the ions erode material from the surface in a process known as sputtering. Thick layers of contamination can be easily removed in this way, as can surface layers of the material beneath. Sputtering rates vary from material to material, and differential sputtering, where one species is eroded off a surface faster than other species, is common. On $TiO_2(110)$ surfaces, oxygen is preferentially sputtered such that surfaces that have been argon bombarded have large numbers of oxygen vacancy defects. These show up in XPS spectra as Ti^{3+}, Ti^{2+} and Ti^{0+} defect peaks in the titanium spectrum. In addition, sputtering causes damage deep into the material surface, such that the surface after sputtering has electronic defects that extend well into the material below the topmost surface layer. The topmost surface defects can be healed by oxygen exposure, but the deep defects remain [29]. In general, a surface that has been sputtered will be much more topographically complex than it was previously. For these reasons, excessive sputtering should be avoided, and topography studies should be done before and after sample treatment to establish that no gross changes is sample morphology have occurred as a consequence of sputtering. Once the $TiO_2(110)$ samples to be studied here have been reduced, they are gently sputtered using 1 keV Ar^+ until no residual contamination by carbon and other common contaminants remains. The clean, but damaged, sample that results can then be thermally annealed to produce a defect-free surface.

4.3.6.4 Thermal Annealing

It has been demonstrated that heating a sputtered $TiO_2(110)$ sample to 600°C in an oxygen ($1x10^{-6}$ T partial pressure) environment re-orders the surface to produce a (1x1) LEED pattern [18, 22, 26] and a stoichiometric surface with no observed defects using XPS

[30] or UPS [18, 22]. Processing in this way is referred to as "annealing" the sample, and it produces what is considered by the industry to be the best single-crystal surface achievable. If the sample is heated in the absence of oxygen, the (1x1) LEED pattern is restored, but a small number of Ti^{3+} defects remain [29]. Here freshly sputtered samples are annealed by heating to 600°C in $1x10^{-6}$ T O_2 for 10 minutes and then cooling to room temperature in this same oxygen environment. The cycle of sputtering and annealing can be repeated indefinitely for these samples, resulting in a reproducible defect-free surface for study.

4.3.6.5 Intentional Creation of Surface Ti^{3+} Defects

Three ways of producing defects on $TiO_2(110)$ surfaces will be compared in this thesis. As previously mentioned, it has been well established that argon ion sputtering heavily damages these surfaces, resulting in an oxygen-deficient surface with defects of several types (Ti^{3+}, Ti^{2+} and Ti^{0+}). The final number of defects produced can be varied by altering the energy of the incident sputtering ions or changing the duration of the exposure. As expected, increasing ion energy or time of ion exposure will result in more damage. Less severe damage can be done by exposing the surface to low-energy electrons. When this is done the resulting surface defects are limited to the surface region and of Ti^{3+} type only [29]. Electron-beam damage, however, does not increase with exposure in the same way that Ar^+-ion damage does. Instead, electron-beam defects are readily created up until a certain number of defects are present. Once this number has been reached, further exposure creates defects only very slowly. This "saturation" region can be reached by exposing the surface to 1 keV electrons for 30 minutes. An additional 2 hours of exposure at this energy are needed before any appreciable damage beyond this point is seen.

This thesis will demonstrate that exposing $TiO_2(110)$ surfaces to above band-gap UV light will also create defects. It is useful to compare spectra for the UV-damaged surfaces to spectra for electron beam-damaged and Ar^+-ion beam-damaged surfaces to characterize the damage the UV light does. The surfaces damaged by sputtering that are used for comparison were taken after exposing the surface to a 1 keV Ar^+ beam for 10 minutes.

This produces roughly the same amount of damage each time it is done on a clean, defect-free surface. Comparison spectra for electron-beam damaged surfaces are taken after the surface has been exposed to 1 keV electrons for 30 minutes, such that the saturation region has been reached. The electron source used to do this damage is the electron gun that is directly in front of the sample in the analysis position. During damage the sample is biased to attract the electrons, resulting in 10 μA of electron-beam current passing through the sample.

4.3.7 A Typical XPS or UPS Experiment

In a typical XPS experiment, a defect-free surface is produced by thermal annealing as described above. For XPS studies, a survey scan (100 eV pass energy) confirms that no contamination remains on the surface, and then a high resolution mulitplex scan (25 eV pass energy) is taken of the Ti-2p doublet and the 0-1s peak. Then the surface is intentionally damaged using either UV photons, low-energy electrons, or argon ions. The damaged surface is then surveyed and multiplexed. An overlap of the Ti-2p multiplexes for the damaged and defect-free surfaces will show how much damage was done. Then gas is introduced to the main chamber to react with the surface, or the sample is transferred to the reaction chamber for gas exposure, and the resulting surface is again surveyed and multiplexed. An overlap of the Ti-2p multiplexes for all three surfaces will then show how the defects respond to the gas molecules. For UPS studies, the procedure is the same, except that electrons are collected following their ejection from the 21.2 eV He I UV source. The resulting spectra for each surface treatment can are then overlapped for comparison.

CHAPTER 5
EXPERIMENTAL RESULTS

5.1 Previous Research on (001) TiO_2 and Overview of (110) TiO_2 Studies Presented Here

The work in this thesis is a direct continuation of Ph.D. research done by Winyann Jang and Chang-Juan Ju in this group on TiO_2(001) surfaces [23, 78]. In their research, Dr.'s Jang and Ju used second harmonic generation to monitor changes in electronic structure and symmetry for surfaces that were prepared by two different methods (mechanical polishing and chemical etching, as discussed in Section 4.2.6). The most substantial observation made in the (001) surface research was that exposing these surfaces to above band-gap UV light appeared to result in the creation of surface defects. These defects could be created on samples with both types of surface preparation. For SHG experiments using 532 nm doubled Nd:YAG laser light, this defect creation appeared as a change in the second harmonic intensity after UV exposure. The change saturated after 360 J/cm^2 total fluence of UV, and could be reversed by exposing the sample to O_2 gas, suggesting that the UV light created surface oxygen vacancies. Spectroscopic studies using tunable dye lasers showed that a change in electronic structure did occur after UV exposure, and that this change was consistent with production of Ti^{3+} defects. Independent confirmation of the type of defects and determination of their number was not possible in this early research.

Following the observation of UV defect-creation, research focused on characterizing interactions between these defects and small molecules. These included O_2, N_2, H_2, and H_2O. The TiO_2(001) surface, both before and after defect production, was found to be inert to N_2 and H_2. When the (001) surface was exposed to water vapor, a very small change in SHG signal was observed as long was the water vapor was present in the chamber. This change was reversed when the water vapor was evacuated. These results were consistent on both polished and etched samples, and led to the conclusion that defects on these surfaces do not react strongly with these three molecules. Reactions with O_2 served as a contrast to this behavior. When surfaces with UV-induced defects were exposed to even a small amount of O_2, the change induced by UV was removed and the SHG signal returned to its

pre-UV level. The process of UV-production and O_2-healing of defects could be repeated indefinitely. Since adsorption of O_2 as O_2^- on TiO_2 surfaces had been reported previously (see Section 2.4.1), the original interpretation of these observations was that O_2 was bound to a defect to produce a Ti^{4+}:O_2^- complex. The UV light was simply destroying these complexes by creating a bulk electron-hole pair, with the hole migrating to the surface to recombine with the bonding electron responsible for the complex. The O_2 would then desorb, and an electron from the bulk would be trapped at the uncoordinated Ti^{4+} ion remaining behind to form a Ti^{3+} defect.

UV creation and O_2 healing of defects were observed both on polished and etched (001) surfaces. In addition, a high-pressure species of O_2 was seen on the polished surface when the O_2 pressure was increased to above 5 Torr (T). No such species was seen on the etched surface. This species was determined to be physisorbed O_2, and a large portion of Dr. Jang's thesis was devoted to exploring the dynamics of this physisorption.

The first experiments presented here mirror Dr. Jang's experiments but for the TiO_2(110) surface. These experiments were done jointly by Dr. Jang and myself, and some of them can be found in his thesis. The remainder of the experiments were done by myself following Dr. Jang's departure from the group. These include XPS studies to confirm that the UV defects created are of Ti^{3+} type and to determine their number. This is followed by studies of interactions between defects and three additional molecules. XPS and UPS were used to study H_2O-defect interactions and HCOOH-defect interactions, and a combination of XPS and SHG was then used to characterize N_2O-defect interactions.

5.2 Defect Creation and Interactions between Defects and O_2

5.2.1 SHG Observation of UV-Creation and O_2-Healing of Defects on (110) TiO_2 Surfaces

5.2.1.1 Overall Behavior on Etched and Polished Surfaces

Typical cycles of UV defect creation and O_2 defect healing for etched and polished surfaces of TiO_2(110) are shown in Figures 5.1 and 5.2 respectively. A brief description of such cycles was included in Section 4.2.7, but will be reproduced here in more experimental

detail. For each cycle shown, SHG signal is monitored as a function of time while changes are made to the surface. Here the input field is p-polarized for the experiment on the etched surface, and s-polarized for the polished surface. The reason for this difference is fully discussed in the next section (see Section 5.2.1.2), as is the meaning of the measured signal levels for each experiment.

The first flat region in each graph is the SHG signal for the surface before any treatment. Then the UV is directed onto each sample. During UV irradiation, no SHG signal can be measured. This is because a large amount of scattered UV from the pump beam necessarily reaches the detector, swamping any SHG signal in an enormous background. To increase the lifetime of the photomultiplier tube, the SHG detection system is shuttered during UV exposure. After sufficient UV exposure to create and saturate any changes in SHG signal (see Section 4.2.7) has been applied, the UV is turned off, and SHG signal is again monitored. This establishes a baseline for the signal level of a surface with UV-induced defects. Then O_2 gas is slowly bled into the chamber through the gas introduction line (see Section 4.2.5.2). For both surfaces, O_2 exposure results in the rapid restoration of the SHG signal to its pre-UV level. On the etched surface, increasing the O_2 partial pressure in the chamber into the Torr regimé did not produce any additional changes. But for the polished sample, SHG signal began to rise after an O_2 partial pressure of 5 Torr (T) was reached. This increase in signal continued until an O_2 pressure of 100 T was reached, where the signal level stabilized. If the O_2 was then pumped out of the chamber, the SHG signal slowly decreased to its previous level. This shows that there is an O_2 species reversibly adsorbed on the polished surface at high pressure.

This behavior, for both types of surface preparation, correlates well with the behavior observed on the (001) surface [23]. Again both etched and polished surfaces undergo changes in their electronic or physical structure when exposed to UV light, and these changes can be reversed by O_2 exposure. The high-pressure physisorption on the polished surface is also present. Similar arguments as were used on the (001) surface lead again to the conclusion that the UV light is breaking apart Ti^{4+}:O_2^- complexes that form on the surface when O_2 interacts with a Ti^{3+} defect.

Figure 5.1: SHG observation ($I_{total,p}$) of UV-creation and O_2-healing of defects on etched (110) TiO_2

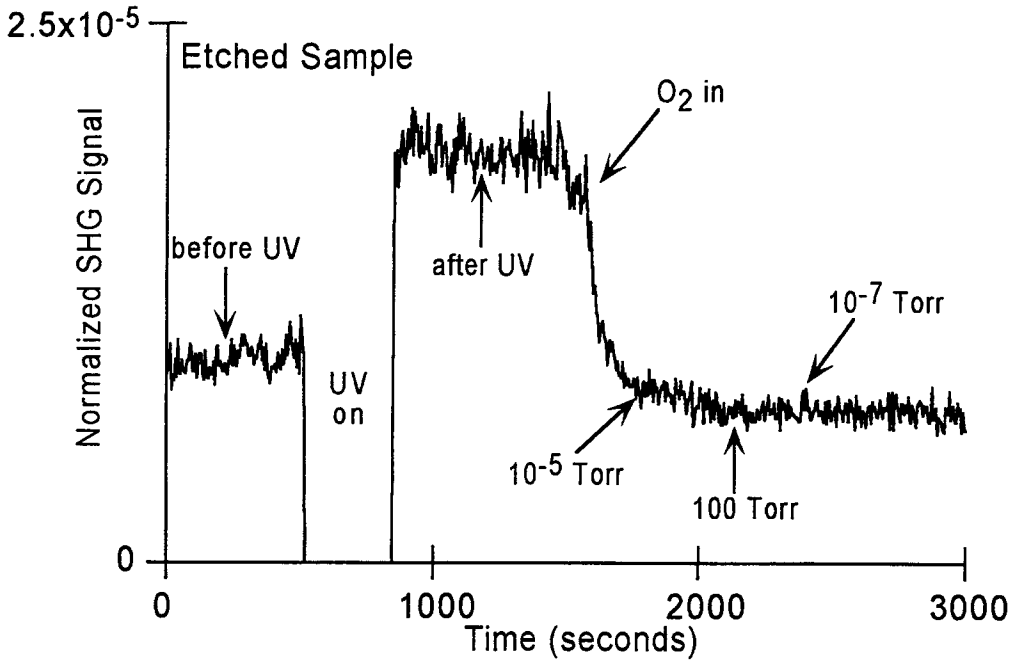

Figure 5.2: SHG observation ($I_{total,s}$) of UV-creation and O_2-healing of defects on polished (110) TiO_2

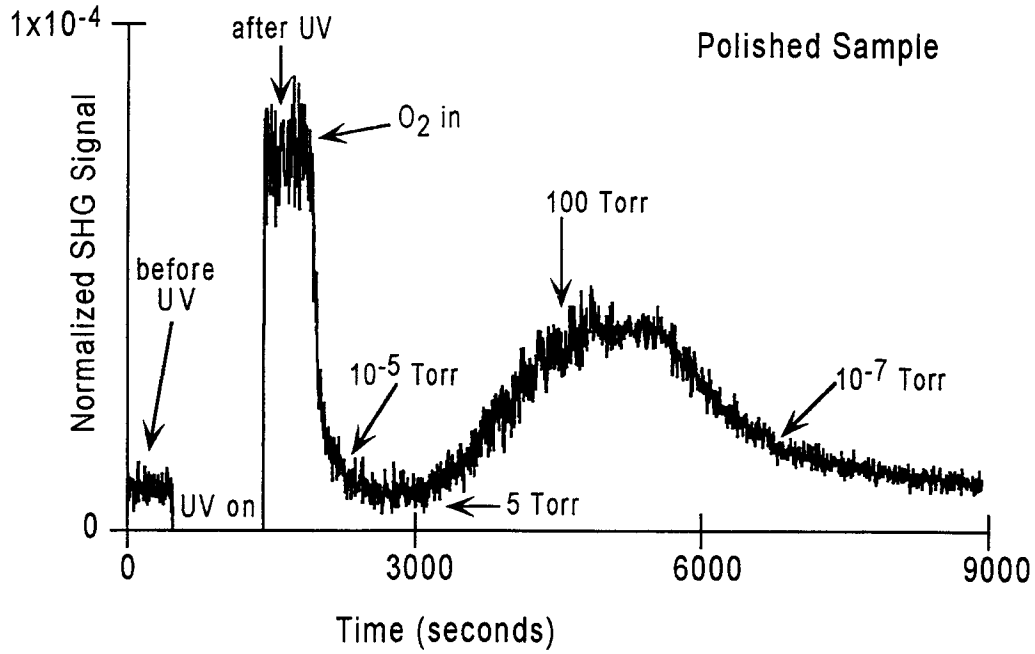

Figure 5.3: SHG cycle ($I_{total,p}$) on polished (110) TiO_2

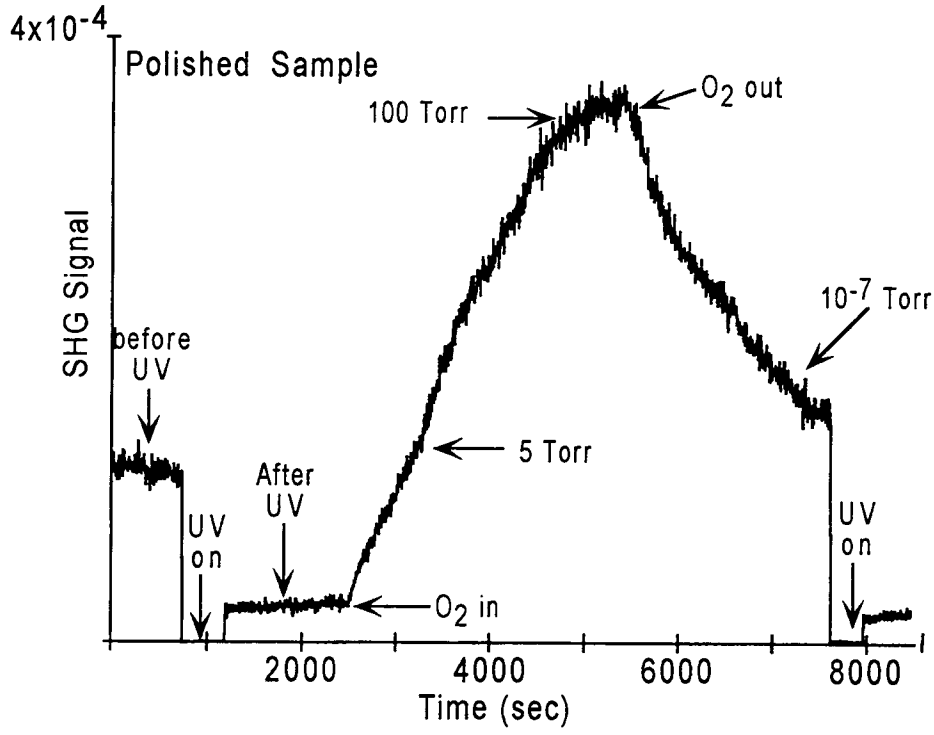

5.2.1.2 More Detailed Comparisons

Comparison of Figures 5.1 and 5.2 seems to indicate a great similarity between the etched and polished surfaces. This similarity is actually not as strong as the data suggest. The SHG signal for the etched surface was generated by using a p-polarized probe beam and collecting light with all possible polarizations as output. Thus the intensity measured is $I_{out,in}=I_{tot,p}$, using the convention of Table 3.1. But the cycle shown for the polished surface was generated by using an s-polarized probe beam and collecting all polarizations of output, so that $I_{tot,s}$ was instead measured. Similar polarization experiments for these two surfaces were not compared because for the polished surface using p-polarization did not allow resolution of the physisorbed high-pressure species from the low-pressure defect-healing species. A cycle for measurement of $I_{tot,p}$ on the polished (110) surface is shown in Figure 5.3. Here the initial signal from the sample before UV exposure is high, and UV exposure causes it to drop. Exposure to O_2 at low pressure causes the signal level to begin

to return to its pre-UV level, but increasing the O_2 pressure causes the signal to continue to rise until the level saturates at 100 T O_2. Pumping out the oxygen causes the signal to slowly return to the pre-UV level. In this figure, before the pre-UV level was again reached additional UV was applied to show that the signal would drop to the expected low level. Since both UV-defect healing and the high-pressure physisorption lead to a rise in SHG signal under these polarization conditions, it becomes difficult to separate the contribution to the signal from each process. For the $I_{tot,s}$ experiment, however, defect healing causes a drop in signal while the high-pressure physisorption causes an increase. This allows for unambiguous separation of the two effects.

In addition, SHG signal levels for the polished surface were in general much stronger than those for the etched surface. The SHG signal scale used in all SHG figures has arbitrary units. To obtain the numbers used on this scale, the integrated output of the PMT is divided by the square of the output voltage read by the reference pin-diode. The reference voltage depends on the optical alignment of the pin-diode with respect to the portion of the beam it measures, and is not an accurate measure of laser power. This normalization scheme is designed to eliminate noise that arises due to fluctuations of the laser within a given experiment. But over the course of many experiments, this can not be relied upon to provide stable normalization that would allow signal levels for different experiments to be compared. Such comparisons are instead made by recording the absolute SHG signal level achieved for a given input power. For 35 mW input probe power, signals from the polished surface are always at least double those for the etched surface. This is thought to be a consequence of the increased surface area available on the polished surface, which is more topographically complex than the etched surface [25].

For the above experiments, the UHV system base-pressure was below $1x10^{-8}$ T. The RGA attached to the chamber further indicated that the partial pressure of O_2 in the chamber was less than $1x10^{-10}$ T. This means that when O_2 is bled into the chamber, the partial pressure of this oxygen is varied from $1x10^{-10}$ T to 100 T. SHG signal for surfaces after UV exposure remains constant if the sample is left in UHV with no intentional gas exposure. This indicates that UV-induced defects do not react with contaminant molecules

Table 5.1: Relative SHG signal measured under different polarization conditions for etched and polished (110) TiO_2 surfaces

polarization condition(out,in)	etched surface before UV	etched surface after UV	polished surface before UV	polished surface after UV
ss	4 (±2)	4 (±2)	2 (±1)	4 (±2)
ps	13	33	4	20
sp	4 (±2)	4 (±2)	38	4 (±2)
pp	71	108	162	20
total,s	19	42	7	27
total,p	75	115	200	23

in the vacuum over the course of an experiment. In addition, O_2 healing is not observed on the UV-damaged surface at a noticable rate until a partial pressure of $1x10^{-6}$ T is reached.

5.2.1.3 Surface Symmetries

As discussed previously, specific polarization experiments can provide information about the symmetry of surfaces studied. Table 5.1 shows the relative SHG signal for etched and polished (110) surfaces both before and after UV exposure. Bulk TiO_2 has D_{4h} symmetry, and an ideal (110) surface should have C_{2v} symmetry. From Table 3.1, this means that both I_{ss} and I_{sp} should be zero, and only I_{ps} and I_{pp} should be present. From Table 5.1 it is clear that the etched TiO_2(110) surface follows this pattern, indicating that it closely matches the symmetry of an ideal surface. This overall symmetry is retained when the surface is exposed to UV, but the non-zero tensor elements of $\tilde{\chi}^{(2)}$ change slightly. In contrast, the rough surface does not follow the expected pattern for a surface of ideal symmetry, indicating that it has more complicated topography. It is also important to note that the symmetry pattern observed for the (110) surface is consistent with both C_{2v} and C_{4v} symmetries. This is an artifact of the geometry chosen for sample analysis. If rotation about the sample z-axis was possible, the symmetry of these surfaces before and after UV exposure could be uniquely determined. Clearly there is much information that

can be gained by doing complete polarization experiments on these samples. Adding sample rotation capabilities is thus a high priority for future studies.

5.2.1.4 Photodynamics of the High Pressure Species

The photodynamics of the high-pressure reversibly adsorbed O_2 species on the polished (001) surface were extensively studied previously [23]. It was found that the physisorbed species could be forced off the surface using a brief UV exposure, even if the sample was in 100 T O_2. This allowed readsorption dynamics of this species to be studied. A typical experiment of this type involves irradiating the sample with UV for a short time, and then monitoring the SHG signal from the surface for 90 seconds after the UV has been removed. The SHG signal is integrated every 2 ms, and 10 such shots are averaged for every data point. (In contrast, when long SHG experiments like those presented in the first three figures are done, 2000 shots are averaged to make one data point.) Multiple 90 second runs are then averaged to minimize noise. The result is that changes in SHG signal that occur over several seconds can be observed.

The motivation for such experiments was the hope that the defect healing process could be observed. To this end, the (001) etched surface was irradiated with UV in a low partial pressure ($1x10^{-5}$ T) of O_2 for 180 seconds, and then 90 second scans of the surface with defects were taken. But even at this low oxygen pressure, defect healing by O_2 happened too quickly to be detected. This indicated that there was little hope of observing the photodynamics of the UV defect creation and O_2 defect healing processes. But doing the same experiment on the polished (001) sample at high pressure did show re-adsorption of the high-pressure species. Here a one second burst of UV removed a number of the physisorbed species, resulting in a lower SHG signal immediately following the exposure. This signal returned to the pre-UV level over several seconds as the physisorbed species returned to the surface. Similar exposure to the etched (001) sample at high pressure produce no such change, confirming that only the high-pressure species was involved.

A similar study on polished and etched (110) surfaces produced similar results. Here 90-second scans of SHG signal in 100 T O_2 for polished and etched (110) surfaces after

1 second UV exposures are shown in Figure 5.4. No re-adsorption is seen on the etched sample, as expected considering no high-pressure species was seen on this surface. But for the polished sample, SHG signal following UV exposure increases, indicating return of the high-pressure species. Figure 5.5 shows a similar scan done in air, with similar results. In air, it is clear that the physisorbed species returns much more quickly after UV exposure than was observed in the pure oxygen environment. Figure 5.4 shows that the SHG signal in O_2 has not entirely leveled off even after 90 seconds, though most of the re-adsorption is complete after about 15 seconds. This indicates that other adsorbates in air, most notably water, may complicate the re-adsorption process.

These studies show that exposure to UV in UHV changes the electronic or physical structure of $TiO_2(110)$ surfaces. This change can be reversed if surfaces are exposed to low partial pressures of O_2 gas. All evidence, including spectroscopic studies on the (001) surface [23], suggest that this change takes the form of creation of Ti^{3+} defects which are then healed by O_2 exposure. Past studies which have observed intact adsorption of O_2 on these surfaces [30] suggest that healing may occur through a charge-transfer that forms a Ti^{4+}:O_2^- complex out of a defect and an O_2 molecule. But it is also possible that O_2 dissociates such that the defect is healed by the O^{2-} ion necessary to form a stoichiometric, defect-free surface. The barrier to such a dissociation is quite large ($\sim$5 eV for O_2 and 3.5 eV for O_2^- [98]), however, suggesting dissociation is unlikely. The second explanation would also require that some mechanism exist by which UV light could create defects on a stoichiometric surface. Since these surfaces are very stable, this is also thought to be unlikely.

5.2.2 XPS Observation of UV-Creation and O_2-Healing of Defects on (110) TiO_2 Surfaces

There are a few limitations to the SHG experiments done here that prevent more definite conclusions from being drawn. First, there has been no direct confirmation of the type of defects being produced by UV exposure. Spectroscopic data on the (001) surface are consistent with Ti^{3+} defects, but do not provide conclusive proof. Second, SHG provides

Figure 5.4: Re-adsorption of the high-pressure O_2 species in 100 Torr O_2 on the polished surface after UV exposure

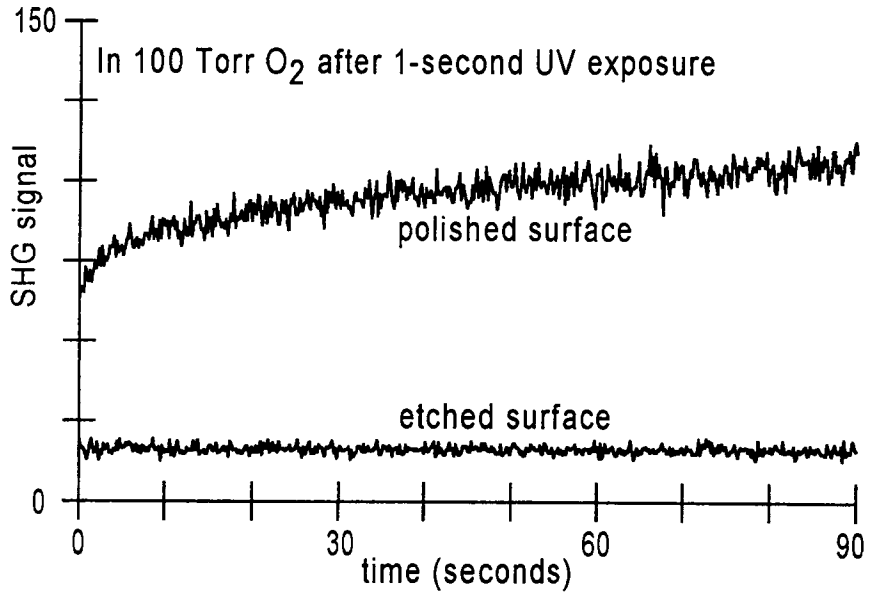

Figure 5.5: Re-adsorption of the high-pressure O_2 species in air on the polished surface after UV exposure

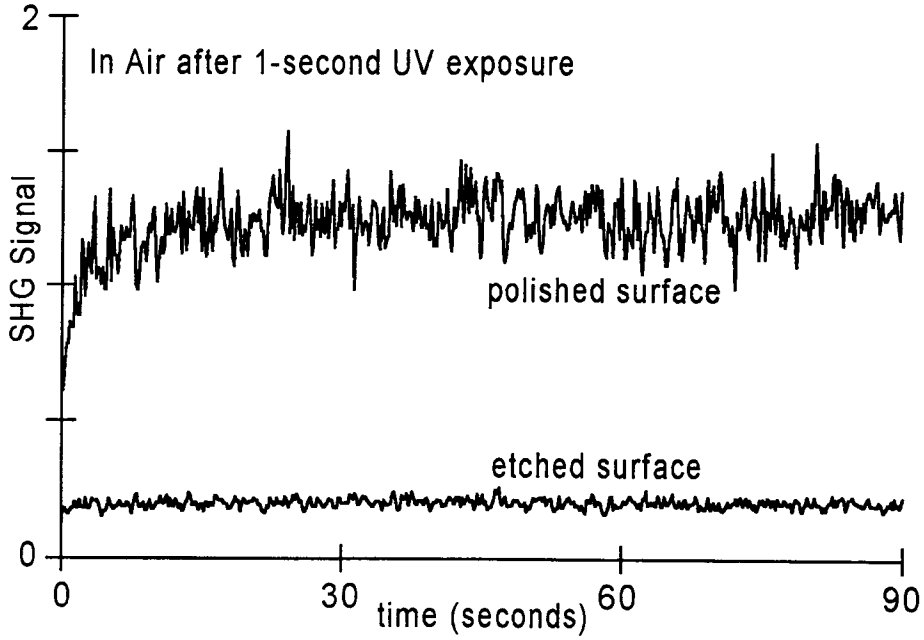

no way to estimate the number of defects created, so that a density of Ti^{4+}:O_2^- complexes on these surfaces can be obtained. Third, studies done here are on surfaces that are not yet well-characterized. Many would argue that the UV response observed here is occurring only at steps on our surfaces. Others suggest that hydrocarbon contamination on these surfaces is leading to UV-assisted desorption of CO or CO_2, though the ability to repeat the UV defect-creation and O_2 defect healing cycle indefinitely argues against this. Since the UHV chamber used for SHG studies is not equipped with conventional surface science probes for chemical analysis, these limitations are difficult to address. For this reason, parallel studies were done on these surfaces using XPS. The results of these studies provide answers to the three above concerns. In addition, identical UV-defect creation studies were done on well-characterized single-crystal, UHV-prepared surfaces. These samples were argon-sputtered to remove all contamination, annealed in O_2 at 600°C to generate a stoichiometric (1x1) surface, and scanned using XPS and UPS to ensure that no defects are present (see Section 4.3.6). Comparing the behavior observed on our etched and polished samples to that seen on samples prepared by means accepted by the UHV industry lends credence to our observations. In addition, studies that characterize defect type and number for defects produced by other means have been done on surfaces prepared in this way, allowing UV-produced defects to be quantified.

XPS studies were done at Pacific Northwest Laboratory, using a PHI-560 spectrometer as detailed in Section 4.3. The lab at PNL was not equipped to allow lasers to be used for UV exposure, so a mercury arc-lamp was used instead. This arc-lamp produced 1.7 Watts of UV at 365 nm, focused 7 cm in front of the lamp. This light was collimated and directed onto the sample in the UHV chamber through a fused silica window. The ultimate UV power density reaching the sample was small ($\approx$50 mW/cm^2 on average) compared to that achieved using the SHG pump beam ($\approx$800 kW/cm^2 pulsed), requiring much longer exposure times to produce defects for XPS observation.

Figure 5.6: XPS observation of UV-creation and O_2-healing of defects on etched (110) TiO_2

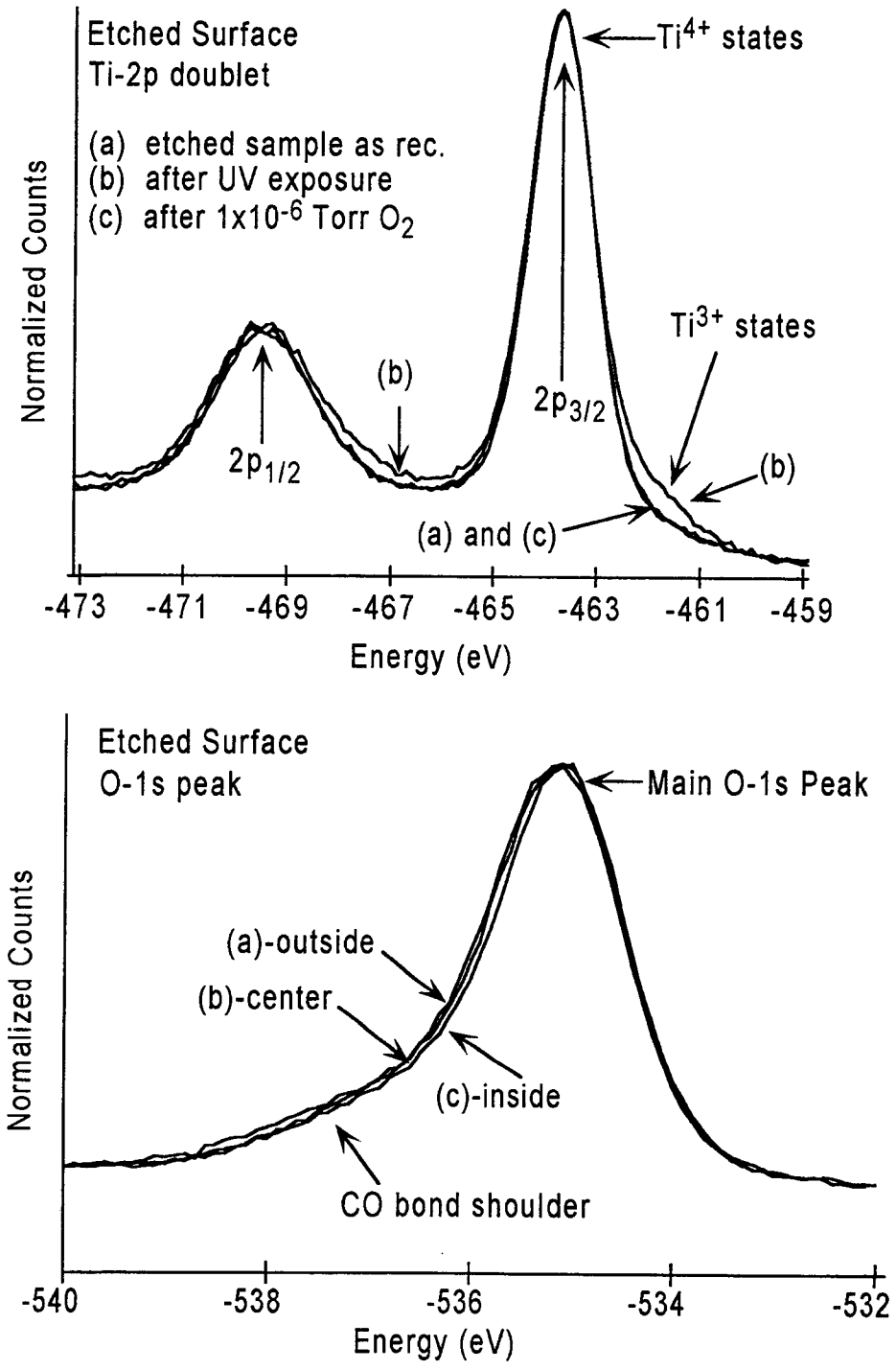

5.2.2.1 Overall Behavior on the Etched (110) TiO_2 Surface

Figure 5.6 shows the result of a typical experiment done on the etched surface using XPS as a surface probe (see Section 4.3.7). A high-resolution XPS scan is taken of the Ti-2p doublet and the O-1s singlet photopeaks for this sample before any treatment. Here the pass energy of the scan is 25 eV, and a data point is taken every 0.1 eV. The resulting lineshapes are taken to be the baseline "defect-free" lineshapes, against which all other spectra are compared. These are shown as curve (a) in the figure. Then this surface is exposed to UV light from the arc lamp, and spectra are recorded again. The XPS spectra after UV exposure are shown in Figure 5.6 as curve (b). Next O_2 gas is introduced into the chamber through a dosing tube situated directly above the sample. The O_2 partial pressure is maintained at $1x10^{-7}$ Torr for 30 minutes. Then the gas is pumped out, and another XPS scan of the Ti-2p and O-1s regions is taken. The resulting spectra are shown as curve (c) in the figure.

When the Ti-2p spectra are examined, it is clear that UV exposure causes the growth of a shoulder 1.7 eV to lower binding energy of the main Ti^{4+} peak. As previously mentioned (see Section 3.5.2.3), such a shoulder is indicative of Ti^{3+} defects. The curve shown was taken after 90 minutes of UV exposure, when defect production had saturated. To determine the saturation fluence needed to produce the maximum number of defects possible, spectra were taken after UV exposures in 30 minute increments. After the first 30 minutes, a small number of defects appeared, and the number of defects increased with each dose until 90 minutes of exposure had been reached. Beyond this point, no more defects were created with additional UV exposure. No other shoulders appeared in the spectra, ruling out creation of defects with Ti^{2+} or other valence states. The 90 minute exposure corresponds to a total saturation fluence of 270 J/cm^2. The saturation fluence for UV-defect creation using the pump beam in SHG experiments was 360 J/cm^2 (see Section 5.1). Estimation of the power density for XPS studies is crude, however, such that these two results are consistent. (No means exists to directly measure the power density striking the sample in the XPS chamber, requiring that this be estimated. The estimate of $\approx$50 mW/cm^2 could be off by as much as 50%.) This leads to the conclusion that UV-defect creation in both studies, using different

sources and wavelengths of UV, saturates at roughly the same UV fluence. The overlapped Ti-2p spectra also show that O_2 exposure electronically heals the UV created defects, since curves (a) and (c) overlap exactly. Furthermore, the process of UV defect creation and O_2 defect healing can be cycled indefinitely, as seen in SHG experiments.

5.2.2.2 More Detailed Comparisons

Analysis of the O-1s overlapped spectra is a little more complicated. In each spectrum, the main O-1s peak is accompanied by a shoulder 2.2 eV to higher binding energy. This shoulder is consistent with both OH and CO bonds on the surface. Figure 5.7 shows an XPS scan of the etched surface over a very broad energy range. (On this graph, the number of counts has been multiplied by four for energies below 250 eV to expand small features.) In addition to the features associated with Ti atoms and O atoms on the surface, a peak appears at 290.0 eV. This peak comes from adventitious carbon that was deposited on the surface during handling as it was transferred from the SHG chamber to the XPS chamber.

Exposing the surface to UV light in air cleans off much of this adventitious carbon, but enough remains to account for the shoulder on the oxygen peak. Table 5.2 lists atomic ratios of titanium, oxygen, and carbon for the etched sample as it was introduced into the XPS chamber, and then similar ratios for the surface after UV cleaning in air. Here atomic ratios are calculated by measuring the peak heights for the Ti-$2p_{3/2}$, O-1s and C-1s peaks, dividing these peak heights by the spectrometer sensitivity factor for each peak (1.2, 0.66 and 0.25 respectively) to obtain corrected peak heights, and then directly comparing these peak heights (see Section 3.5.2.2). Unscaled peak heights are measured with a caliper from high-resolution scans of each of the three elemental regions. The carbon contamination of the cleanest surface achieved (the one shown in Figure 5.7) corresponds to 0.33 mL carbon coverage. On surfaces with no charging, the adventitious carbon peak is expected to appear at 284.8 eV. Here charging shifts this peak, and all other peaks, by 5.2 eV (see Section 3.5.1.3). To obtain the absolute energy location of the titanium and oxygen peaks, this shift must be included. But the absolute location of these peaks is not of critical interest here.

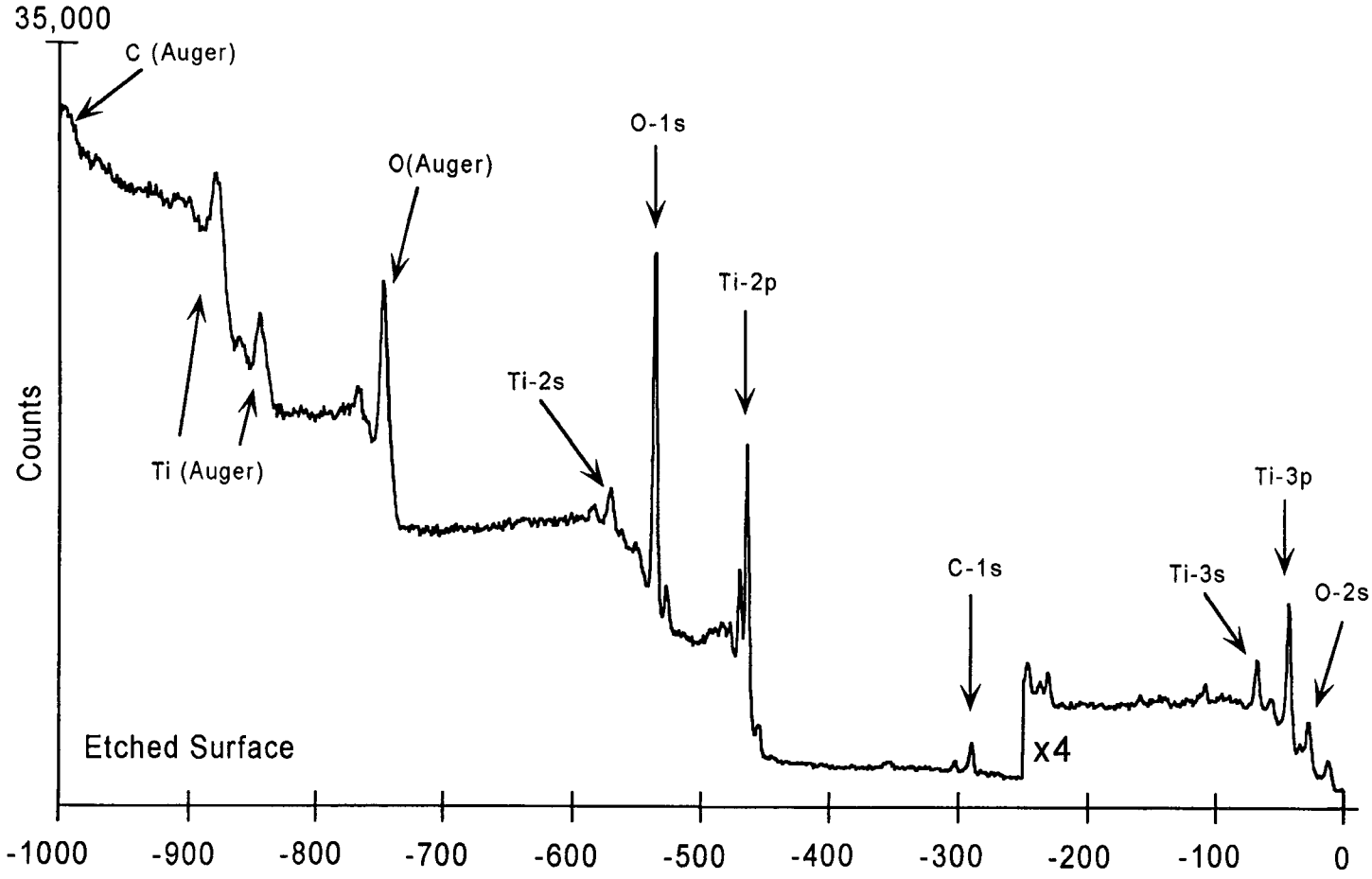

Figure 5.7: XPS survey of the etched (110) TiO_2 surface

Instead, focus is placed on the relative position of shoulders on main peaks. For this reason, all spectra presented here will be plotted without correcting for this charging shift.

The observed adventitious carbon contamination can not be removed without argon sputtering, which is undesirable because it would irreparably damage the etched surface. At this point, it is not possible to determine whether UV defect creation occurs despite this carbon contamination or because of it. It could be argued that the UV is simply assisting the process by which carbon on the surface scavenges lattice oxygen to form CO or CO_2. This is certainly consistent with the overlapped oxygen spectra in Figure 5.6, where a slight narrowing in the CO shoulder is observed after both UV exposure and O_2 defect healing. To determine whether such processes are responsible for the observed UV-induced defects, a surface with no such carbon contamination must be studied. Since exposing the surface to UV in air helps to clean carbon off the surface, it is likely that the same process occurs on samples studied by SHG as they are repeatedly exposed to UV light in 100 T of O_2. Such exposures are now intentionally done whenever a sample is placed in the SHG UHV chamber. It is hoped that this procedure removes enough carbon from the surface to ensure that SHG studies are done on a surface with little contamination. The next section presents results of the UV defect-creation experiment on a surface that is known to have no such carbon contamination.

5.2.2.3 Overall Behavior on Annealed (110) TiO_2 Surfaces

To prepare a well-characterized, contamination-free, defect-free surface, a flat (110) TiO_2 wafer sample is bulk reduced, argon sputtered, annealed at 600°C in $1x10^{-6}$ T O_2, and cooled in this same oxygen environment. This procedure, described in Section 4.3.6, produces what the industry considers to be the most defect-free, stoichiometric surface achievable. No carbon is present on surfaces prepared in this way. Figure 5.8 shows an overlap of spectra for such a surface (a) immediately after its preparation, (b) following a 90 minute UV exposure using the mercury arc lamp, and (c) following a 5 minute O_2 gas dose at $1x10^{-7}$ T. Comparing this overlap to the overlap in Figure 5.6 for the etched sample shows that the two surfaces respond to these treatments in the same way. UV exposure

Table 5.2: Atomic ratios of Titanium, Oxygen, and Carbon on the etched surface before and after UV cleaning in air

Before Treatment

elemental peak	peak height (inches)	scaled peak height (height/sens. factor)	atomic percent
Ti-$2p_{3/2}$	3.412	2.843	22.2%
O-1s	4.615	6.992	54.5
C-1s	0.748	2.992	23.3
		total=12.82	100

After Treatment

elemental peak	peak height (inches)	scaled peak height (height/sens. factor)	atomic percent
Ti-$2p_{3/2}$	3.053	2.544	25.1%
O-1s	4.291	6.502	64.3
C-1s	0.268	1.071	10.6
		total=10.117	100

creates defects on both surfaces, and exposure to O_2 removes these defects. For the annealed sample, curve (c) shows only partial healing after 5 minutes of O_2 exposure. Additional 5 minute doses were done until the resulting Ti-2p spectrum exactly overlapped curve (a). In this way, it was determined that a total exposure of 30 minutes at $1x10^{-7}$ T was required to completely eliminate all traces of UV-induced defects. The fully healed spectrum is not plotted with the curves in Figure 5.8 because it directly overlaps curve (a). These results definitively confirm that above band-gap UV exposure creates Ti^{3+} defects on $TiO_2(110)$ surfaces, independent of surface carbon contamination.

5.2.2.4 More Detailed Comparisons

Several important observations arise from comparison of spectra for the annealed surface and the etched surface. First, the lineshape of the titanium peaks on the etched surface is identical to that of the annealed surface. This means that the etched surface is electronically as "good" (as defect-free) as the annealed surface. The main difference

Figure 5.8: XPS observation of UV creation and O_2 healing of defects on annealed (110) TiO_2

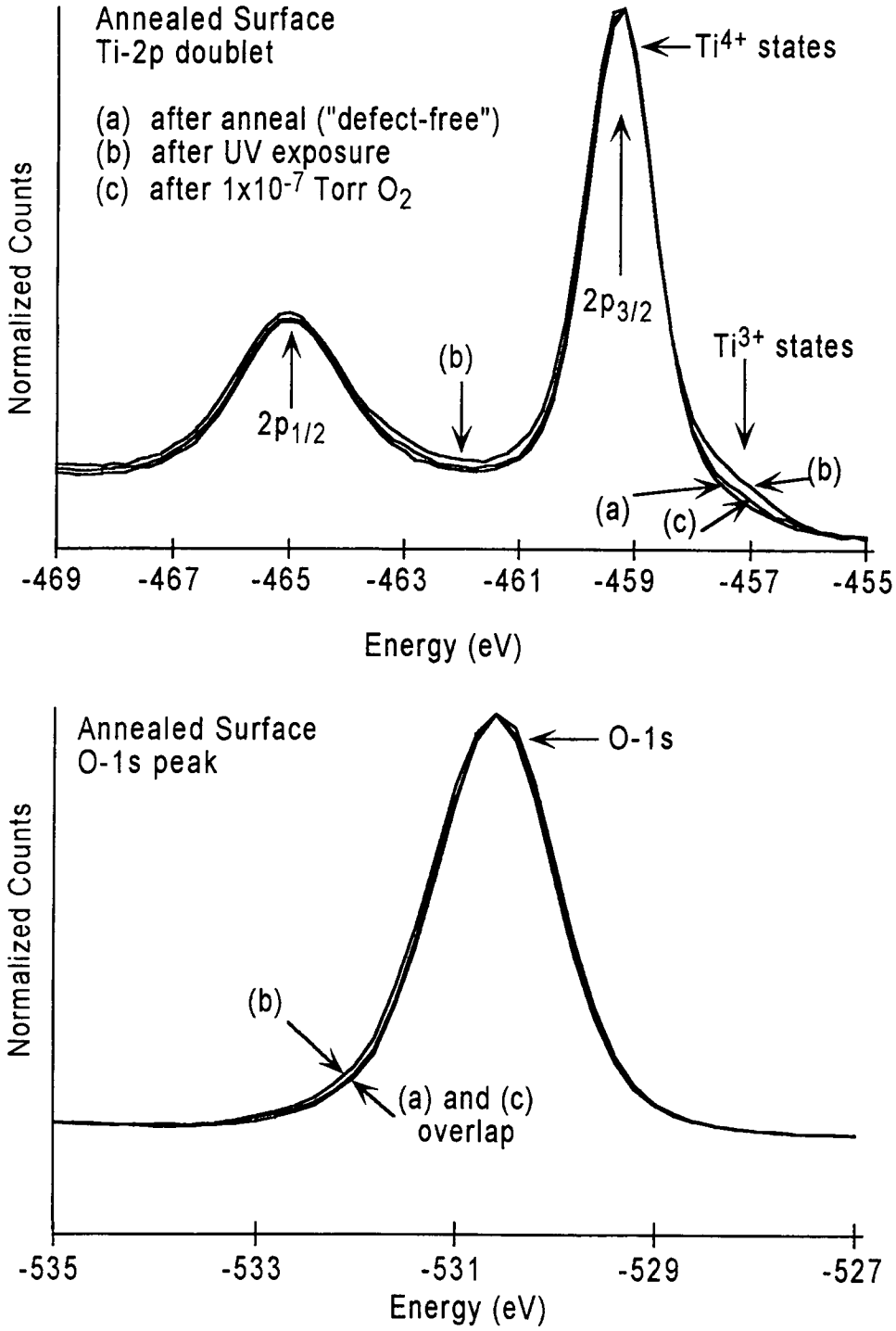

between the two surfaces appears in the O-1s spectra. Since there is no carbon contamination on the annealed surface, no CO shoulder is present on its O-1s spectrum, and the main oxygen peak is nearly symmetric. But when defects are created on the annealed surface, a slight broadening of this peak appears. This broadening disappears when the surface is exposed to O_2. (Such broadening is also seen when defects are produced by other means, such as electron-beam and argon-ion exposure [29].) No absolute explanation for this slight broadening has been established at this point, but it is possible that it is due to residual hydroxyl groups that may be present on the surface. When surface oxygen atoms are removed during UV exposure, the height of the O-1s peak should decrease slightly relative to the height of any peak present due to hydroxyls. This would appear as a slight increase in the hydroxyl peak size when O-1s peaks are overlapped, explaining the observed broadening.

When Figures 5.6 and 5.8 are compared, it is also obvious that more noise exists on the spectra for the etched surface. This is because data were taken every 0.1 eV on the etched surface while they were taken every 0.2 eV on the annealed surface. It was discovered during the course of experiments that changing to the larger step increment resulted in no observed change in the resolution of the spectra, but allowed twice as many scans to be taken over the same time period, resulting in twice the signal-to-noise ratio. For these high resolution scans, each energy window is individually scanned in one data collection cycle. Then the cycle is repeated, and the number of counts at each energy is directly added to the number of counts obtained in the previous cycle. This continues over many cycles, such that peaks grow increasingly larger while valleys (no signal) remain small. The more cycles that can be averaged, the better the signal-to-noise ratio. In the course of a set of experiments, however, it is only practical to collect data for about 30 minutes. During this time, roughly 30 cycles at 0.1 eV step-interval can be taken, while 60 cycles at 0.2 eV step-interval are possible. This explains why the larger interval was chosen when it became clear that doing so would not decrease the resolution of the scans. On all XPS scans presented here, no smoothing or data massaging of any type has been done. When spectra are overlapped, however, it is often necessary to shift one or more of the peaks by a few tenths of an electron volt to make peaks from all spectra exactly coincide. This necessarily makes the energy scale used meaningless. In all cases here, the first spectrum referenced in a graph (usually a

defect-free surface, but occasionally just the starting surface before treatment) is left at the measured energies, and any subsequent peaks place on top of it are shifted to best overlap. In all cases, this shift is small, and is a consequence of slight variations in the amount of charging that occurs on the sample during a given experiment.

5.2.2.5 Quantifying the Number of UV Defects Created

On both the chemically etched and the annealed surfaces, UV defect production and O_2 defect healing can be cycled repeatedly. In all cases, the titanium spectra indicate that the O_2 healed surface is indistinguishable from the nearly perfect annealed surface. Also, each time a surface is exposed to UV from a defect-free state, the titanium spectra after UV exposure exactly overlap. This means that the same number of defects are produced by the UV each time. It is useful to quantify the defect density, so that the number of sites involved in these defect creation and healing processes can be established. To this end, spectra after UV exposure are compared to spectra obtained for annealed surfaces that have been damaged by other means.

As previously discussed (see Section 4.3.6.5), defects can be created on $TiO_2(110)$ surfaces by ion-sputtering and through exposure to a low-energy electron beam. XPS and UPS studies have established [29] that defects created by sputtering are extensive, occurring several atomic layers on and below the surface, and can be of several different valences (Ti^{3+}, Ti^{2+}, and Ti^{0+}). In contrast, defects created by low-energy electron beam exposure are of Ti^{3+} type only and are confined to the topmost surface layer. Figure 5.9 shows an overlap of the Ti-$2p_{3/2}$ peak for a defect-free surface, three surfaces with electron beam damage, an Ar^+-ion sputtered surface, and a UV-exposed surface. Here only the 3/2 peak in the Ti-2p doublet is shown to expand the area where defects appear. Curves (a)-(d) are from a detailed study of damage caused by low-energy electron beams [29]. This study was done prior to the work in this thesis, and on a different $TiO_2(110)$ crystal than the one used for the UV work presented here. There is a great deal of consistency, however, between spectra on different $TiO_2(110)$ crystals, as long as they are prepared in the same way. Titanium spectra taken on both crystals after annealing overlap exactly. In addition, a

Figure 5.9: Overlap of Ti-$2p_{3/2}$ Peaks for the annealed surface: (a) before any treatment; after damage by 0.48 keV electrons at exposures of (b) 0.007 C/cm^2; (c) 0.026 C/cm^2; and (d) 0.075 C/cm^2; after (e) UV exposure; and after (f) Ar^+ ion sputtering.

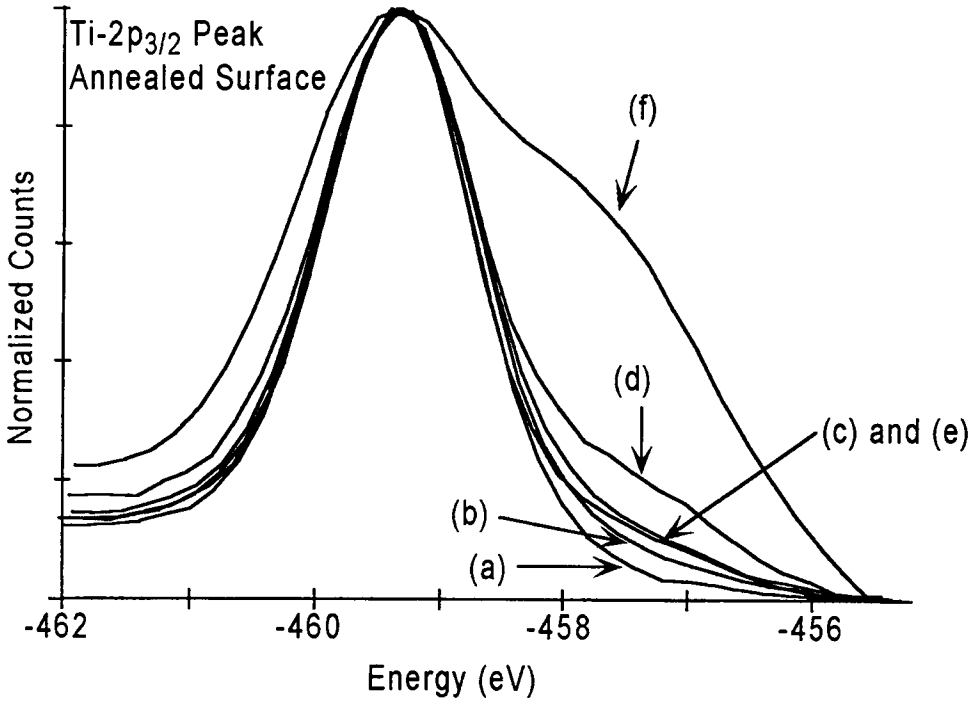

few test exposures with the electron beam were also done on the sample used for study of UV-induced defects. The results was that defects were created in the same way and at the same rate on the sample used in UV experiments as was seen on the previous sample. These observations suggest that spectra for these different samples can be compared directly.

In the study of damage caused by low-energy electron beams, 0.48 keV electrons were emitted from the electron gun (see Section 4.3.6.5) to strike the sample. This beam was directed onto the sample for given periods of time, with spectra taken in between each successive dose. This study showed that such low-energy electrons created Ti^{3+} defects on the surface, but not so that the number of defects increased linearly with dose. The total electron dose on the sample was determined by measuring the current established by the electrons striking the sample and using this to calculate the total amount of charge

Figure 5.10: Ti^{3+}/Ti^{4+} peak ratio as a function of electron beam exposure for low-energy electron-beam damage

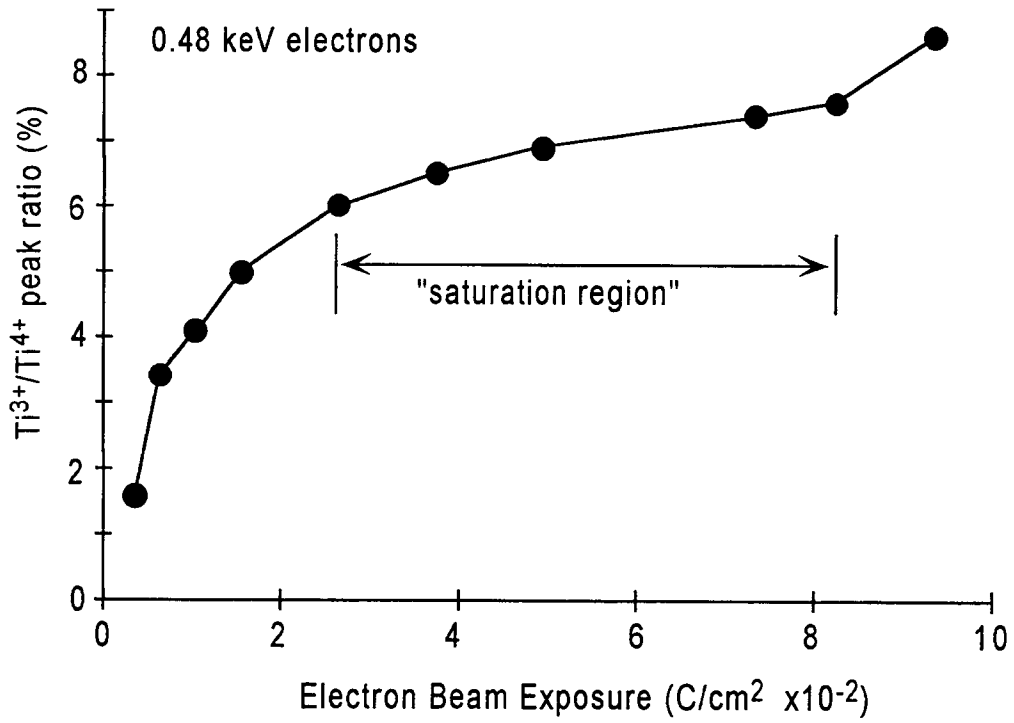

per area striking the surface over the course of each exposure. Figure 5.10 shows the area ratio of the Ti^{3+} and Ti^{4+} peaks as a function of electron dose. As more defects are created this ratio should clearly increase. But this increase does not happen in a linear fashion. For low exposures to the electron beam, defects are created quite rapidly (Ti^{3+}/Ti^{4+} = 0-6%). Then a saturation region is reached (Ti^{3+}/Ti^{4+} = 6.5-7%) where additional beam exposure creates comparatively only a few more defects. After considerably longer exposures, defect production rate increases again. Here data for 0.48 keV electrons only are shown, though similar curves were obtained for electrons of various energies. In addition, no data are presented for exposures larger than 0.10 C/cm^2. Data for longer exposures were taken, but are not shown here so that low exposure behavior may be better observed. For longer exposures, the trend observed for the 0.10 C/cm^2 data point continues: the defect production rate is larger than the rate seen in the saturation region, but is not as rapid as initial defect production.

Curvefitting the spectra obtained in this study [29] allows the number of defects produced to be determined. Such curvefitting leads to the determination that the saturation region (Ti^{3+}/Ti^{4+} = 6.5-7%) corresponds to a defect density consistent with defect sites at between 1/4 and 1/3 of the titanium atoms on the surface. Since each oxygen vacancy creates two Ti^{3+} defects, this is removal of 1/8 to 1/6 of the oxygen atoms present on an ideal surface. On an ideal surface the total density of oxygen atoms is $1.56x10^{15}/cm^2$, with 1/3 of these being bridging oxygen atoms ($5.2x10^{14}/cm^2$) and 2/3 being lattice oxygen atoms ($1.04x10^{15}/cm^2$) [29]. Removal of 1/6 of the total number of oxygen atoms on the surface creates a vacancy density of $2.6x10^{14}/cm^2$. If all of these vacancies are generated by removing exclusively bridging oxygen atoms, this corresponds to oxygen vacancies at fully 1/2 the bridging oxygen sites on the surface.

The "saturation region" described above for electron-beam exposure does not constitute true saturation of defect density because continued exposure to the low-energy electrons always results in the creation of more defects. The rate of defect creation only slows dramatically after the "saturation region" is reached. In contrast, true saturation occurs when surfaces are exposed to UV. After a certain number of defects have been created by UV, additional UV exposure creates no more defects. Figure 5.9 shows that at this saturation point UV has created the same number of defects as were seen in the "saturation region" for electron-beam damage. This corresponds to vacancies for 1/6 the total oxygen atoms on the surface, as described above. This suggests that defects can be readily created on these surfaces up to the 1/6 total oxygen limit. Beyond this limit, defect production is not favorable. For UV, no mechanism exists by which such defects can be produced; for electron-beam exposure, such mechanisms exist.

An Ar^+-ion sputtered surface is also included in the overlapped spectra of Figure 5.9. This helps to show the dramatic difference between damage done by "gentle" means, such as UV irradiation and electron-beam exposure, and the extensive damage generated by sputtering. A sputtered surface can even have more titanium atoms in defect states than remain fully coordinated. As previously mentioned, defects created by ion sputtering are not restricted to the topmost surface layer, while electron-beam or UV induced defects are. This is best observed by exposing surfaces with each type of damage to O_2. Strictly surface

Figure 5.11: Overlap of Ti-2p peaks for (a) a defect-free surface; (b) a surface after 1 keV Ar^+ sputtering for 12 minutes; and (c) the sputtered surface after $1x10^{-6}$ T O_2 for 30 minutes.

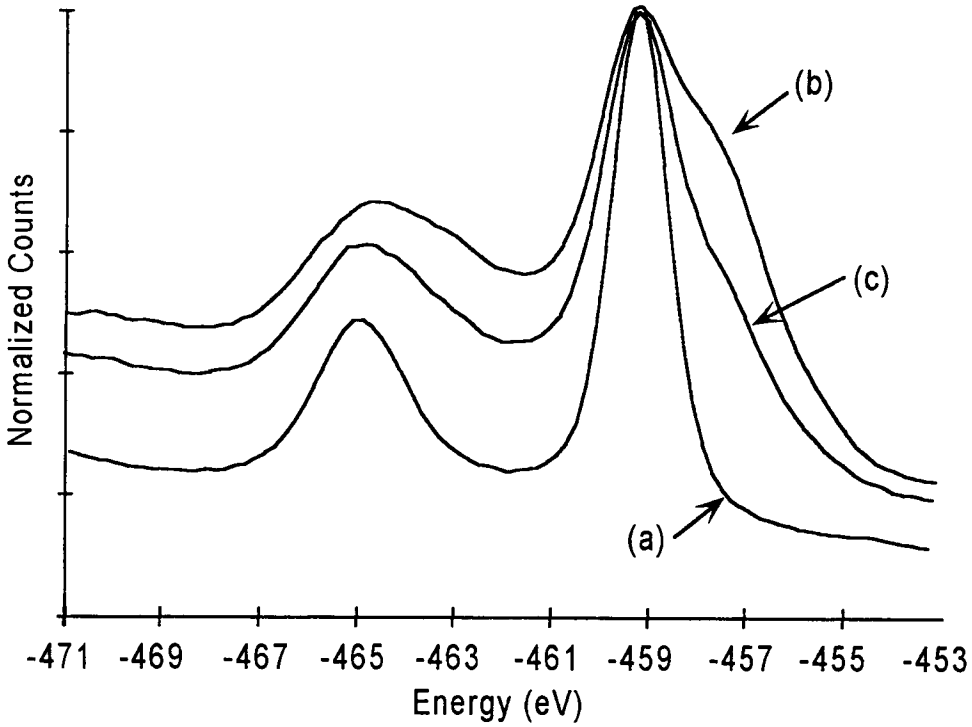

damage is healed by oxygen exposure, while sub-surface defect states remain unhealed. This was shown in for UV-damaged surfaces in Figure 5.8, where a $1x10^{-6}$ T O_2 dose healed all defects. Exposing an electron-beam damaged surface to oxygen results in identical healing behavior. But an Ar^+ sputtered surface behaves differently, as shown in Figure 5.11. Here oxygen exposure only partially heals defects. Even exposure to air is insufficient to cause complete defect healing. In order to restore the Ar^+ sputtered surface to its stoichiometric, defect-free state the sample must be heated to above 600°C in an oxygen environment. This suggests that the healing observed on Ar^+ sputtered surfaces occurs only on the top surface layer, such that buried defects that can not be reached by additional oxygen exposure are detected by XPS in the layers below the surface. But this must be confirmed using other methods to rule out the possibility that healing is occurring only a specific sites. This is done using UPS, as shown in the next section.

Figure 5.12: UPS spectrum for a "defect-free" annealed surface.

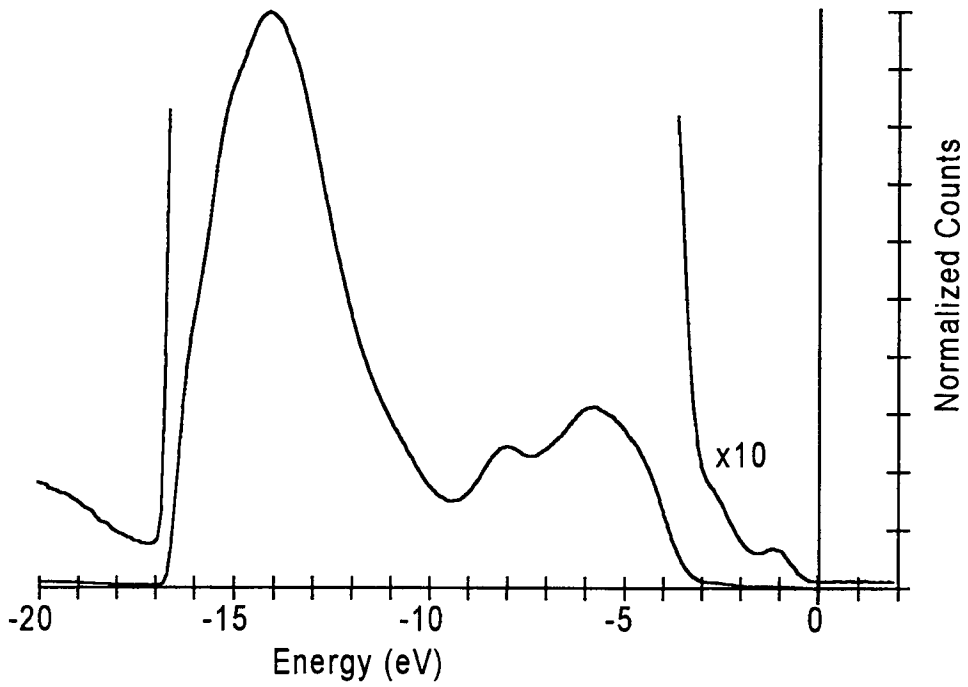

5.2.3 Use of UPS to Probe Surface Defects and Interactions

As was discussed in Section 3.6, Ultraviolet Photoelectron Spectroscopy can also be used to detect the presence of defects on TiO_2 surfaces. In UPS, 21.2 eV He-I UV photons are directed onto the sample. The photons remove electrons from the valence band of the surface, and these electrons are detected and sorted by their kinetic energy as electrons were during XPS experiments. The result is a spectrum showing valence band structure. Figure 5.12 shows one such UPS spectrum for a defect-free surface prepared by sputtering and annealing in O_2. Here the large peak centered between -14 and -15 eV is largely due to electrons from near-surface layers that experience loss before detection. The peaks at -6 eV and -8 eV are from electrons in the O-2p valence band of the surface. The valence band edge is also apparent at about 3 eV, an energy consistent with the bulk band gap. Here there should be no states in the band gap, but some are indeed present. In order to see the small

number of electrons in this defect state, the spectrum must be expanded by a factor of 10. This expansion is included in Figure 5.12. When defects are created on $TiO_2(110)$ surfaces using ion sputtering or low-energy electron bombardment, the defect peak in the gap grows. This is shown by overlapping three UPS spectra, shown in Figure 5.13. Here spectra for a defect-free annealed surface (ann.), a surface with electron-beam damage in the "saturation region" (e-beam), and an Ar^+-sputtered surface (sput.) are shown in the top graph of the figure, while a x10 expansion of these spectra is shown in the bottom graph. The bottom graph shows that both the electron-beam exposed and the ion-damaged surfaces have a large defect state in the gap. Here the argon sputtered peak is the largest, followed by the electron-beam peak. But beyond this rough quantification of the number of defects present, very few conclusions can be drawn from the UPS spectra. The background signal from electrons experiencing loss changes dramatically once the surface is sputtered, and changes in the structure of the O-2p valence band are evident even for electron-beam damage. These changes are complex, and do not follow any trend determined to this point.

UPS spectra have their use in determining whether or not defects are confined to the top surface layer. UV photons eject electrons that have much lower energy than those emitted by XPS. These electrons are much more easily scattered to become background signal than the higher energy XPS electrons. For this reason, UPS peaks contain only electrons that come from the very top surface layer. While XPS can probe 1-10 atomic layers, UPS can be considered as a probe of only 1-2 atomic layers. Figure 5.14 shows UPS spectra taken for surfaces in the XPS experiments of Figure 5.11. Here the expanded graph shows that Ar^+ sputtering creates defects, as expected, but that these defects are almost completely healed by O_2 exposure. XPS showed only partial healing. The remaining defects seen by XPS then must come from buried layers not seen by UPS.

Care must be taken when analyzing UPS spectra. If changes in these spectra are slight, then they may be overlapped and interpreted without concern. But if changes in spectra are more dramatic, determining the proper way to overlap these spectra is not trivial. For example, in all of the above spectra, curves are overlapped by normalizing the spectra so that the large background peak between -15 eV and -14 eV is taken as the height reference. That is, the tallest point of this peak is normalized to 1. But in some spectra, this peak

Figure 5.13: UPS spectra for three surface treatments: annealed, electron-beam damaged, and argon-ion sputtered.

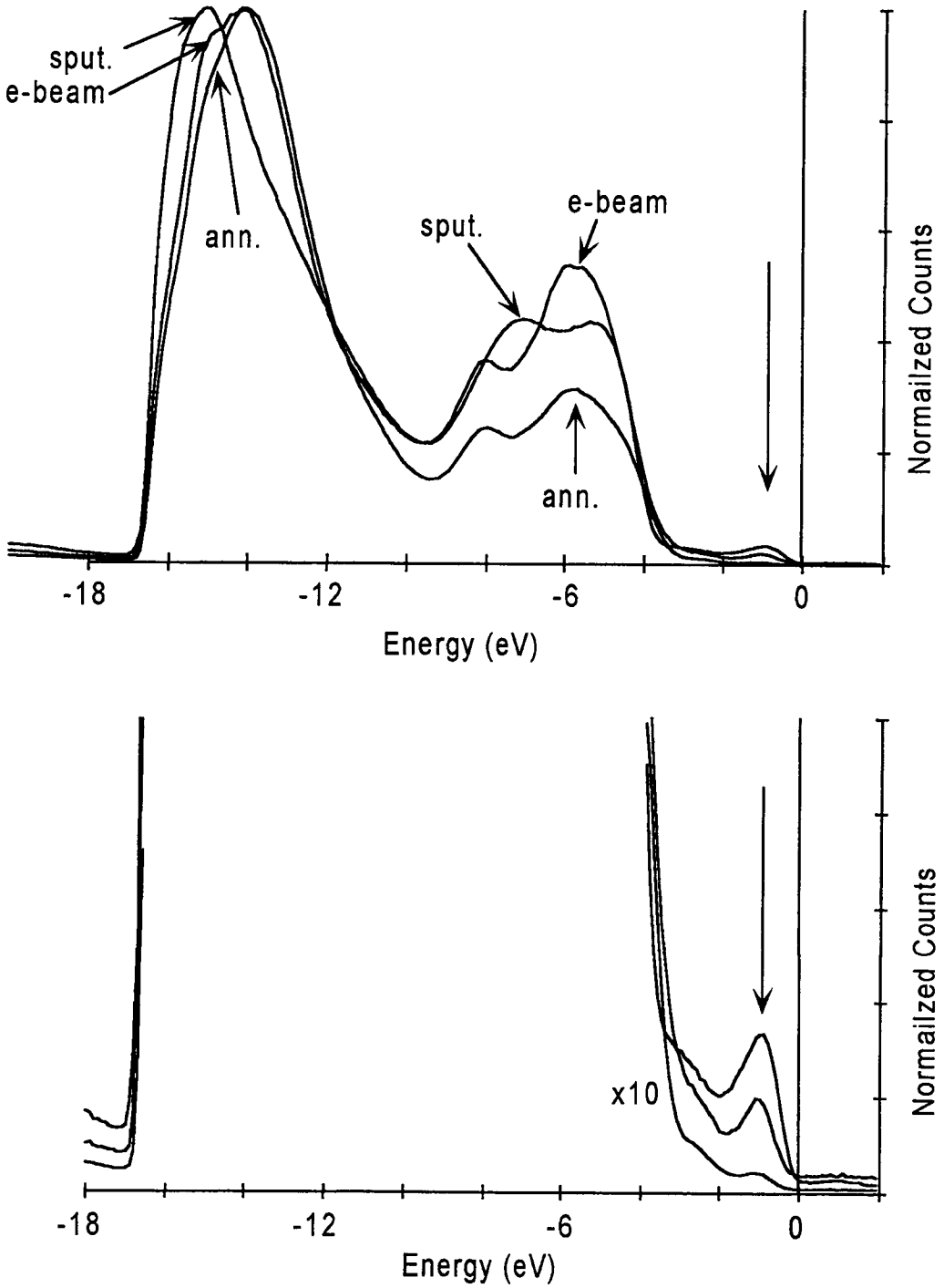

Figure 5.14: UPS spectra for three surface treatments: annealed, argon-ion sputtered, and argon-ion sputtered after O_2 exposure.

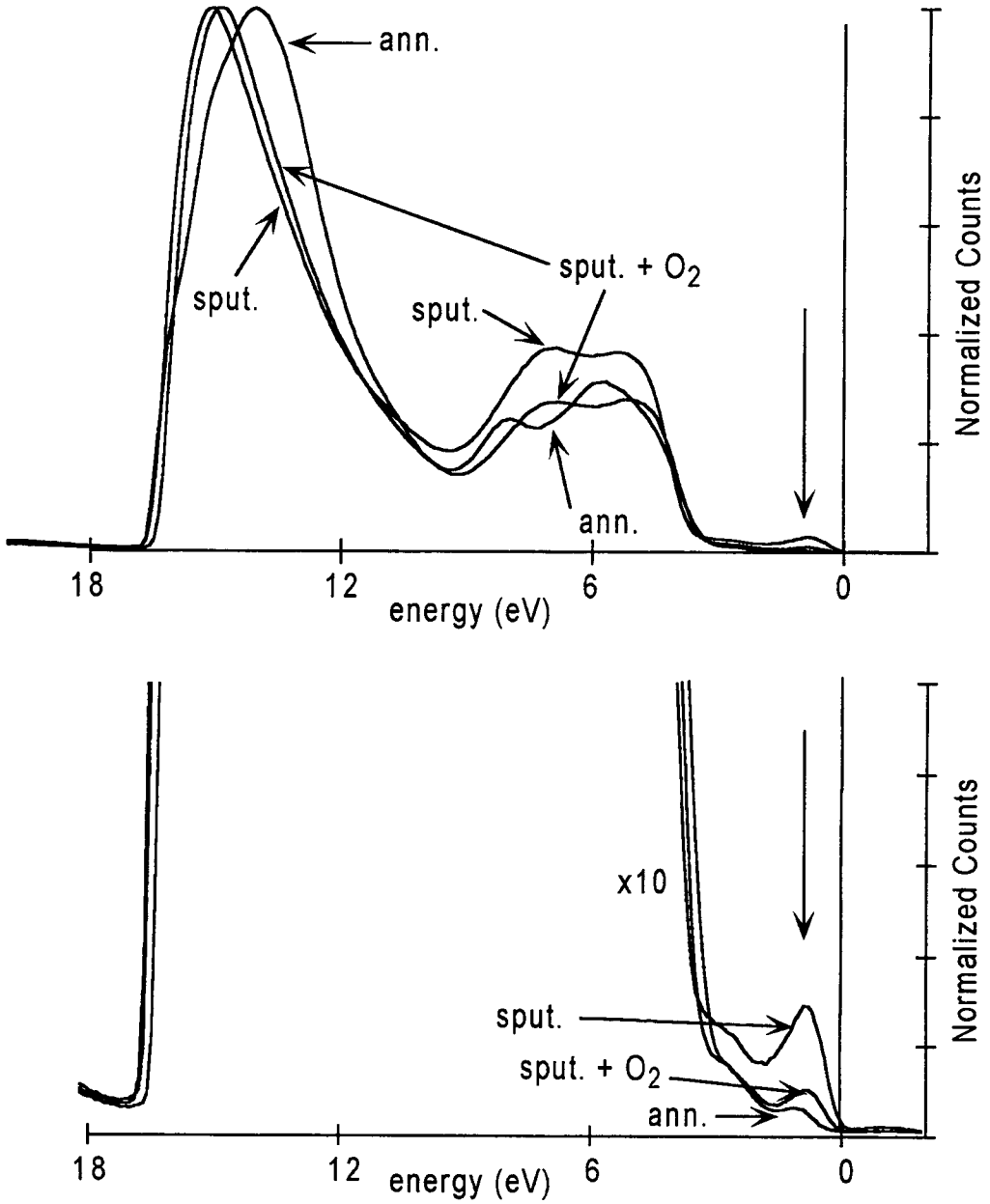

clearly has a different shape, and even a slightly different position, than it has in other spectra. It can also have a very different relative height as compared to the O-2p band features at about -6 and -8 eV. So using this feature as a reference for overlapping spectra does not always make sense. When dramatic changes in spectra occur, no features remain consistent enough to use as references. For graphs where spectra are expanded to show the defect peak in the band gap, scale comparisons are equally difficult. Typically, the jump in signal on the left of the graph is used as a reference. When the x10 expansion is made, these background jumps frequently overlap well enough to allow unambiguous interpretation of the heights of the defect peaks. But if these don't overlap, one or more of the expanded spectra must be re-scaled such that they do. Then the expansion is no longer uniform, and peak sizes become less meaningful. In general, UPS should only be used to observe very large changes in the number of defects on the surface when the overall UPS spectra change little. Unless a consistent feature is present to allow obvious overlap of the spectra, determination of the number of defects present should not be attempted.

5.2.4 Section Summary

The experiments presented in this section show that UV light with above band-gap photon energy (3.4 eV and 4.7 eV) creates Ti^{3+} defects on $TiO_2(110)$ surfaces prepared by mechanical polishing, chemical etching, and thermal annealing. These defects are restricted to the top surface layer, and are very similar to defects created by low-energy electron bombardment. The main difference between defect production by these two methods is that UV defect production saturates, while electron-beam defect production does not. The number of UV defects at saturation can be quantified, and corresponds to vacancies at 1/6 the possible oxygen atom sites on the surface. If only the bridging oxygen atoms are being removed by UV, then fully half these bridging atoms are removed by UV exposure to saturation.

Exposing surface defects to O_2 results in rapid healing. For Ti^{3+} defects limited to the topmost surface layer, which are produced by either UV exposure or electron-beam exposure, complete defect healing occurs when defective surfaces are exposed to only $1x10^{-7}$

T O_2. Damage that is more extensive than this can not be entirely healed by such oxygen exposures. Ion-sputtered surfaces are damaged over several near-surface layers such that oxygen exposure only heals the top layer, leaving buried defects that are still detectable using XPS.

Early work using SHG led to the interpretation that the surfaces studied were covered with Ti^{4+}:O_2^- complexes that became sites for UV defect creation and O_2 defect healing. The incident UV light was thought to break apart such a complex by creating an electron-hole pair in the bulk of the sample, with the hole migrating to the surface to capture the electron holding the complex together. O_2 exposure then healed defects by reforming the complexes. An alternative explanation was that UV was removing bridging or lattice O^{2-} *atoms* to create defects, and O_2 exposure resulted in defect healing through O_2 dissociation only. This explanation was not favored because removal of a tighly-bound lattice or bridging oxygen atom by photons barely above the band-gap was thought to be impossible without the presence of steps or other lattice deformations. It was hoped that XPS studies would point to one interpretation over another, however, to end any debate on the mechanisms involved in these processes. Unfortunately, this was not the case.

XPS studies on the samples used in SHG experiments confirmed that defects were created by UV and healed by O_2, but provided no evidence for the existence of O_2 bound intact on the surface. It was thought at this point that the complexes that became defect sites after UV exposures might exist only at steps on the etched and polished surfaces studied by SHG, so that similar studies on a verifiably "perfect" surface would result in no UV-induced defects. Surprisingly enough, the etched surfaces studied were found to be as defect-free as the best surfaces producible by thermal annealing, and UV defect production was also observed on annealed samples. This forces the conclusion that either a mechanism exists by which UV light can remove tightly bound bridging oxygen *atoms* or even the most "perfect" surfaces producible are covered with Ti^{4+}:O_2^- complexes that can not be detected. Both possibilities alarmed those who routinely study annealed samples. The first seems to require the invention of some new physics. The second calls into question not only the quality of the surfaces studied, but also the ability of conventional surface science techniques to observe physical defects. The techniques used here indicate that the surfaces

studied have no *electronic* defects. That is, each titanium atom is fully coordinated and has its electrons in shells at the same energy as all other titanium atoms on the surface. But these techniques can not determine whether a state with no electronic defects can be achieved when the titanium atoms are bound to something other than the expected O^{2-} ion, such as a molecular O_2^- ion. This would constitute an undetectable physical defect.

This leads to the question of whether some other molecule could bind to a titanium 3+ ion to produce a surface that appeared electronically defect-free when it in fact had physical defects. The search for complexes formed in this way partially motivates the remaining research in this thesis, though success has not been realized on this issue. Resolution of the mechanism quandary introduced by UV defect creation on these surfaces is not trivial.

5.3 Interaction Between H_2O and Defects on (110) TiO_2 Surfaces

As discussed in Section 2.4.3, much research has been done in an attempt to understand the interaction between H_2O and TiO_2 surfaces. Studies of surfaces exposed to water by different groups have led to three different conclusions, namely that water (1) does not interact with defects, (2) creates defects and (3) removes defects. There is also no agreement as to whether water adsorbs on defect-free surface molecularly or as hydroxyl groups through dissociation [99]. One way to shed light on some of these contradictory reports is to study water-surface interactions using XPS. This will allow direct observation and quantification of the defect states present on the surface. Previously, UPS was used to attempt this. These studies led to some of the contradictory interpretations of spectra largely because of the ambiguity present in overlapping spectra obtained by UPS. Different groups selected different spectral features as references, aligned and overlapped their spectra in different ways, and drew conflicting conclusions. Until some means of calibrating UPS spectra absolutely is developed, such confusion will always accompany UPS results. High-resolution XPS spectra, on the other hand, provide a more direct and quantifiable measure of the presence and fate of defects on these surfaces. In the following sections, studies of interactions between H_2O and $TiO_2(110)$ surfaces will be presented. Defect-free surfaces and surfaces with either electron-beam induced or ion-sputtered defects will be exposed

to both vapor and liquid water. These will be *ex situ* studies, in that samples will be transferred to the reaction chamber for vapor exposures or to the electro-chemical liquid cell for dipping in liquid water, and then returned to the main chamber for collection of XPS spectra. Here a cell containing distilled, de-ionized liquid H_2O is attached to the side of the reaction chamber, and separated from the reaction chamber by a leak valve. Water vapor can then be introduced to the reaction chamber by incrementally opening this leak valve to establish the desired dosing pressure. Before sample introduction, the air above the water sample is evacuated repeatedly to remove any contamination. The reaction chamber is then baked, and again flooded with water vapor to ensure minimal contamination by other species.

5.3.1 H_2O on Annealed, "Defect-free" Surfaces

Figure 5.15 shows the result of interactions between vapor and liquid water on a "defect-free" surface prepared by thermally annealing a sputtered sample, as described in Section 4.3.6. Here the defect-free surface, shown in curve (a), has the broadest Ti-2p peaks, and the narrowest O-1s peak. Curve (a) overlaps spectra obtained for all other annealed surfaces to date, and represents the narrowest peaks obtainable by annealing. Curve (b) is obtained by exposing the surface shown in curve (a) to $4.5\text{x}10^{-6}$ T H_2O for five minutes. (Smaller doses than this were done, including a $1\text{x}10^{-6}$ T five minute dose, producing no observable change in either the Ti-2p or O-1s spectra.) For the dose in curve (b), the Ti-2p peaks nearly overlap those of the untreated surface, though a very slight narrowing of the right side of the peaks is evidence that healing of a very small number of residual defects has occurred. In addition, the O-1s peak following the first water dose exhibits slight broadening to lower binding energy. This broadening is consistent with the presence of a small number of hydroxyl groups on the surface. Curve (c) shows the result of a much larger (0.6 T, 5 minute) vapor dose. After this dose, more narrowing of the Ti-2p peaks and more hydroxyl broadening of the O-1s peak are observed. Dipping the sample in water results in the narrowest Ti-2p peaks observed, and in the largest hydroxyl shoulder on the O-1s peak, as shown in curve (d). The growth of the hydroxyl peak in the O-1s spectrum

Figure 5.15: XPS spectra showing interactions between H_2O and a defect-free (110) TiO_2 surface

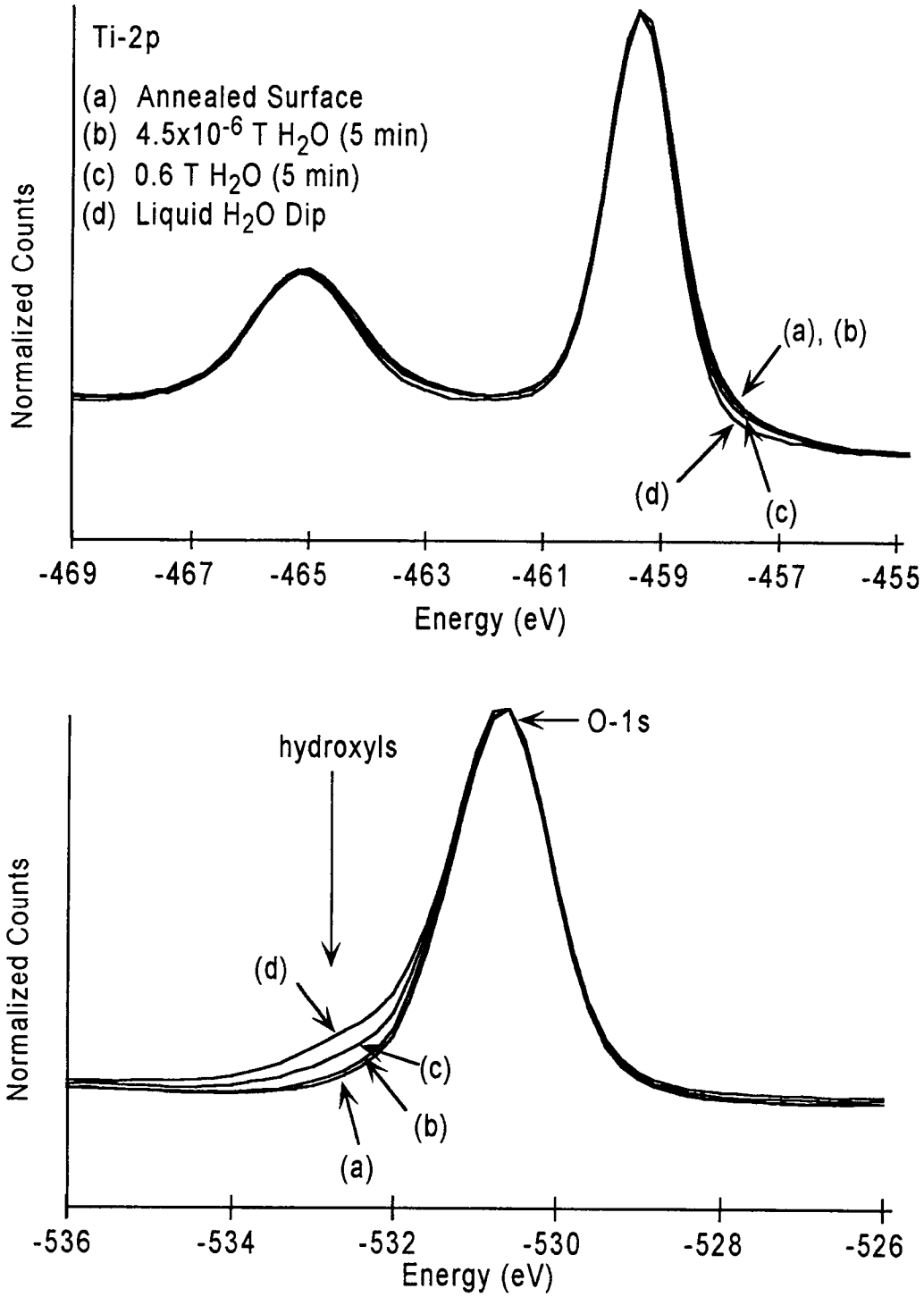

seems to correlate well with the removal of Ti^{3+} signature in the Ti-2p spectrum. This seems to support the interpretation that water dissociates on $TiO_2(110)$ surfaces to heal any Ti^{3+} defects present. This may occur through the formation of Ti^{4+}:$(OH)^-$ complexes, in analogy to the previously proposed Ti^{4+}:O_2^- complexes, providing an explanation of the observed OH shoulder. Clearly the broadening of the oxygen peak is proportionally larger than the narrowing of the titanium peaks. This might lead to the conclusion that additional hydroxyls are adsorbing at sites where no defects are present, but a more likely explanation is that the additional hydroxylation comes from the extra hydrogen atom present in the dissociation of water attaching to a bridging or lattice oxygen atom on the surface [32].

OH area ratios can be obtained by fitting two curves to the O-1s region. For the surface before water treatment, a symmetric Gaussian-Lorentzian function is used to fit the O-1s peak. The result of this is a good fit to the observed peak for fitting parameters of full-width at half maximum (FWHM) of 1.6 eV, and percentage Gaussian of 90%. When two curves are used to fit the water dosed spectra, the FWHM is maintained. The result is a good fit for this FWHM for two peaks with percentage Gaussian of 100% and peak separations of 1.1-1.6 eV depending on exposure. Once two-peak spectra are fit, the ratio of the area of these peaks becomes a measure of the relative number of hydroxyl sites present on the surface. (Similar fitting procedures were used to determine Ti^{3+}-to-Ti^{4+} peak ratios for the electron-beam defect study [29]. But the defect study was done prior to my involvement in the research, so the details of this process are not presented here.) After the 4.5×10^{-6} T exposure, the OH coverage was ~0.04 monolayer (ML), while for the high pressure vapor exposure this climbed to ~0.14 ML. Liquid exposure resulted in saturation of the OH peak at ~0.25 ML hydroxyl coverage. This is hydroxylation of 1/3 of the oxygen atoms on the surface. If all of this hydroxylation comes from H_2O dissociation that occurs only to heal defects, then 1/6 of the total oxygen sites on the surface must have been vacant. This is consistent with the amount of defect healing observed on the surface.

Clearly there are quite a number of defects present on this surface, even after it was annealed to produce what was considered a "defect-free" state. The reason for this is simple. Water studies on these surfaces were done before oxygen studies, though they are presented in reverse order here. Initially, the recipe for producing a "defect-free" surface was to anneal

samples at 600°C for 30 minutes in $1x10^{-7}$ T O_2, and then to cool them in this oxygen environment to room temperature. This established recipe produced the annealed surfaces used in the water study, which were assumed to be defect free. Following the observation of defect healing during water exposure, it became clear that these surfaces were in fact highly defect-ridden. The annealing recipe was then called into question. Subsequent re-evaluation showed that the sample was actually getting considerably hotter than 600°C using electron-beam heating at its original settings. Decreasing the current of the electron-beam heater and increasing the O_2 partial pressure to $1x10^{-6}$ T during the anneal resulted in annealed surfaces with very narrow Ti-2p peaks. Surfaces were prepared using this new recipe in the studies of other molecules that followed, including the O_2 studies presented here in Section 5.2.2.3. When water dosing experiments were later repeated on a defect-free surface made using the new recipe, no defect healing was observed. But, the OH shoulder still appeared on the O-1s peak, indicating that surfaces were becoming hydroxylated despite the absence of defects. This suggests more than one process by which water can dissociate and hydroxylate the surface.

5.3.2 H_2O on Surfaces with Electron-Beam Induced Defects

Surfaces with defects produced by electron-beam bombardment were also exposed to vapor and liquid water and studied using XPS. Here surfaces were prepared by creating a "defect-free" surface by sputtering and annealing to 600°C in O_2 (using the old recipe), and then exposing the resulting surface to the 0.48 keV electrons for 30 minutes. This dose was selected by comparing to the previous study on electron-beam induced defects (see [29] and Section 5.2.2.5), and corresponds to defect creation in the "saturation region" observed in that study. Scans taken before and after electron bombardment show a substantial number of defects appearing as a consequence of the exposure. The damaged surface was then transferred to the reaction chamber for vapor water exposures, and then back to the main UHV chamber for measurement of XPS spectra. A liquid water dip was also done. The results of these experiments are shown in Figure 5.16. Here curve (a) is the surface with electron-beam induced defects. Curve (b) shows the same surface after a 0.6 T 5 minute

Figure 5.16: XPS Spectra showing interactions between H_2O and an electron-beam damaged (110) TiO_2 surface

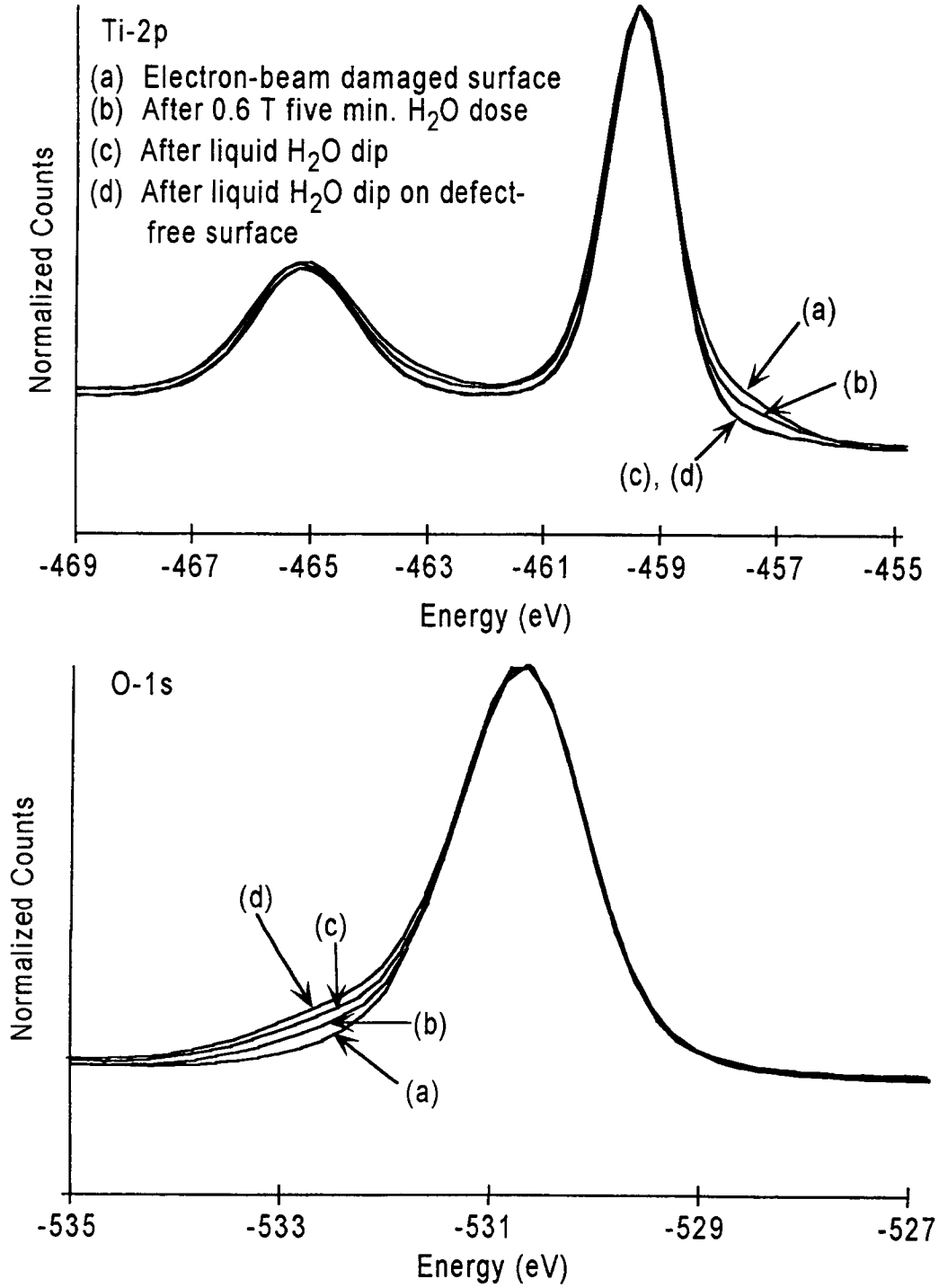

vapor water exposure. Curve (c) shows an electron-beam damaged surface after a liquid water dip. Curve (d) shows a plot of the liquid water-dosed "defect-free" surface from Figure 5.15. Curve (d) was included to show that the final states for both annealed and electron-beam damaged surface after a liquid water dip have identical Ti-2p spectra, but that slightly more hydroxyls are present on the water exposed annealed sample. The reason for this slight difference has not yet been established. A vapor water dose at $4.5x10^{-6}$ T for five minutes was also done, but is not shown in this figure because it almost exactly overlapped curve (a). The curves shown here confirm observations for the annealed surface. Small doses of vapor H_2O cause little change in the number of defects present, while large doses do heal a substantial number of Ti^{3+} defects. Exposure to liquid water results in the narrowest Ti-2p peaks possible, representing complete healing of all defects present. The O-1s spectra show that hydroxyls grow on the surface in the process. It is possible that defects are being electronically healed by hydroxyls to form Ti^{4+} :$(OH)^-$ complexes, as suggested previously. But this can not be conclusively demonstrated because hydroxyls adsorb on surfaces that start out defect-free. It remains possible that physical defect healing occurs instead to form stoichiometric Ti^{4+}:O^{2-} pairs as water dissociates. But this provides no explanation for the hydroxylation that occurs.

5.3.3 H_2O on Surfaces with Sputter-Induced Defects

Ion sputtering has been used to prepare and damage TiO_2 surfaces for more than 20 years. The first UPS study showing interactions between sputtered surfaces and vapor water was done in 1977 [37]. This study showed no appreciable decrease in the intensity of the defect state in the gap for water exposures up to 10^8 L (this is roughly the same exposure as our 0.6 T five minute dose), in seeming contradiction to our observed defect healing on electron-beam damaged surfaces. The study also showed growth of three peaks in the spectrum with increasing water dosing. Two of these peaks, at -6 eV and -8 eV, were associated with the growth of hydroxyls on the surface, while the third, at about -10 eV, was interpretted as molecularly adsorbed H_2O. We repeated these UPS studies, obtaining similar spectra as those obtained in the 1977 study. In addition, we scanned the surface

using XPS to track defect number more precisely, and included a liquid water dip. Our results indicate that the 1977 study may have drawn conclusions based on inappropriate criteria for overlapping spectra.

Figure 5.17 shows an overlap of XPS spectra for a nearly defect-free surface, a surface that has been sputtered with 1 keV Ar^+ ions for 10 minutes, and the sputtered surface after being transferred from vacuum to a liquid water dip. Clearly the Ti-2p spectra show that a great deal of defect healing takes place in the liquid water, but not all defects are healed. Vapor water doses (not shown) healed defects as well, contrary to the observed behavior in the 1977 study, but did so such that only slight changes in the Ti^{3+} defect peak were observed with each dose. While small changes in defect number are readily detected using XPS, normalization problems often make them undetectable using UPS. In addition, the 1977 study did not expand the region containing the defect state to see if small changes were in fact taking place. Our UPS spectra, when expanded, did show small decreases in the intensity of the defect state with increasing vapor water exposure. But as mentioned previously, such changes are difficult to interpret with confidence for UPS due to the lack of an absolution normalization and overlap scheme.

In the XPS study, healing is saturated after the liquid water dip in that subsequent exposure to water or O_2 results in no change in the number of defects present. The overlap of O-1s spectra for these three surfaces shows two things. First, sputtering the surface results in a broadening of the O-1s peak. This broadening accompanies defect production, and was seen on a smaller scale for the electron-beam damaged surfaces in Figure 5.8. Second, water exposure results in further broadening in the same region as defect-induced broadening as the surface becomes hydroxylated. It is unfortunate that the defect-induced broadening coincides in energy with the hydroxyl peak. This makes determination of hydroxyl peak areas impossible on surfaces with a substantial number of defects.

As observed for oxygen healing of argon-sputtered surfaces, the partial disappearance of the defect signal comes from healing of surface states only. Deeper sputter damage remains unhealed, and contributes to the defect signal that remains even after the water dip or subsequent air exposure. UPS again provides a way to observe this directly. Figure 5.18 shows an overlap of UPS spectra for the Ar^+ surface and this same surface after liquid

Figure 5.17: XPS spectra showing interactions between H_2O and an Ar^+-ion sputtered (110) TiO_2surface

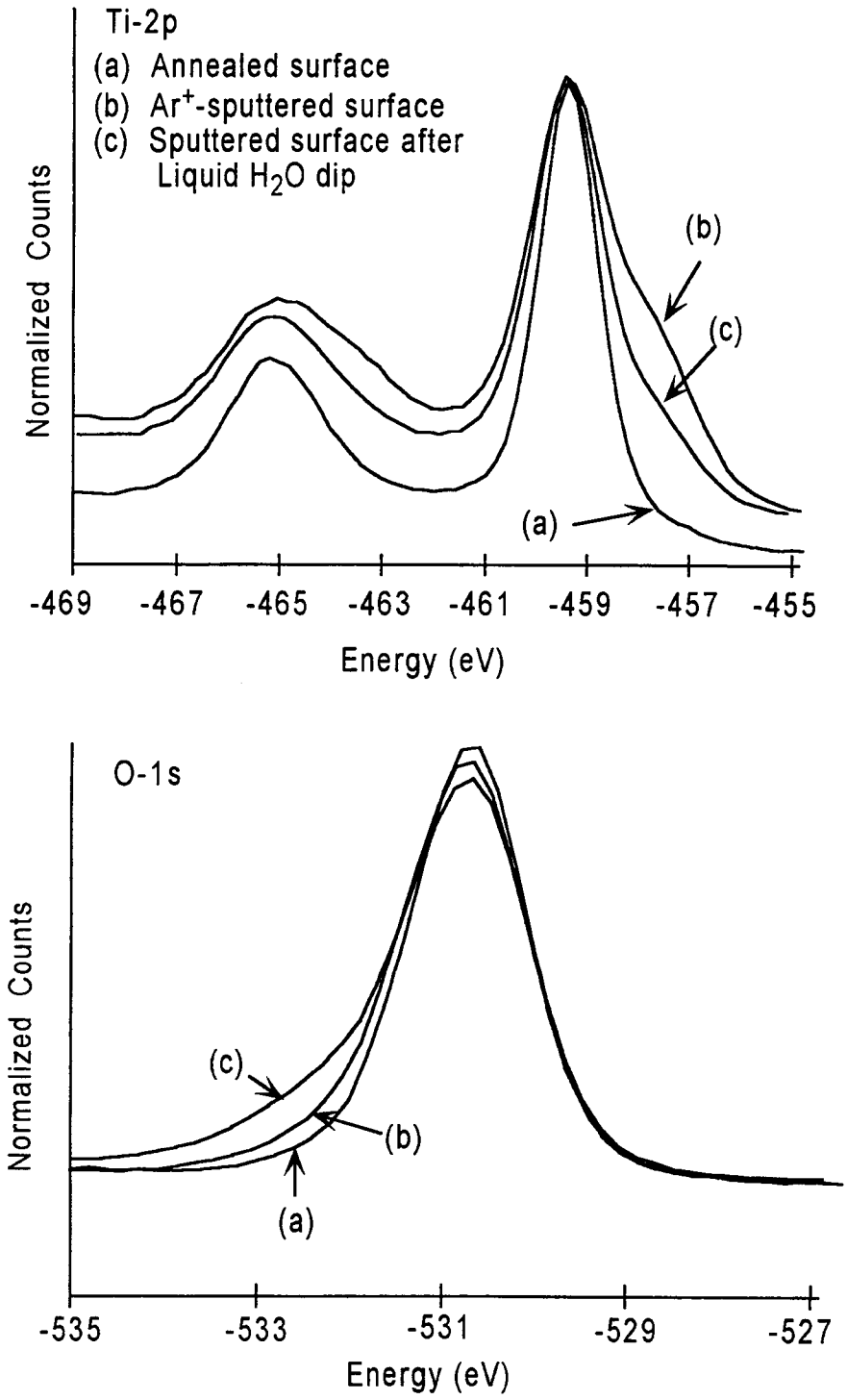

water exposure. Expanding the defect state in the gap shows conclusively that no defects remain after the water dip. Since UPS is more surface specific than XPS, this constitutes proof that all surface defects have been healed.

Figure 5.18 also shows that exposure to liquid water results in the formation of at least one additional peak in the UPS spectrum. There is clearly an additional feature at about -10 eV, as observed in the 1977 study. It could also be argued that the peaks at -6 eV and -8 eV have increased in size as well. This argument was made in the 1977 study for their spectra. But in the 1977 study, spectra were aligned by overlapping the edge of the valence band for each spectrum. This resulted in spectra with peaks growing at -6 and -8 eV, but also with the large background feature between -14 and -15 eV increasing with each water dose. There is no reason to believe that any change in the size of this background feature occurs, such that it may be more reasonable to align spectra so that the height of this feature is more uniform. When this is done, it is clear that peak growth at -6 eV and -8 eV is small, if it exists at all. Again, this speaks to the difficulty involved in analyzing UPS spectra for TiO_2. It seems that a reasonable overlap scheme can be found to make spectra conform to almost any desired interpretation of the interaction on the surface. Some groups align the large background peak, as we have done; some align the edge of the valence band, as was done in the 1977 study. Any feature chosen as the reference in a UPS spectrum could be changing in size and location during surface treatment, making the choice ambiguous. Since most early studies of H_2O on $TiO_2(110)$ were done using UPS, it is not surprising that three conflicting interpretations of the data were reached. Here we have provided independent evidence to support the claim that water heals defects, likely by dissociating so that a hydroxyl group adsorbs at the defect site. Based on this XPS observation, past and current UPS spectra can be overlapped to paint a consistent picture. This process of making UPS spectra fit an interpretation instead of being able to draw a conclusive interpretation from the UPS data is dangerous. For this reason, no more UPS studies will be presented in this thesis.

Figure 5.18: UPS spectra showing H_2O healing surface defects on sputtered (110) TiO_2

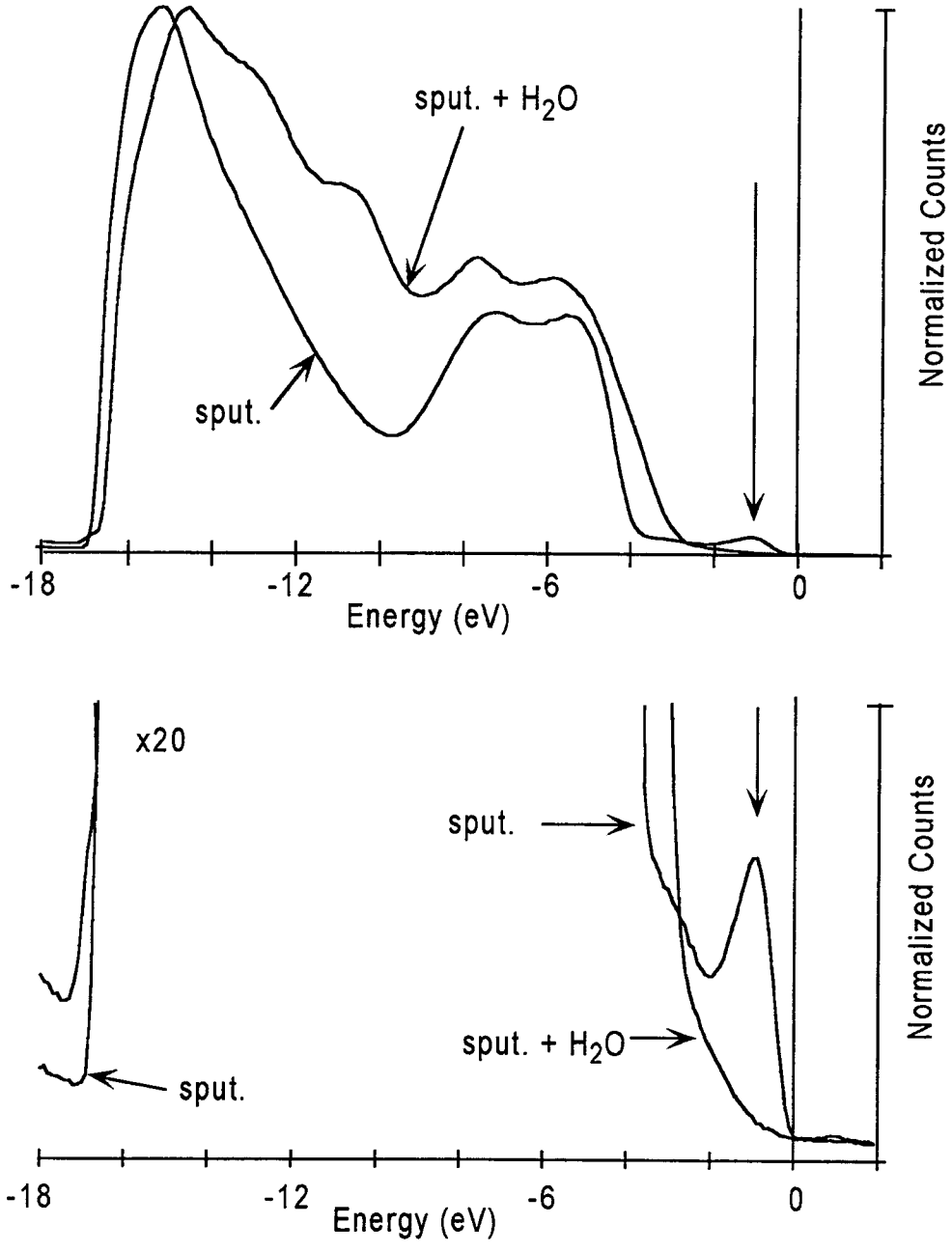

5.3.4 Section Summary

The above XPS studies show that surface defect signatures on $TiO_2(110)$ can be removed by liquid or high-pressure vapor H_2O exposures. Since signatures consistent with hydroxyl groups are also present after these water doses, this could occur through intact OH healing of a Ti^{3+} defect to form a Ti^{4+}:$(OH)^-$ complex. Unfortunately, this can not be conclusively determined from these studies because hydroxyl growth appears even on surfaces that have no defects to begin with and demonstrate no healing after exposure. These studies also raise serious questions about the usefulness of UPS as a technique to study TiO_2 surfaces. Such studies have led to conflicting interpretations of interactions between these surfaces and H_2O because there are no stable features in the UPS spectrum to use as references. The result is that spectra can be overlapped in many ways, each leading to a different physical interpretation. The temptation is to "reverse-fit" the UPS spectrum so that they are consistent with an existing picture of the reaction occurring, as could be done here. (This leads me to abandon UPS as a technique until these problems are resolved. My collaborators at PNL still use the technique to double-check XPS results, but do not rely on it to draw independent conclusions.)

5.4 Interactions between HCOOH and Defects on (110) TiO_2 Surfaces

The studies for O_2 and H_2O seem to indicate that oxygen-containing molecules dissociate and heal defects on $TiO_2(110)$ surfaces. Evidence in the literature shows similar defect healing for surfaces exposed to NO [38, 40, 41] and SO_2 [42, 43]. Based on these studies, it is tempting to conclude that all oxygen-containing molecules will behave the same way. But CO gives an example of an oxygen-containing molecule that may react with the surface to *create* additional defects [36]. In the following sections, it will be demonstrated that formic acid (HCOOH) adsorbs on the surface, yet does so without healing defects. Despite the presence of two oxygen atoms in each formic acid molecule, no dissociation to heal defects will be evident. For complex organic molecules, reactions on TiO_2 surfaces are varied: some involve defect healing through dissociation of the molecule; others scavenge oxygen from the surface to create defects; and many simply do not react with the surface. While it is

useful to characterize the response of these surfaces to a given molecule, it would be more useful to establish the parameters that dictate which behavior will occur.

Here a cell containing pure liquid HCOOH is attached to the side of the reaction chamber in place of the water cell described previously. The air above this cell is evacuated, and the reaction chamber baked, to ensure minimal contamination during formic acid doses.

5.4.1 HCOOH on Defect-Free Surfaces

Figure 5.19 shows an overlap of the Ti-2p and O-1s energy regions for spectra taken to explore the interaction between formic acid and defect-free surfaces. Here a defect-free surface was prepared by first sputtering and then annealing (heating to 600°C in $1x10^{-6}$ T O_2 and then cooling to room temperature in this oxygen environment) a reduced single-crystal wafer sample. After an XPS spectrum was taken of this surface, as shown in curve (a), the sample was transfered to the reaction chamber for exposure to vapor HCOOH. Three successive vapor doses were applied to this defect-free surface, with XPS spectra taken between each dose. These spectra are shown in curves (b)-(d). Here no change occurs in the Ti-2p spectra when formic acid is applied to the defect-free surface, indicating that HCOOH does not change the valence state of surface titanium atoms. But with increasing exposure to HCOOH, a shoulder grows 2.0 eV to higher binding energy on the O-1s peak. Since curves (c) and (d) overlap exactly in the O-1s region, it is clear that growth of this peak saturates between the first and second formic acid exposures. This shoulder on the main oxygen peak is consistent with OH or CO bonds on the surface. Along with this peak, a small peak grows in the carbon energy window. This peak is located 4.2 eV to higher binding energy from the residual adventitious carbon peak energy, and is also consistent with CO bonds on the surface [80]. These additional peaks indicate that formic acid adsorbs on the defect-free surface. Such adsorption has been seen previously [43], and was determined to occur through dissociation of the formic acid to form hydroxyls and formate.

Figure 5.19: XPS spectra showing HCOOH on defect-free (110) TiO_2

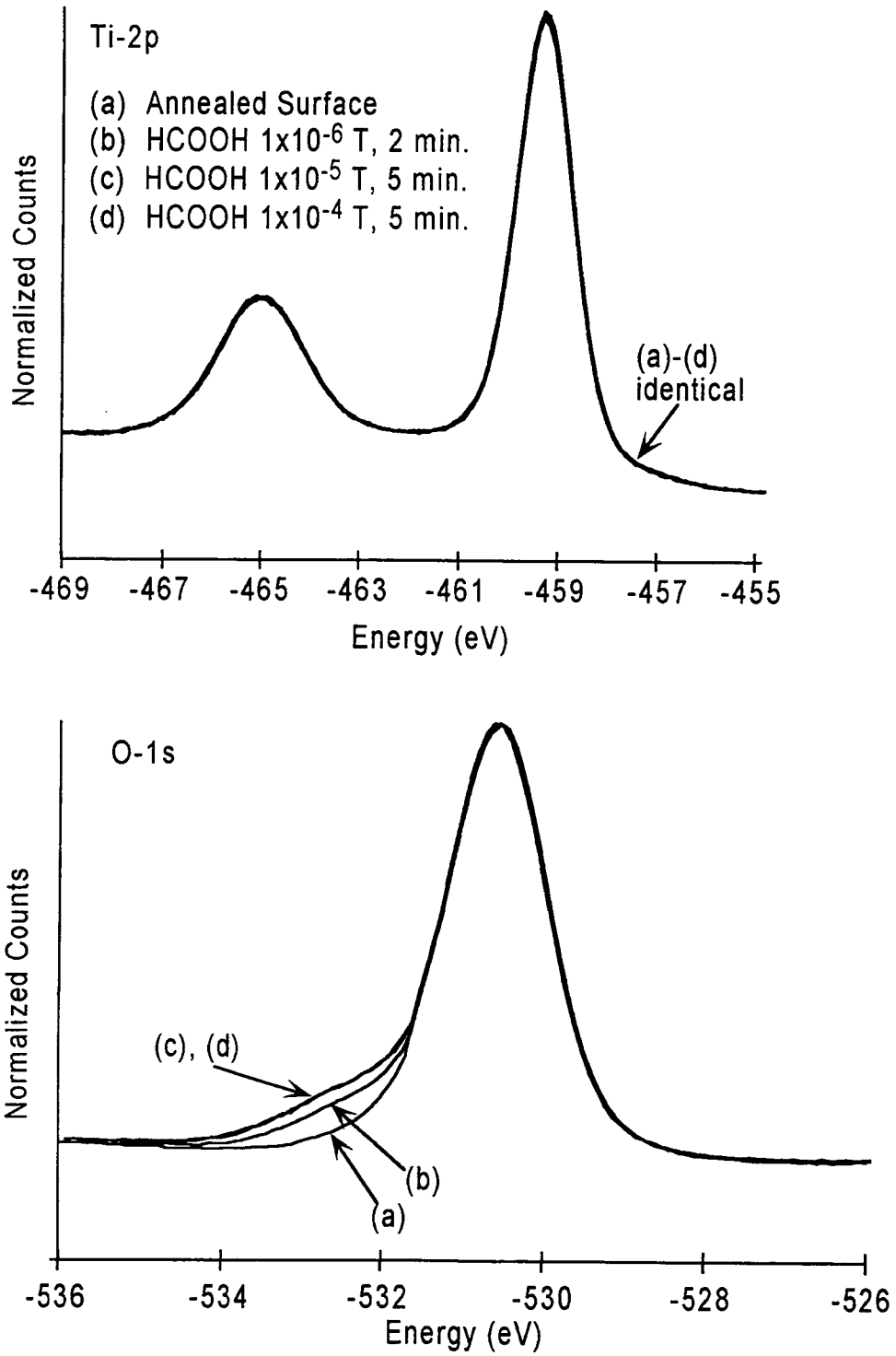

5.4.2 HCOOH on Surfaces with Defects

Figure 5.20 shows a surface that has been exposed to 1 keV Ar^+ ions for 10 minutes, and the response of this surface to successive doses of formic acid. The shoulder on the O-1s peak is again present, indicating that formic acid has adsorbed on the surface. But this shoulder is much larger than the shoulder seen on the defect-free surface, indicating that more formic acid has adsorbed than previously. This adsorption is not accompanied by any change in the shape of the Ti-2p peaks such that all defects remain unchanged despite adsorption. This could suggest that the additional adsorbed formic acid coordinates with defects, but without exchanging charge. It is also possible, however, that the increased formic acid adsorption is correlated to the increase in topographical complexity that accompanies sputter damage. Damage occurs at different rates across the surface during sputtering, increasing the effective surface area of the sample and thus making more adsorption sites available. Thus it is possible that the observed reaction between HCOOH and these surfaces is entirely independent of surface defects. In any case, this interaction does not produce defect healing, as was observed for both H_2O and O_2, requiring that a different mechanism be responsible for the adsorption behavior of HCOOH. A similar experiment was done on surfaces with defects induced by electron beam exposure, with similar results (not shown here). In this case, Ti^{3+} defects only were created, and these defects did not interact with HCOOH despite observed formate adsorption.

5.4.3 Section Summary

These experiments show that formic acid adsorbs on $TiO_2(110)$ surfaces without interacting with any oxygen vacancy defects that are present. Adsorption saturates at fairly low exposures, and any further exposure results in no change in the XPS spectra for the surface. Following these XPS experiments, the intention was to do similar experiments using SHG as a probe. But formic acid proved to be very destructive, doing extensive damage to the XPS reaction chamber and the bearings on the turbo-molecular pump. This led to the ultimate decision that placing formic acid in the SHG UHV chamber would be unwise.

Figure 5.20: XPS Spectra showing HCOOH on Ar^+ sputtered (110) TiO_2

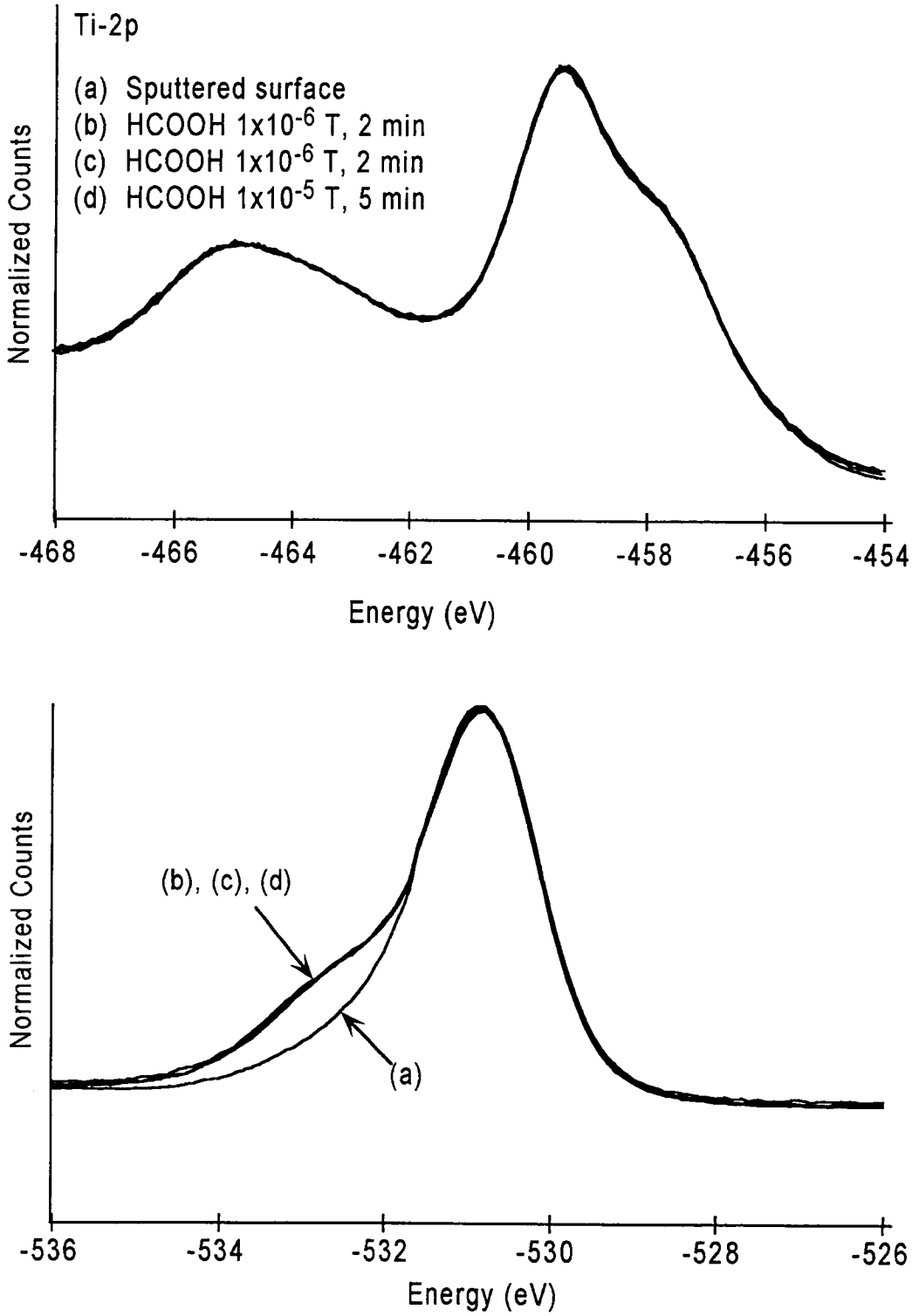

Table 5.3: Electron affinity and response to defects for oxygen-containing molecules

molecule	Response of Defect to Molecule	Electron Affinity[100]
O_2	healing: immediate	0.44 eV
H_2O	healing: at high exposures	none
SO_2[42, 43]	healing: immediate	1.11 eV
CO[36, 34, 35]	defect creation	none
HCOOH	none	none

5.5 Defect Healing Correlates to Electron Affinity: A Predictive Scheme

Based on experiments presented both here and in the literature, there are now three observed responses of the surface to oxygen-containing molecules. In the first, defects interact with the molecule so that the defect signature is removed (O_2, H_2O at high exposures, SO_2, NO). In the second, the molecule scavenges oxygen atoms from the surface to create defects (CO). In the third response, the valence state of the surface titanium atoms is not altered despite adsorption by the molecule (HCOOH). At this point it becomes desirable to establish the critical property of a molecule that determines whether that molecule will interact with a defect.

Table 5.3 summarizes the response of several molecules to Ti^{3+} defects, and also lists their electron affinity. This table suggests that defect healing by a molecule correlates to that molecule's electron affinity. Both O_2 and SO_2 heal at low exposures, and both have an electron affinity. Molecules such as CO and HCOOH that do not heal defects have no electron affinity. The only molecule listed that does not conform to this scheme is H_2O, which has no electron affinity but does heal defects at high exposures. This can be explained if defect healing only occurs when H_2O on the surface dissociates. Since hydroxyl groups have an electron affinity of 1.83 eV, it is possible that dissociation of water leads to the formation of a hydroxyl species that interacts with defects to produce the observed healing. This is likely considering that at high exposures water adsorption on the surface approaches a liquid water layer, where a balance of hydroxyls and hydrogen ions is expected.

This leads to a binary predictive scheme for interactions between defects and introduced molecules on $TiO_2(110)$: if the molecule in question has an electron affinity, it will interact with the defect, resulting in removal of the defect signature. Conversely, if the molecule has no electron affinity, such interactions will not take place. This does not preclude other types of interactions, such as the oxygen-scavenging behavior of CO [36], but only provides a criterion for interactions of one type. This simple scheme makes intuitive sense. Any molecule that can lower its energy by capturing an electron can find a source for such an electron at a Ti^{3+} defect site. The defect and the molecule in question can then form a bond through this shared electron such that the titanium atom changes to a Ti^{4+} valence state and appears healed. The result is a Ti^{4+}:X^- complex for molecule X. As an alternative, the charge-transfer to the molecule could cause it to dissociate, such that an oxygen atom from the dissociation process physically heals the defect. Such dissociation, however, is usually accompanied by a large barrier, suggesting that intact complexes might be favored. Ti-2p peaks in XPS would be insensitive to the distinction between "electronic" healing of a defect, where the valence state of the titanium is 4+ but the titanium atom may be bonded to a species other than O^{2-}, and "physical" healing of a defect, where the oxygen vacancy is filled by an oxygen atom only. For this reason, the existence of Ti^{4+}:X^- complexes has not been confirmed by conventional surface science probes, and remains a controversial theory.

Thus there are two theories suggested by these studies that must be explored further. The first is that electron affinity is the factor that dictates whether molecule-defect interactions will occur, while the second is the proposal that such interaction can occur through formation of Ti^{4+}:X^- complexes. The strategy adopted for lending credence to these theories is to select molecules for interaction based on their electron affinities, and test the success of the predictive model. It is also useful to select a molecule that will provide a signature detectible using XPS if it interacts with a defect to form a complex. Based on these criteria, N_2O is selected as a case-study for testing these theories. Nitrous oxide has an electron affinity of 1.46 eV, so it should interact with defects. In addition, if N_2O heals defects to form a complex, a measurable nitrogen peak should appear after defect healing.

Figure 5.21: SHG experiment showing N_2O on UV-damaged (110) TiO_2

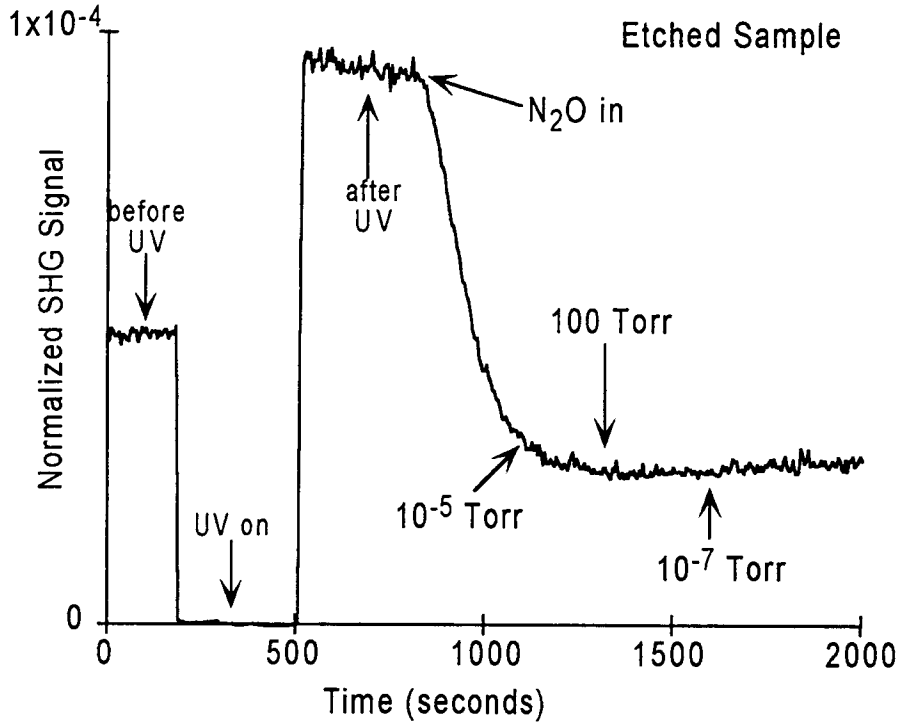

The following sections present experiments that characterize interactions between N_2O and defects using both SHG and XPS.

5.6 Interactions between N_2O and Defects on (110) TiO_2 Surfaces

To allow SHG experiments that test the response of defects to N_2O, a gas manifold was attached to the gas introduction line that would allow either N_2O or O_2 to enter the chamber. Figure 5.21 shows an experiment that contrasts the SHG response of surfaces where defects have been healed by either O_2 or N_2O. First the SHG signal for a surface where defects have been repeatedly created and then healed by O_2 is sampled. This represents a "defect-free" surface that has been shown to be electronically equivalent to the annealed samples studied using XPS. Then defects are created on this surface by exposing it to UV light until the observed change in SHG signal saturates. The resulting signal level

is that of a surface with a substantial number of Ti^{3+} defects. Now N_2O is added to the chamber, and the SHG signal is monitored while this gas interacts with the defects. Clearly defects react with the N_2O in much the same way that they interacted with O_2 in a previous experiment (see Figure 5.1). But the signal level after N_2O healing is different than the signal level seen after O_2 healing (the starting signal level). This difference would not exist if defects on both surfaces were healed by the same species, namely an oxygen ion (O^{2-}). While this observation does not constitute direct proof of the existence of Ti^{4+}:O_2^- complexes on oxygen-healed surfaces, it does provide evidence in their favor. Based on this experiment, it seems reasonable to suggest that oxygen healing occurs through formation of Ti^{4+}:O_2^- complexes, while nitrous oxide healing occurs through the formation of Ti^{4+}:$(N_2O)^-$ complexes. If this is the case, then XPS experiments should show a N-1s peak from these complexes after N_2O exposure.

For N_2O gas dosing in the XPS chamber, a cylinder of pure research grade N_2O was attached to the reaction chamber through a leak valve. This line was processed as all others were, by successively evacuating the line and then filling it and the reaction chamber with the reaction gas. As a final step, the reaction chamber and dosing line was baked, refilled with N_2O and evacuated again. Since the ion pump in the main chamber is very efficient at pumping N_2O, dosing was done in the main chamber by opening the valve between the main chamber and the reaction chamber and then bleeding gas into both chambers using the leak valve. Blank experiments with no gas show no interactions, indicating that side-chamber contamination is not a problem.

When a defect-free surface is exposed to N_2O, no change occurs in the titanium, oxygen, and nitrogen regions of the XPS spectrum. Thus the surface is entirely inert to N_2O when no defects are present. Figure 5.22 shows an overlap of a defect-free surface prepared by annealing (using the new recipe), the same surface after exposure to 1 keV electrons for 30 minutes, and the damaged surface after exposure to $1x10^{-7}$ Torr N_2O for 10 minutes. Curve (a) shows the defect-free surface, curve (b) shows the surface after Ti^{3+} have been created by the electron beam, and curve (c) shows the nitrous-dosed surface. Clearly curves (c) and (a) nearly overlap, showing that nitrous heals defects. Additional doses improve the overlap between the dosed surface and the defect-free surface, such that

after a $1x10^{-6}$ Torr 10 minute N_2O dose all defect signature is gone. An experiment where identical doses of O_2 were done shows the same amount of healing for identical doses of either O_2 or N_2O. This shows that N_2O conforms to the pattern where molecules with an electron affinity will interact with defects on $TiO_2(110)$ surfaces to remove the defect signature.

For these experiments, data in the N-1s energy region was also collected. Prior to N_2O exposures, a small amount (~0.4 atomic %) of trace nitrogen was present on the surface. After N_2O exposure, the amount of nitrogen increases slightly so that ~0.9 atomic % was present. This increase is consistent from experiment to experiment, indicating that a small amount of nitrogen is deposited on the surface during nitrous oxide dosing. But if N_2O healing of defects was occurring such that $Ti^{4+}:(N_2O)^-$ complexes were forming, the increase in nitrogen accompanying complete defect healing would be much larger than is observed. The density of defects present after electron-beam damage corresponds to vacancies for 1/6 the surface oxygen atoms. This corresponds to 1/10 ML of atoms. If each defect were healed by a N_2O molecule, then the resulting surface would have 1/5 ML coverage of nitrogen, which would yield a measured nitrogen coverage of about 6 atomic %. This leads to the conclusion that defect healing by N_2O likely occurs through dissociation, with an oxygen atom healing the defect, and N_2 desorbing. The O-1s curves support this interpretation, since the defect-free spectrum exactly overlaps the N_2O-dosed spectrum. Thus it is clear that $Ti^{4+}:(N_2O)^-$ complexes do not form.

The above spectra show that XPS detects no difference between a defect-free surface produced by annealing a sample to high temperature in an oxygen environment and one where surface Ti^{3+} defects have been healed by exposure to N_2O. In addition, defects created by electron-beam or UV exposure can be healed by O_2 to produce a surface that is indistinguishable from an annealed surface or a N_2O healed surface. This simply indicates that the surface electronic structure is the same for all these preparations. But this does not conclusively prove that these surfaces are physically identical. It remains possible that $Ti^{4+}:O_2^-$ complexes exist on the annealed surface and on the O_2-healed surface. But N_2O likely heals by dissociating so that defects are healed by a single oxygen atom, rather than a molecule. Such dissociation is observed on rutile SnO_2, where N_2O is commonly used to

Figure 5.22: XPS spectra showing N_2O on electron-beam damaged (110) TiO_2

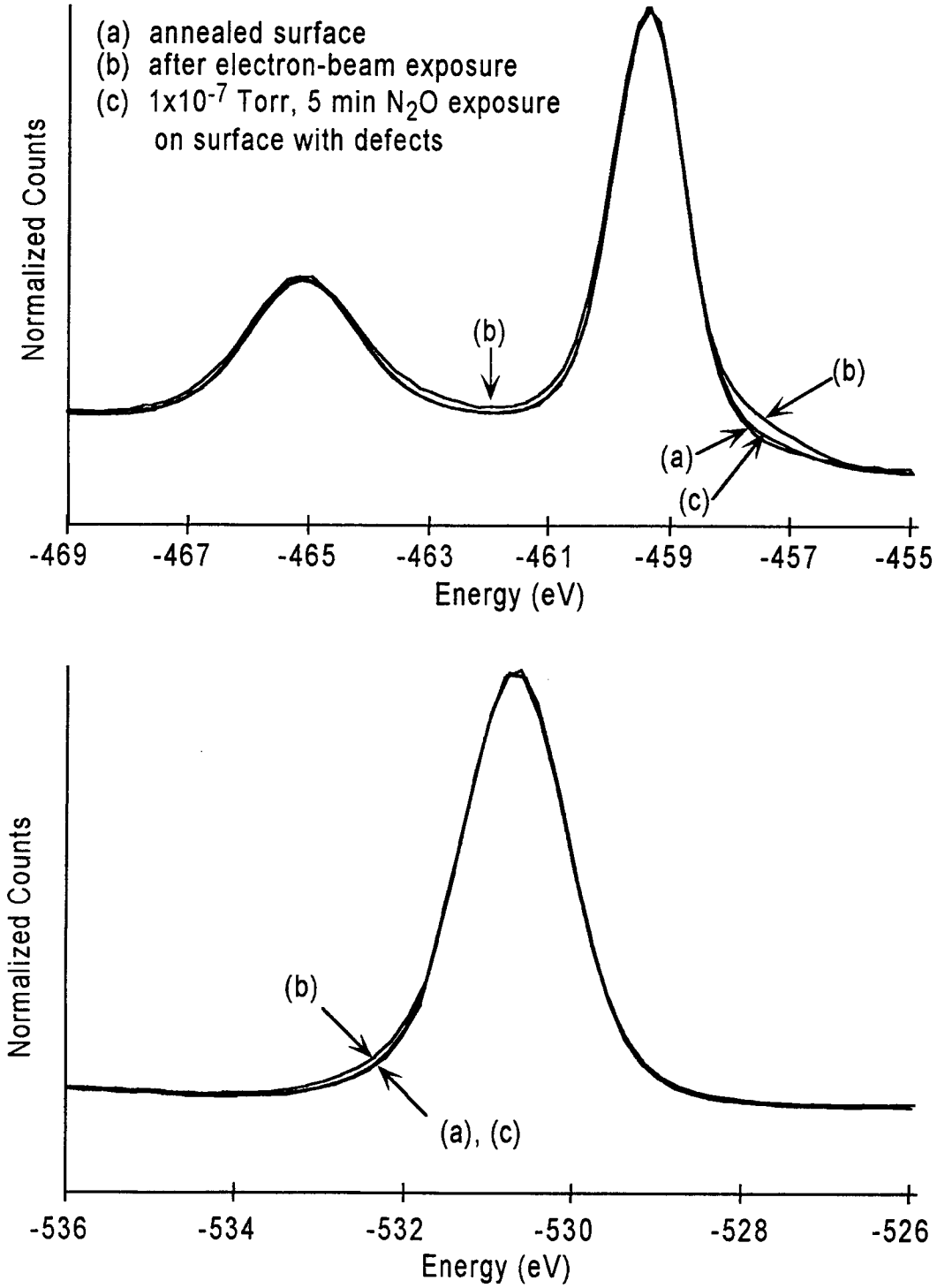

anneal samples [101]. So there may still be a physical difference between O_2-healed and N_2O-healed surface that is not detectable using XPS. Indeed such a difference is necessary to explain the difference in SHG signal for the O_2-healed and N_2O-healed surfaces.

5.7 Implications of These Results

These results call into question a fundamental assumption made by many surface scientists that study TiO_2. Namely, it is assumed that the absense of defect "signatures" (the Ti^{3+} shoulder on the Ti-2p peak in XPS and the Ti-3d state in the band-gap in UPS) is conclusive evidence that a surface is physically defect-free. Based on this assumption, samples prepared by annealing in oxygen that show no defect signature are considered to have "perfect" single-crystal surfaces. Much research is done on such surfaces, and the results of this research are interpreted based on a perfect starting surface. The SHG experiments presented here suggest that it is possible for a surface that is not physically perfect to appear to be "defect-free" using conventional probes. This may occur as molecular species complex with oxygen vacancies, as opposed to these vacancies being filled with the O^{2-} necessary to create a perfect surface. If XPS, UPS, and other commonly-used probes can not distinguish between a truly stoichiometric surface and one with molecular complexes, then interpretations of interactions observed using these probes must be made very carefully. Ideally, experiments using these techniques should be confirmed by repeating these experiments using a probe that is sensitive to changes both in electronic and physical structure. These experiments represent the first observation of a distinction between perfect *electronic* structure and perfect *physical* structure, with the first not necessarily implying the second, that appears (to my knowledge) in the literature.

Another consequence of the SHG experiments presented here is that UV light can create defects not only on O_2-healed surfaces but also on N_2O-healed surfaces. The cycles of UV defect creation followed by N_2O or O_2 defect healing can be repeated indefinitely. If these surfaces differ as proposed here, this means that UV can create defects even on the physically "perfect" surfaces that result from healing by O^{2-} when N_2O dissociates. At first it was thought that lattice and bridging oxygen atoms on the surface should be tightly

bound, such that this would be energetically unfavorable on an ideal surface. Indeed this argument led to the proposal of the more loosely bound Ti^{4+}:O_2^- complexes as responsible for the UV defect creation. Following these experiments it seems inescapable that UV light with energy just above the bulk band-gap can create oxygen vacancies on all $TiO_2(110)$ surfaces.

Finally, these experiments continue to suggest that electron affinity is the critical property that dictates whether a molecule will interact with a defect on these surfaces to result in defect healing. N_2O certainly fits this scheme, since it has an electron affinity of 1.46 eV and does heal defects. But these results are not yet conclusive, as only a small number of molecules have been studied. Most studies of interactions between these surfaces and molecules do not track the fate of defects, so molecules that adsorb but do not heal, like HCOOH, are sometimes placed in the same category as molecules that do heal defects. Additional studies, particularly those in which molecules that have an electron affinity but no oxygen atoms, are warranted to determine whether the trend observed here is real.

CHAPTER 6
CONCLUSIONS AND FUTURE WORK

The SHG experiments presented here show that $TiO_2(110)$ surfaces behaves similarly to $TiO_2(001)$ surfaces previously studied. In particular, a change in the SHG signal in UHV that is consistent with the creation of oxygen-vacancy defects is observed when these surfaces are exposed to above band-gap UV light at 266 nm. The UV-induced change saturates after a total UV exposure of 360 J/cm^2, as was observed for the (001) surface. This change can be reversed if O_2 is introduced to a partial pressure above 1x10^{-6} Torr. These observations remain consistent with the interpretation adopted in the (001) study, that molecular oxygen binds strongly to Ti^{3+} defects to form Ti^{4+}:O_2^- complexes. UV light then destroys such complexes, and the O_2 desorbes leaving behind the Ti^{3+} defects. Exposure to O_2 then simply reforms these complexes. Direct evidence of these complexes does not exist for single-crystal surfaces, but some groups have reported desorption of O_2 from TiO_2 surfaces.

Two types of surface preparations were examined using SHG. In the first, single crystal prisms were mechanically polished until optically flat. In the second, mechanically polished samples were etched in fuming H_2SO_4. Etching in this way produced a surface that appears optically to be more rough than the polished surface. But those who first reported this etching procedure claim that this apparent worsening of surface structure arises because of preferential etching of small polishing scratches present before etching. On an atomic scale, the etched surface was seen to be considerably flatter than the polished surface [25]. On the polished surface, SHG detected reversible adsorption of molecular at O_2 partial pressures in the Torr range. This adsorption was absent on the etched sample. The observed high-pressure species could be forcibly removed from the surface by a short UV exposure, and the dynamics of its re-adsorption over several seconds at high pressure could be tracked using SHG. The same experiment in air showed removal and re-adsorption of a similar species. This demonstrates the utility of SHG as a tool for observing molecular dynamics on surfaces in various environments.

To confirm the interpretation that UV creates defects on TiO_2 surfaces in UHV, similar studies were done using XPS and UPS. These techniques are sensitive to surface electronic structure, and their spectra for TiO_2 contain specific "signatures" that indicate the presence of defects. XPS experiments presented here demonstrate that exposing the etched surface to UV at 365 nm from a mercury arc lamp results in the creation of a substantial number of Ti^{3+} defects. The defect signature saturates after a UV exposure of about 270 J/cm^2, which is consistent with the observed saturation in SHG studies when possible errors in measuring the UV fluence in the XPS experiment are considered. The same experiment was repeated on an annealed sample prepared using a method that produces a surface considered by the industry to be stoichiometric and defect-free. This experiment showed that UV creates a large number of defects even on the best, most contamination-free surfaces achievable. The number of defects created can be quantified by comparing spectra to a study of electron-beam damaged surfaces, and corresponds to vacancies at half the bridging oxygen atom sites on the surface. If these defects are created by destroying Ti^{4+}:O_2^- complexes, as proposed during the SHG studies, this implies that even the best surfaces produced are covered by a large number of physical defects (where the expected atomic oxygen ion is replaced by a molecular oxygen ion) that can not be detected using techniques that measure electronic structure.

This possibility motivated the search for other molecular adsorbates that might make defects appear healed to XPS and UPS, but that do not represent physical healing of the surface. When surfaces were exposed to H_2O, defect healing did not begin to occur until extremely high vapor doses of water were applied, and was not completed until the sample was dipped in liquid water. This suggested that defect healing occurred only after water dissociated into hydroxyls. Peaks in the XPS spectra indicative of hydroxyls on the surface did appear with successive doses, but they did so even on surfaces with no defects. This prevented conclusive determination of the species responsible for defect healing during water exposure. It could be that hydroxyls are healing defects intact to form Ti^{4+}:$(OH)^-$ complexes, but this can not confirmed. When HCOOH was applied to surfaces with defects, no defect healing was observed. But carbon peaks consistent with HCOOH adsorption were observed on all surfaces exposed to formic acid. This suggests that HCOOH adsorbs on

$TiO_2(110)$ surfaces at room temperature, but that this adsorption is not related to the presence of absense of surface defects.

Results here for O_2, H_2O, and HCOOH seemed to suggest that the response of surface defects to molecules may vary to the extent that they can not be predicted. All three molecules are oxygen-containing, and thus would seem likely candidates to heal defects. But of the three, only O_2 heals readily, with H_2O healing only at high doses and HCOOH not healing at all. Molecules studied by other groups include H_2, CO, CO_2, NO, SO_2, NH_3, and H_2S. Of these studies, only those for NO, SO_2 and H_2S directly observed the fate of defects. NO and SO_2 reacted with defects, resulting in rapid removal of any defect signature present. H_2S reacted only slightly with defects, resulting in a small amount of healing, and a small amount of sulfur was detected on the surface. All evidence suggests that surfaces, whether pristine or defect-ridden, are inert to NH_3 and CO_2. In contrast, CO appears to create addition defects by scavenging bridging or lattice oxygen atoms from the surface to form CO_2. Results for H_2 are ambiguous, but seem to indicate that it does not interact strongly with defects. This wide variety of responses seems to defy classification. In fact, these interactions appear to track with the electron affinity of the introduced molecule. That is, if the reaction molecule has an electron affinity, it will interact with a defect to result in complete removal of the defect signature. A partial list of electron affinities and observed responses for some of these molecules was presented in Table 5.3. This table is reproduced in Table 6.1, and expanded to include N_2O and the other molecules discussed here (for which defects were not tracked in studies of their interactions with TiO_2 surfaces).

Included in Table 6.1 is the response of N_2O to surface defects. Experiments using SHG and XPS to characterize interactions between TiO_2 surfaces and N_2O were done to test the observed correlation between electron affinity and defect healing. N_2O, which has an electron affinity and readily heals defects, clearly fits the pattern. It was hoped that N_2O would interact with defects to form Ti^{4+}:$(N_2O)^-$ complexes that could be observed using XPS. Such an observation would be proof that such complexes were possible. Unfortunately, no nitrogen peak was seen in the XPS spectrum after defect healing by N_2O, indicating that defect healing likely happened though dissociation. The result of this healing would be a stoichiometric surface with only atomic bridging and lattice oxygen ions and no complexes

Table 6.1: Electron affinity and interaction with defects for various molecules

** Behavior of defects not directly monitored.

molecule	Response of Defect to Molecule	Electron Affinity[100]
O_2	healing: immediate	0.44 eV
SO_2[42, 43]	healing: immediate	1.11 eV
NO[38, 40, 41]	healing: immediate	0.024 eV
N_2O	healing: immediate	1.47
H_2O	healing: at high exposures	none
HCOOH	none	none
NH_3[44, 45]	none **	none
CO_2[30]	none **	none
CO[30, 34, 35]	possibly defect creation **	none

of type Ti^{4+}:X^-. But SHG results for N_2O provide further indirect evidence in support of Ti^{4+}:O_2^- complexes. Here SHG detects a difference between surfaces that were healed by N_2O and those healed by O_2. Both XPS and UPS spectra indicate that these surfaces are electronically identical. If healing by both molecules occurred through dissociation to fill the Ti^{3+} defects with atomic oxygen, SHG would indicate that there was no difference between the surfaces as well. The difference observed by SHG suggests that defects are healed by different species for the two molecules. This could be explained if the observed electronic healing occurred by dissociation for N_2O to physically heal defects, but intact by molecular oxygen to form Ti^{4+}:O_2^- complexes. Since the result of either healing would be a fully coordinated Ti^{4+} ion where the defect site was, both XPS and UPS would show no defect signature. But the physical difference between Ti^{4+}:O^{2-} and Ti^{4+}:O_2^- could be detected using SHG.

The results presented here suggest several areas of future research. First, the correlation between electron affinity and defect healing must be more strongly established by further study. In particular, the research here has demonstrated that molecules with both an electron affitinity and oxygen content will heal defects. Oxygen content alone is not sufficient to guarantee defect healing. But is an electron affinity alone sufficient to guarantee that defect healing will occur? To determine this, molecules with an electron affinity but

no oxygen content should be studied as well. Some evidence has pointed to the existence of Ti^{4+}:H^- and Ti^{4+}:S^- complexes, suggesting that species forming complexes need not contain oxygen. The CRC [100] lists countless candidates for future study. Additional studies should also be done to conclusively demonstrate the existence of Ti^{4+}:X^- complexes. For Ti^{4+}:O_2^-, vibrational studies could possibly be used to observe O_2 on the surface. Initially, EELS was explored as a technique that might be sensitive to O_2 bound to defects. Unfortunately, this state coincides in energy with a large phonon overtone in EELS spectra, making it impossible to detect its presence or absence [102]. Until a definitive experiment to resolve the debate over Ti^{4+}:O_2^- complexes can be designed, additional studies to observe similar complexes can be attempted.

Now that it has been demonstrated that above band-gap UV light can create defects on TiO_2 surfaces, many past photocatalysis experiments may need to be reconsidered. In most experiments, interactions between surfaces and molecules in the presence of UV light were thought to occur as the UV created electron-hole pairs in the near surface region. The electrons and holes could then migrate to the surface and interact with ambient molecules. This mechanism is certainly valid, and likely drives many of the observed catalytic reactions in the literature. But the new mechanism described here, where UV creates an oxygen vacancy defect which can then interact with nearby molecules, must be considered as well. Evidence in the literature [11] suggests that even the original "photocatalysis" experiment showing the electrolysis of water by UV on TiO_2 surfaces may not be driven by the electron-hole pair mechanism. Instead, it is likely that UV creates defects that interact with H_2O to result in its decomposition.

It is clear that SHG can provide additional information about surfaces that is not obtainable using conventional methods. That SHG can be used to monitor molecular adsorption and desorption in a wide variety of environments speaks to its versatility. As SHG becomes more extensively used as a surface science probe, changes in SHG signals will become better understood. This will allow differences in signal level, such as those seen for N_2O-healed and O_2-healed surfaces, to be unambiguously assigned to differences in physical surface structure. The studies presented here demonstrate the need for a technique such as SHG. For over a decade now, the absense of electronic defect "signatures" in XPS and

UPS has implied a physically perfect surface. Now that SHG has detected a substantial difference between two surfaces that appear identical using XPS or UPS, this assumption must be questioned.

BIBLIOGRAPHY

[1] A. Fujishima and K. Honda. Electrochemical photolysis of water at a semiconductor electrode. *Nature*, 238:37, 1972.

[2] Ashley N. Shultz, Winyann Jang, William M Hetherington III, Donald R. Baer, Li-Qiong Wang, and Mark H. Engelhard. Comparative second harmonic generation and X-ray photoelectron spectroscopy studies of the UV creation and O_2 healing of Ti^{3+} defects on (110) rutile TiO_2 surfaces. *Surface Science*, 339:114–124, 1995.

[3] Li-Qiong Wang, Donald R. Baer, Mark H. Engelhard, and Ashley N. Shultz. The adsorption of liquid and vapor water on TiO_2 (110) surfaces: The role of defects. *Surface Science*, 344:237–250, 1995.

[4] A. J. Bard. Design of semiconductor photoelectrochemical systems for solar energy conversion. *Journal of Physical Chemistry*, 86:172–177, 1982.

[5] A. J. Bard. Photoelectrochemistry. *Science*, 207:139–144, 1980.

[6] A. J. Bard. Photoelectrochemistry and heterogeneous photocatalysis at semiconductors. *Journal of Photochemistry*, 10:59–75, 1979.

[7] E. Pelizzetti and M. Schiavello, editors. *Photochemical Conversion and Storage of Solar Energy.* Kluwer Academic Publishers: Dordrecht, 1991.

[8] M. Schiavello, editor. *Photocatalysis and Environment.* Kluwer Academic Publishers: Dordrecht, 1988.

[9] D. F. Ollis and H. Al-Ekabi, editors. *Photocatalytic Purification and Treatment of Water and Air.* Elsevier: Amsterdam, 1993.

[10] A. Fujishima. The raising of the titanium. *Look Japan*, page 26, June 1995.

[11] A. L. Linsebigler, G. Lu, and J. T. Yates. Photocatalysis on TiO_2 surfaces: Principles, mechanisms, and selected results. *Chemical Reviews*, 95:735–758, 1995.

[12] V. E. Henrich. The surfaces of metal oxides. *Reports on Progress in Physics*, 48:1481–1541, 1985. See extensive references contained.

[13] V. E. Henrich and R. L. Kurtz. Surface electronic structure of TiO_2: Atomic geometry, ligand coordination, and the effect of adsorbed hydrogen. *Phys. Rev. B*, 23:6280–6287, 1981.

[14] E. D. Palik, editor. *Handbook of Optical Constants of Solids*, volume 23. Academic Press Inc., 1985. See TiO_2 Chapter by M. W. Ribarsky.

[15] J. G. Gay, W. A. Albers, and F. J. Arlinghaus. Irreducible representations of the little groups of D_{4h}^{14}. *J. Phys. Chem. Solids*, 29:1449–1459, 1968.

[16] M. Cordona and G. Harbeke. Optical properties and band structure of wurtzite-type crystals and rutile. *Phys. Rev.*, 137:A1467–A1476, 1965.

[17] D. C. Cronemeyer and M. A. Gilleo. The optical absorption and photoconductivity of rutile. *Phys. Rev.*, 82:975, 1951.

[18] Y. W. Chung, W. J. Lo, and G. A. Somorjai. Low energy electron diffration and electron spectroscopy studies of the clean (110) and (100) titanium dioxide (rutile) crystal surfaces. *Surf. Sci.*, 64:588, 1977.

[19] M. A. Henderson. Mechanism for the bulk-assisted reoxidation of ion sputtered TiO_2 surfaces: Diffusion of oxygen to the surface or titanium to the bulk? *Surf. Sci. Lett.*, 343:L1156–L1160, 1995.

[20] V. E. Henrich. Ultraviolet photoemission studies of molecular adsorption on oxide surfaces. *Prog. Surf. Sci.*, 9:143–164, 1979.

[21] S. Munnix and M. Schmeits. Electronic structure of oxygen vacancies in TiO_2. *Solid State Commun.*, 50:1087–1089, 1984.

[22] R. H. Tait and R. V. Kasowski. Ultraviolet photoemission and low-energy-electron diffraction studies of TiO_2 rutile (001) and (110) surfaces. *Phys. Rev. B*, 20:5178, 1979.

[23] Winyann Jang. *Second Harmonic Generation Study of Photodynamics and Adsorption/Desorption on Rutile TiO_2 Surfaces.* PhD thesis, Oregon State University, 1994.

[24] L. E. Firment. Thermal faceting of the rutile $TiO_2(001)$ surface. *Surf. Sci.*, 116:205–216, 1982.

[25] K. Sakamaki, K. Itoh, A. Fujishima, and Y. Gohshi. Surface density of states of $TiO_2(110)$ single crystal and adsorbed molecular observation by scanning tunneling microscopy and tunneling spectroscopy. *Journal of Vacuum Science and Technology A*, 8:614, 1990.

[26] Q. Zhong, J. M. Vohs, and D. A. Bonnell. Effect of reduction on the topographic and electronic structure of TiO_2 surfaces. *Surf. Sci.*, 274:35, 1992.

[27] S. Munnix and M. Schmeits. Electronic structure of ideal $TiO_2(110)$, $TiO_2(001)$, and $TiO_2(100)$ surfaces. *Phys. Rev. B*, 30:2202–2211, 1984.

[28] R. V. Kasowski and R. H. Tait. Theoretical electronic proporties of TiO_2 (rutile) (001) and (110) surfaces. *Phys. Rev. B*, 20:5168, 1979.

[29] Li-Qiong Wang, Donald R. Baer, and Mark H. Engelhard. Creation of variable concentrations of defects on TiO_2 using low-density electron beams. *Surface Science*, 320:296–306, 1994. See also contained references.

[30] W. Gőpel, J. Anderson, D. Frankel, M. Jaehnig, K. Phillips, J. Schäfer, and G. Rocker. Surface defects of $TiO_2(110)$: A combined XPS, XAES and ELS study. *Surf. Sci.*, 139:333, 1984.

[31] J. M. Pan, B. L. Maschhoff, U. Diebold, and T. E. Madey. Interaction of water, oxygen, and hydrogen with $TiO_2(110)$ surfaces having different defect densities. *J. Vac. Soc. Techno. A*, 10:2470, 1992.

[32] R. L. Kurtz, R. Stockbauer, T. E. Madey, E. Roman, and J. L. deSegovia. Synchrotron radiation studies of H_2O adsorption on $TiO_2(110)$. *Surf. Sci.*, 218:178–200, 1989.

[33] Li-Qiong Wang, Ashley N. Shultz, Donald R. Baer, and Mark H. Engelhard. Interactions of small molecules with $TiO_2(110)$ surfaces: The role of defects. J. Vac. Soc. Technol. (in press).

[34] G. Lu, A. Linsebigler, and J. T. Yates JR. The photochemical identification of two chemisorbed states for molecular oxygen on $TiO_2(110)$. *J. Chem. Phys.*, 102:3005–3008, 1995.

[35] D. D. Beck, J. M. White, and C. T. Ratcliffe. Catalytic reduction of CO with hydrogen sulfide. 3. study of adsorption of O_2 and CO coadsorbed with H_2S on anatase and rutile using Auger electron spectroscopy and temperature programmed desorption. *J. Phys. Chem*, 90:3132, 1986.

[36] W. Gőpel, G. Rocker, and R. Feierabend. Intrinsic defects of $TiO_2(110)$: Interaction with chemisorbed O_2, H_2, CO and CO_2. *Phys. Rev. B.*, 28:3427–3438, 1983.

[37] V. E. Henrich, G. Dresselhaus, and H. J. Zeiger. Chemisorbed phases of H_2O on TiO_2 and $SrTiO_3$. *Solid State Communications*, 24:623–626, 1977.

[38] G. Lu, A. Linsebigler, and J. T. Yates JR. Defect sites on $TiO_2(110)$: Production and chemical detection of active sites. *J. Phys. Chem*, 98:11733, 1994.

[39] H. Kobayashi and M. Yamaguchi. Ab initio MO study of adsorption of CO molecule on TiO_2 surfaces. *Surf. Sci.*, 214:466, 1989.

[40] F. Boccuzzi, E. Guglielminotti, and G. Spoto. Vibrational and electronic effects of NO chemisorption on TiO_2 and Ru/TiO_2. *Surf. Sci.*, 251/252:1069, 1991.

[41] N. K. Pande and A. T. Bell. A study of the interactions of NO with Rh/TiO_2 and TiO_2-promoted Rh/SiO_2. *J. Catal.*, 97:137, 1986.

[42] K. E. Smith, J. L Mackay, and V. E. Henrich. Interaction of SO_2 with nearly perfect and defect $TiO_2(110)$ surfaces. *Phys. Rev. B*, 35:5822, 1987.

[43] H. Onishi, T. Aruga, C. Egawa, and Y. Iwasawa. Adsorption of CH_3OH, HCOOH and SO_2 on $TiO_2(110)$ and stepped $TiO_2(441)$ surfaces. *Surf. Sci.*, 193:33, 1988.

[44] U. Diebold and T. E. Madey. Adsorption and electron stimulated desorption on $NH_3/TiO_2(110)$. *J. Vac. Sci. Technol. A.*, 10:2327, 1992.

[45] E. L. Roman, J. L de Segovia, R. L. Kurtz, , R. Stockbauer, and T. E. Madey. UPS synchrotron radiation studies of NH_3 adsorption on $TiO_2(110)$. *Surf. Sci.*, 273:40, 1992.

[46] K. E. Smith and V. E. Henrich. Interaction of H_2S with high defect density $TiO_2(110)$ surfaces. *Surf. Sci.*, 217:445, 1989.

[47] K. S. Kim, M. A. Barteau, and W. E. Farneth. Adsorption and decomposition of alipathic alcohols on TiO_2. *Langmuir*, 4:533, 1988.

[48] K. S. Kim and M. A. Barteau. Reactions of methanol on $TiO_2(001)$ single crytsal surfaces. *Surf. Sci.*, 233:13, 1989.

[49] A. Kiennemann, H. Idriss, R. Kieffer, P. Chaumette, and D. Durand. Study of the mechanism of higher alcohol synthesis on Cu-ZnO-Al_2O_3 catalysts by catalytic tests, probe molecules, and temperature programmed desorption studies. *Ind. Eng. Chem. Res.*, 30:1130, 1991.

[50] H. Idriss, K. S. Kim, and M. A. Barteau. Carbon-carbon bond formation via aldolization of acetaldahyde on single crystal and polycrystalline TiO_2 surfaces. *J. Catalysis*, 139:119, 1993. And contained references.

[51] S. Sato and J. M. White. Photoassisted water-gas shift reaction over platinized TiO_2 catalysts. *J. Am. Chem. Soc.*, 102:7206–7210, 1980.

[52] S. Sato and J. M. White. Photoassisted hydrogen production from titania and water. *J. Phys. Chem.*, 85:592, 1981.

[53] D. Duonghong, E. Borgarello, and M. Grătzel. Dynamics of light-induced water cleavage in colloidal systems. *J. Am. Chem. Soc.*, 103:4685, 1981.

[54] S. Fukuzawa, K. M. Sancier, and T. Kwan. Photoadsorption and photodesorption of oxygen on titanium dioxide. *J. Catalysis*, 11:364–369, 1968.

[55] M. Formenti, H. Courbon, F. Juillet, A. Lissatchenko, J. R. Martin, P. Meriaudeau, and S. J. Teichner. Photointeraction between oxygen and nonporous particles of anatase. *J. Vac. Sci. Tech.*, 9:947–952, 1972.

[56] W. J. Lo, Y. W. Chung, and G. A. Somerjai. Electron spectroscopy studies of the chemisorption of O_2, H_2 and H_2O on the $TiO_2(100)$ surfaces with varied stoichiometry: Evidence for the photogeneration of Ti^{+3} and for its importance in chemisorption. *Surf. Sci*, 71:199, 1978.

[57] Y. Yanagisawa and Y. Ota. Thermal and photostimulated desorption of chemisorbed oxygen molecules from titanium dioxide surfaces. *Surf. Sci. Lett.*, 254:L433, 1991.

[58] D. Briggs and M. P. Seah. *Practical Surface Analysis: Volume 1 - Auger and X-Ray Photoelectron Spectroscopy.* John Wiley and Sons, 2nd edition, 1990.

[59] P. A. Franken, A. E. Hill, C. W. Peters, and G. Weinrich. Generation of optical harmonics. *Physical Review Letters*, 7:118, 1961.

[60] T. H. Maiman. Stimulated optical radiation in ruby. *Nature*, 187:493, 1960.

[61] Y. R. Shen. *The Princliples of Nonlinear Optics.* John Wiley and Sons, 1984.

[62] Robert W. Boyd. *Nonlinear Optics.* Academic Press, 1992. See Section 2.6 and 2.7.

[63] N. Bloembergen and P. S. Pershan. Light waves at the boundary of nonlinear media. *Physical Review*, 128:606–622, 1962.

[64] P.N. Butcher and D. Cotter. *The Elements of Nonlinear Optics.* Cambridge University Press, 1990.

[65] N. Bloembergen. *Non-linear Optics (reprinted edition).* Addison-Wesley, 1992. See Chapter 4.

[66] Amnon Yariv. *Quantum Electrodynamics.* John Wiley and Sons, Inc., Second edition, 1975.

[67] Y. R. Shen. Optical second harmonic generation at interfaces. *Ann. Rev. Phys. Chem.*, 40:327–350, 1989.

[68] N. Bloembergen, R. K. Chang, and C. H. Lee. Second-harmonic generation of light in reflection from media with inversion symmetry. *Physical Review Lett.*, 16:986–989, 1966.

[69] C. H. Lee, R. K. Chang, and N. Bloembergen. Nonlinear electroreflectance in silicon and silver. *Physical Review Lett.*, 18:167–170, 1967.

[70] N. Bloembergen, R. K. Chang, S. Jha, and C. H. Lee. Optical second harmonic generation in reflection from materials with inversion symmetry. *Physical Review*, 174:813–822, 1968.

[71] F. Brown and M. Matsuoka. Effect of adsorbed surface layers on second-harmonic light from silver. *Physical Review*, 185:985–987, 1969.

[72] J. M. Chen, J. H. Bower, C. S. Wang, and C. H. Lee. Optical second harmonic generation from submonolayer Na-covered Ge surfaces. *Optical Communications*, 9:132–134, 1973.

[73] M. Fleischmann, P. J. Hendra, and A. J. McQuillan. Raman spectra of pyridine adsorbed at a silver electrode. *Chem. Phys. Lett.*, 26:163–166, 1974.

[74] C. K. Chen, T. F. Heinz, D. Ricard, and Y. R. Shen. Surface-enhanced second-harmonic generation and Raman scattering. *Phys. Rev. B*, 27:1965–1979, 1983.

[75] T. F. Heinz, C. K. Chen, D. Ricard, and Y. R. Shen. Spectroscopy of molecular monolayers by resonance second harmonic generation. *Phys. Rev. Lett.*, 48:478–481, 1982.

[76] R. M. Corn and D. A. Higgens. Optical second harmonic generation as a probe of surface chemistry. *Chem. Rev.*, 94:107–125, 1994.

[77] V. Mizrahi and J. E. Sipe. Phenomenological treatment of optical second harmonic generation. *J. Opt. Soc. Am. B*, 5:660–667, 1988.

[78] Chang-Juan Ju. *Theory and Application of Optical Second Harmonic Generation on Dielectric Surfaces.* PhD thesis, Oregon State University, 1994.

[79] D. S. Chemla and J. Zyss. *Nonlinear Optical Properties of Organic Molcules and Crystals: Volume 1.* Academic Press, 1987.

[80] C. D. Wagner, W. M. Riggs, L. E. Davis, J. F. Moulder, and E. Muilenberg. *Handbook of X-Ray Photoelectron Spectroscopy.* Perkin-Elmer, Eden Prairie MN, 1979.

[81] W. Koechner. *Solid-State Laser Engineering.* Springer-Verlag, 1992. See Chapter 2.

[82] F. Zernike and J. E. Midwinter. *Applied Nonlinear Optics.* John Wiley and Sons, Inc., 1973. See Chapter 3.

[83] K. W. Kirby and L. G. DeShazer. Refractive indices of 14 nonlinear crystals isomorphic to KH_2PO_4. *J. Opt. Soc. Am. B.*, 4:1072, 1987.

[84] Private Communications: Indices provided by INRAD Inc., Northvale NJ, for commercial crystals that they produce.

[85] M. Born and E. Wolf. *Principles of Optics.* Permagon Press Ltd., 1959.

[86] H. Ito, H. Naito, and H. Inaba. Generalized study on angular dependence of induced second-order nonlinear optical polarizations and phase matching in biaxial crystals. *J. Appl. Phys.*, 46:3992, 1975.

[87] M. V. Hobden. Phase-matched second-harmonic generation in biaxial crystals. *J. Appl. Phys.*, 38:4365, 1959.

[88] T. A. Driscoll, H. J. Hoffman, and R. E. Stone. Efficient second-harmonic generation in KTP crystals. *J. Opt. Soc. Am. B*, 3:683, 1986.

[89] D. J. Gettemy, W. C. Harker, G. Lindhom, and N. P. Barnes. Some optical properties of KTP, $LiIO_3$, and $LiNbO_3$. *IEEE J. Quan. Elec.*, 24:2231, 1988.

[90] D. W. Anthon and C. D. Crowder. Wavelength dependent phase matching in KTP. *Appl. Opt.*, 27:2650, 1988.

[91] T. Y. Fan, C. E. Huang, B. Q. Hu, R. C. Eckardt, Y. X. Fan, R. L. Byer, and R. S. Leigelson. Second harmonic generation and accurate index of refraction measurements in flux-grown $KTiOPO_4$. *Appl. Opt.*, 26:2390, 1987.

[92] G. D. Boyd and D. A. Kleinman. Parametric interaction of focused gaussian light beams. *J. Appl. Phys.*, 39:3597, 1968.

[93] W. A. Marquardt and R. M. Bednarski. *U.S. Patent No. 3,888,973*, 1986.

[94] F. W. Giacobbe and G. S. Khan. Production of ultra-high purity nitrogen. *Solid State Technology*, page 77, July 1987.

[95] C. L. Thomas. *Catalytic Processes and Proven Catalysis.* Academic Press, 1970. See Page 118.

[96] ed. H. O Finklea. *Semiconductor Electrodes.* Elsevier, Amsterdam, 1988. See chapters on TiO_2, InP, and GaAs.

[97] S. E. Gilbert and J. H. Kennedy. Etching effects on photoelectrochemistry and surface structure. *J. Electrochem. Soc.*, 135:2385, 1988.

[98] Jeffrey I. Steinfeld. *Molecules and Radiation.* MIT Press, Second edition, 1985.

[99] V. E. Henrich and P. A. Cox, editors. *The Surface Science of Metal Oxides.* Cambridge University Press, 1994.

[100] R. C. Weast, editor. *CRC Handbook of Chemistry and Physics.* CRC Press Inc., 70 edition, 1990. See Electron Affinity tables.

[101] V. A. Gercher, D. F. Cox, and J. M. Themlin. Oxygen-vacancy-controlled chemistry on a metal oxide surface: methanol dissociation and oxidation on $SnO_2(110)$. *Surf. Sci.*, 306:279, 1994.

[102] Private Communications with M. A. Henderson.